Dissertations

Spring 5-2017

Advancing Structure-Property Relationships in Functional Materials Via Thiol-ene Photopolymerization

Brian Richard Donovan
University of Southern Mississippi

ADVANCING STRUCTURE-PROPERTY RELATIONSHIPS IN FUNCTIONAL

MATERIALS VIA THIOL-ENE PHOTOPOLYMERIZATION

by

Brian Richard Donovan

A Dissertation
Submitted to the Graduate School
and the School of Polymers and High Performance Materials
at The University of Southern Mississippi
in Partial Fulfillment of the Requirements
for the Degree of Doctor of Philosophy

Approved:

_____
Dr. Derek L. Patton, Committee Chair
Associate Professor, Polymers and High Performance Materials

_____
Dr. Robson F. Storey, Committee Member
Professor, Polymers and High Performance Materials

_____
Dr. Sarah E. Morgan, Committee Member
Professor, Polymers and High Performance Materials

_____
Dr. Charles L. McCormick, Committee Member
Professor, Polymers and High Performance Materials

_____
Dr. Jason D. Azoulay, Committee Member
Assistant Professor, Polymers and High Performance Materials

_____
Dr. Karen S. Coats
Dean of the Graduate School

May 2017

Published by the Graduate School

THE UNIVERSITY OF
**SOUTHERN
MISSISSIPPI**®

ABSTRACT

ADVANCING STRUCTURE-PROPERTY RELATIONSHIPS IN FUNCTIONAL

MATERIALS VIA THIOL-ENE PHOTOPOLYMERIZATION

by Brian Richard Donovan

May 2017

Thiol-ene photopolymerizations provide a robust and versatile synthetic pathway
to functional materials, and owing to the radical step-growth nature of polymerization
and the resulting homogenous network structure, provide non-convoluted insight into
how network chemistry influences and dictates macromolecular properties.

The first facet of this dissertation focuses on the design and synthesis of bio-
inspired, thin film adhesives for dry and aqueous adhesion. Drawing inspiration from the
intertidal marine mussel, Chapter II details the synthesis of adhesive networks containing
a monofunctional catechol-based monomer. The inclusion of a catechol group resulted in
significant improvements in adhesion on a variety of substrates. In Chapter III, the
inclusion of simple hydrophobic groups in the adhesive thiol-ene networks to improve
underwater adhesion is reported. The presence of hydrophobic groups effectively push
water away from the adhesive resin/substrate interface, facilitating adhesive interaction
underwater. Further, the influence of the catechol (a known radical scavenger) and the
hydrophobic groups (commonly considered non-adhesive) on polymerization kinetics,
thermal mechanical, and mechanical properties was determined.

The second facet of this dissertation focuses on the synthesis of semi-fluorinated
polymer networks, as outlined in Chapter IV. Fluorine groups impart several
advantageous properties to polymeric materials including increased mechanical strength,

chemical and thermal stability, and unique optical and wetting properties. As such, the inclusion of the trifluorovinyl ether group in a thiol-ene photopolymerization resulted in the rapid and efficient synthesis of semi-fluorinated networks, exhibiting significant increases in thermomechanical and mechanical properties as a function of fluorine content.

ACKNOWLEDGMENTS

I would like to gratefully acknowledge several individuals without whom this dissertation would not have been possible:

My advisor, Dr. Derek L. Patton, for training me when I joined the lab as a novice and for providing me with the guidance necessary to develop into a better researcher and mentor. Thank you for providing me with the opportunity to explore my own ideas, travel, and present within the polymer community, and for your steadfast resolve and patience in the face of questions and concerns you had no doubt heard many times before.

My committee members Dr. Robson F. Storey, Dr. Sarah E. Morgan, Dr. Charles L. McCormick, and Dr. Jason D. Azoulay for their support and willingness to help me in the pursuit of my education and career. From letters of recommendation to research advice, I sincerely appreciate the time and effort you have spent helping me reach this point. Thank you.

The Patton Research Group, past and present: Dr. Emily Hoff, Li Xiong, Wei Guo, Dahlia Amato, Doug Amato, Yidan Guan, Cassandra Reese, Dr. Austin Baranek, Dr. Jananee Narayanan, Dr. Bradley Sparks, Dr. Ryan Hensarling, Matt Jungman, and Arthur Leblanc. Thank you for making the lab days lighter, for listening to me rant and rave, and for providing me with guidance and feedback on my research efforts.

Dr. William Jarrett for his expertise in NMR and his patience training me in various techniques. I can assure you that collecting all those spectra was worth it.

The various undergraduate researchers I've been fortunate to work with over the years: Jared Cobb, Laken Kendrick, Ethan Hoff, Brandon Yrle, Jason Ballenas, and

Teddy Wong. Thank you all for helping me with the complex and the mundane, and for staying patient with me as I learned with you.

To Katrina Knauer for the constant support and companionship throughout the dissertation process and over my graduate career. Thank you for being there night or day, and for helping me relax and keep my days in perspective.

Various colleagues and staff at SPHPM and elsewhere for their friendship, advice, and support including Allison Couche, Jeff Velarde, Mike Brignone, Mike Sennett, Brian Greenhoe, Kyle Bentz, Brooks Abel, Bin Yang, Corey Parada, Hunter Cooke, Andrew Janisse, Phil Pickett, and Jody Wiggins.

DEDICATION

To my mother and father, Mary and Richard Donovan, for the unending support and belief. Your encouragement and love has always given me the strength to move forward and pursue my ambitions.

TABLE OF CONTENTS

LIST OF TABLES

LIST OF ILLUSTRATIONS

LIST OF ABBREVIATIONS

APE	pentaerythritol
AFM	atomic force microscopy
BnSH	benzyl mercaptan
BPA	Bisphenol A
DAm	dopamine acrylamide
DMA	dynamic mechanical analysis
Eug	Eugenol
EugOH	4-allylpyrocatechol
EugTES	triethylsilane eugenol
F6	2-(perfluorohexyl)ethyl acrylate
HCl	hydrochloric acid
H$_2$O	water
IBA	isobutanol
IPA	isopropanol
M3MP	methyl 3-mercaptopropionate
MeEug	methyl eugenol
Mod-PETMP	modified PETMP
n	refractive index
PEG	poly(ethylene gycol)
PETMP	pentaerythritol tetrakis(3-mercaptopropionate)
Ph-TFVE	phenyl trifluorovinyl ether
PrSH	1-propanethiol

RT-FTIR	real time-Fourier transfer infrared
TES	triethylsilane
TFVE	trifluorovinyl ether
T_g	glass transition temperature
TGA	thermogravimetric analysis
TiO_2	titanium dioxide
TIP	titanium isopropoxide
TMPMP	trimethylolpropane tris(3-mercaptopropionate)
TPFPB	tris(pentafluorophenyl)borane
UV	ultraviolet
UV-Vis	ultraviolet-visible

CHAPTER I – INTRODUCTION

1.1 Thiol-Ene Network Polymerization

The radical mediated thiol-ene reaction was first proposed in the 1930s[1] and has since emerged as a valuable tool for the synthetic polymer chemist. Thiol-ene reactions proceed according to Figure 1.1 and display many of the characteristics of a "click" reaction, including high yields, short reaction times, minimal by-product generation, solvent-free or solvent-tolerant reaction conditions, and an insensitivity to moisture and oxygen.[2-7] In the presence of a radical initiator (thermal, photo, or redox), the thiol hydrogen is readily abstracted to form a thiyl radical (initiation). The thiyl radical then adds across a carbon-carbon double bond, generating a β-thioether carbon-centered radical (propagation). The carbon-centered radical next undergoes a rapid chain transfer reaction with an additional thiol to regenerate the thiyl radical species and the thiol-ene product (chain transfer). The step nature of the thiol-ene reaction, the rapid initiation and
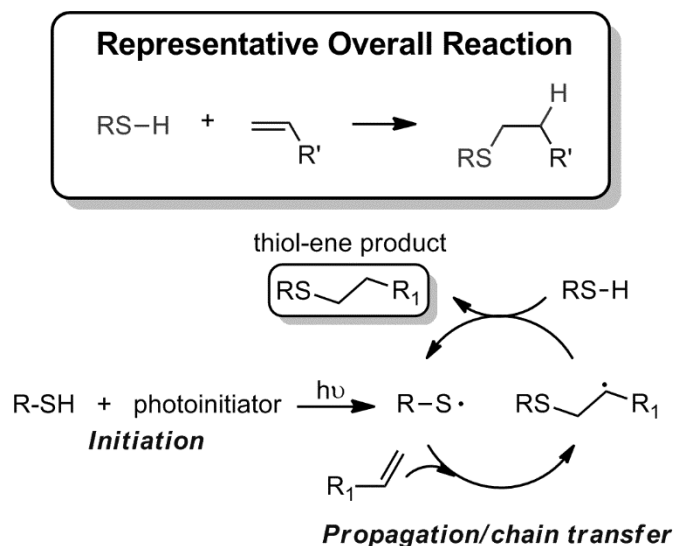
Figure 1.1 Thiol-ene radical reaction.

1
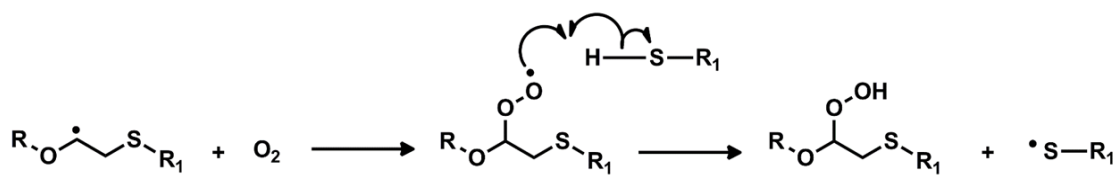
Figure 1.2 Reaction of oxygen with the propagating carbon-centered radical formed in the thiol-ene radical reaction. The formed peroxy radical is capable of abstracting a hydrogen from a thiol, allowing the thiol-ene mechanism to continue.

chain transfer reactions, and the oxygen insensitivity are facilitated by the abstractable hydrogen of the thiol functional group. This abstractability is imparted by the low bond dissociation energy (BDE) of the S-H bond, generally accepted to be approximately 87 kcal mol^{-1}.[8-11] In the presence of a radical, R$^{\bullet}$, with a corresponding higher R-H BDE, such as those generated by a photoinitiator or the carbon-centered radical following the thiol-ene propagation step, the thiol will readily transfer its hydrogen and generate a thiyl radical (the BDE of a secondary alkyl C-H bond is ~ 95-99 kcal mol^{-1}).[10-13] Additionally, in the event that an oxygen molecule reacts with the propagating radical (Figure 1.2), the formed peroxy radical is capable of abstracting a thiol hydrogen, regenerating the thiyl radical, and the thiol-ene mechanism continues.

The thiyl radical is electrophilic in nature[14], and thus tends to react more rapidly with electron-rich double bonds (vinyl ether) than electron-poor double bonds (acrylate), following the general order of reactivity presented in Figure 1.3a.[2, 15, 16] Differences in thiol reactivity (Figure 1.3b) are less reported, though it has been demonstrated that propionate and glycolate esters react faster than alkyl thiols (Figure 1.2b).[16, 17] When the functionality, *f*, of the thiol and alkene monomers is such that *f* > 2, poly(thioether) networks may be formed, and such networks are the primary focus of this dissertation.

(a) norbornene > vinyl ether > allyl ether ~ allyl trizaine > alkene > acrylate > styrene

(b) gylcolate > propionate > alkyl
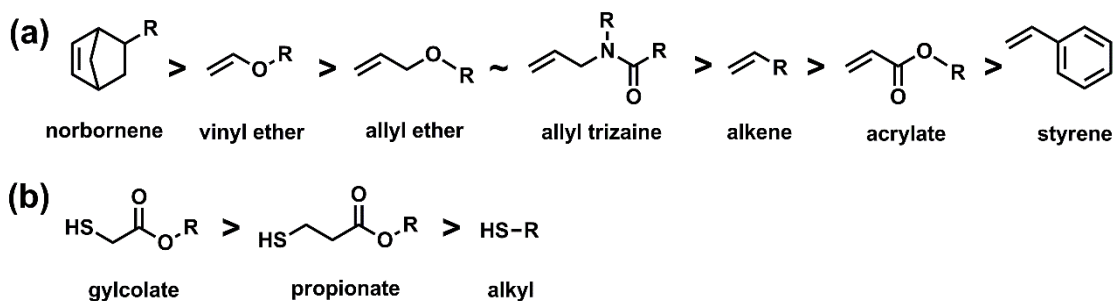
Figure 1.3 Structure and reactivity of some common (a) alkene and (b) thiol monomers used in the thiol-ene radical reaction.

Our interest in the thiol-ene network polymerization, specifically, the thiol-ene photopolymerization is two-fold. First, due to the efficiency and robustness of "click" type reactions, combined with the spatial and temporal control of light-induced polymerizations, thiol-ene photopolymerizations are an ideal synthetic pathway for the generation of monolithic, polymeric materials. Second, owing to the step-growth nature of polymerization, molecular weight builds in a uniform manner, reaching the gel-point only at relatively high functional group conversions, therefore yielding uniform polymer networks.[18, 19] Thus, thiol-ene photopolymerizations offer not only an ideal synthetic method for the generation of functional materials, but also provide a means to directly study the influence of incorporated chemistries on macromolecular properties. This strategy has been successfully utilized by our group and others to generate functional thiol-ene materials and investigate their structure property relationships in areas including superhydrophobic/superolephobic surfaces[20, 21], optical materials[22, 23], nano- and microparticle synthesis[24, 25], anti-bacterial coatings[26, 27], porous scaffolds[28, 29], shape changing materials[30, 31], and semi-fluorinated polymer networks.[17, 32] This list is not all-inclusive, but does demonstrate the depth and diversity with which thiol-ene chemistry may be utilized.

This dissertation utilizes thiol-ene photopolymerizations in two main areas of focus. The first is in the synthesis and understanding of bio-inspired adhesives, specifically those derived from the unique binding ability of the marine mussel. As discussed in the following pages, the marine mussel has a unique ability to bind in harsh, aqueous environments. By mimicking the adhesive chemistry employed by the mussel, we aim to impart adhesive functionality to a rapidly photopolymerized thiol-ene network in both dry and wet environments. A fundamental understanding of how the catechol influences polymerization kinetics and the resulting network structure may lend itself to the development of "on-demand" adhesives and sealants for use in applications where water is ubiquitous and other polymerization mechanisms may be inhibited. The second area of focus is in the generation of semi-fluorinated materials. Fluoropolymers and their semi-fluorinated analogues are well known to have unique chemical, mechanical, and physical properties. By use of a fluorinated alkene, we seek to directly incorporate a semi-fluorinated linkage into the backbone of a thermoset thiol-ene network, ideally improving thermomechanical and mechanical properties, as well as both thermal and chemical network stability.

1.2 Bio-Inspired Adhesion

1.2.1 Polymeric Adhesion

Adhesives are generally defined as a material which brings two substrates together at an interface and resists separation.[33] Albeit varied in their design and application, adhesives have been widely implemented due to their unique advantages over conventional binding methods, including 1) the ability to join dissimilar materials, 2) the ability to join thin sheet material efficiently, i.e. composites, 3) improved stress

4

distribution in a material's joint, 4) a greatly improved design flexibility, and 5) the cost

effectiveness and convenience of the technique.[33] Generally, to develop a strong

adhesive one must consider the balance between a materials cohesion, or the forces that

cause a material to stick to itself, and adhesion, or the chemical or physical forces that

cause dissimilar surfaces to stick together.[34] Cohesive interactions in polymer adhesives

include noncovalent interactions, such as hydrogen bonding, but also benefit from the

stronger covalent bonds formed during polymerization. Further, the macromolecular

properties of the polymer, including the crosslink density, the modulus of the resulting

polymer, and the molecular weight between crosslinks, also greatly impact the adhesive's

cohesive strength.[35] Adhesive interactions are generally categorized as mechanical or

chemical.[36] Mechanical adhesion is based on the adhesive interlocking into irregularities

on the surface of a substrate. This requires that the adhesive can diffuse into either open

pores or defects on a surface (organic and inorganic substrates), or polymer chains from

the adhesive can diffuse into the polymer chains of the substrate and form entanglements

(organic substrates only), and has been shown to depend on substrate roughness.[33, 37]

Chemical adhesion proposes that materials in close proximity will adhere to each other

via intermolecular forces (dipole interactions, hydrogen bonding) and chemisorption

(covalent bonding, metallic bonding) of functional groups within the polymer to a

substrate, either organic or inorganic.[38] In general, polar groups present in adhesives and

the chemical interactions they partake in, are the primary, and most widely accepted

factor contributing to interfacial adhesion.

      Overall, adhesion is a complex phenomenon, dependent on a range of forces and

interactions. This complexity, however, leads to a myriad of potential design

considerations when attempting to develop a successful and applied adhesive. As our

research group focuses on synthetic polymer chemistry, we target chemical modification

of polymeric materials to impart adhesion. Specifically, we draw inspiration from nature,

focusing on the design and synthesis of biomimetic adhesives.

1.2.2 Mussel-Inspired Adhesion

Nature provides several examples of extraordinary adhesive systems, though the

most widely investigated are that of the gecko and the marine mussel. The gecko utilizes

an array of angled, hair-like fibers on the bottom of its feet to generate reversible and

rapid adhesion, and is dependent on a number of factors including the nanostructure and

surface area of the fibers, and the angle at which they attach.[39-41] As such, many

synthetic mimics focus on re-engineering the gecko foot nanostructure.[42-44] The marine

mussel, though equally complex, achieves a significant portion of its adhesive strength

from a unique chemistry, specifically, the rare amino acid 3,4-dihydroxyphenylalanine
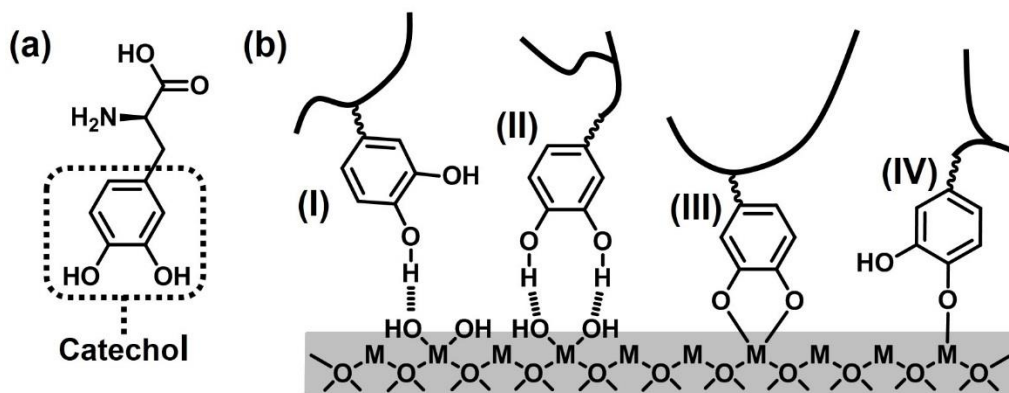
Figure 1.4 (a) 3,4-dihydroxyphenylalanine (DOPA) (b) catechol binding modes to a
general metal oxide (MO_x) substrate (I) mono hydrogen bonding (II) dual
hydrogen bonding (III) bidentate chelation (IV) monodentate chelation.

(DOPA, Figure 1.4a).[45] Consequently, synthetic mimics of the marine mussel adhesive

are often based on the inclusion of DOPA analogues.[46-48] DOPA, and in particular its

6

catechol moiety, are capable of several adhesive interactions including both mono and dual hydrogen bonding[49, 50], π-π interactions, and mono and bidentate chelation to inorganic surfaces (Figure 1.4b).[50-53] The reported binding modes are pH dependent, as the catechol may oxidize to the non-adhesive quinone form under basic conditions.[49, 51] It should be noted that the oxidation of DOPA in basic pH buffers has been utilized to develop polydopamine coatings that demonstrate adhesion to a wide variety of substrates.[54-56] This mechanism is utilized by the mussel to impart cohesive strength to its naturally-occuring adhesive, however, our interest lies in the incorporation of catechol monomers into oil-based, and well-defined polymer thermosets where DOPA oxidation does not lead to network formation, but rather results in a decrease in adhesive strength[45, 51], and thus oxidation shall be avoided.

As described, the presence of DOPA in the marine mussel's adhesive proteins plays a critical role in the organism's adhesion. Of particular interest is the mussel's unique ability to bind underwater, to a range of substrates, in the turbulent environments of an intertidal zone. Water is typically detrimental to adhesion due to its ability to permeate adhesive materials, diminishing cohesive strength[57], and to disrupt the interactions associated with the chemical binding mechanism of adhesion (i.e. hydrogen bonding).[58] Undoubtedly, the ability of the mussel adhesive to bind underwater extends beyond the presence of a single amino acid, but DOPA, the primary chemistry associated with adhesive interaction, has been demonstrated to bind in the presence of water.[50-53, 59] Though experimentation has demonstrated the ability of DOPA to adaptively bind underwater, a fundamental description of this interaction has been difficult to capture. A recent modeling study, however, demonstrated that for a catechol approaching a hydrated

silica surface, the most energetically favorable condition was measured when the catechol was bound directly to the silica surface, displacing pre-absorbed water molecules.[60] Additionally, it has been demonstrated that synergistic mechanisms of action facilitate catechol binding to a surface by the inclusion of ionic or hydrophobic groups, capable of displacing water or other surface contaminants prior to adhesive binding.[61, 62]

In summary, the unique binding capabilities of the marine mussel in both dry and aqueous environments provide inspiration for the development of biomimetic synthetic adhesives. In Chapters II and III, we aim to develop a fundamental understanding of how a catechol monomer influences polymeric network properties in order to generate adhesives demonstrating an "on-demand" cure, and improved binding strength under a variety of applied conditions.

1.3 Semi-Fluorinated Polymers

The second facet of this dissertation focuses on the generation of photopolymerized semi-fluorinated networks. Fluoropolymers are desirable materials due to their high mechanical strength, thermal and chemical stability, unique wetting behavior, and desirable optical properties.[63-67] These properties are imparted by the high electronegativity and low polarizability of the fluorine atom, and by the high strength of the C-F and C-C bond in fluorinated materials (~485 kJ mol^{-1} and ~360 kJ mol^{-1}, respectively).[68, 69] Generally speaking, polymers with high fluorine content exhibit the most desirable of the previously listed properties, however, highly fluorinated materials are often crystalline and therefore difficult to synthesize and process.[70] To alleviate demanding processing conditions, amorphous, semi-fluorinated polymers have been

synthesized that display analogous properties to their fully fluorinated counterparts but exhibit improved processability.[65, 71, 72]

Of particular interest to this dissertation are semi-fluorinated polymers employing the synthetic benefits of photopolymerization. Successful photopolymerizations have been carried out utilizing vinylidene fluoride[73], fluoroepoxides[74], and fluorinated thiol-ene monomers[32], however, the most widely utilized fluoromonomers have been mono and multifunctional fluorinated acrylates.[68] One of the more common examples is the polymerization of diacrylate and dimethacrylate functionalized perfluoropolyethers (PFPEs), leading to the formation of crosslinked semi-fluorinated polymers[75-78]. Owing to the unique properties imparted by the fluorine content within these materials, acrylic/methacrylic semi-fluorinated polymers have found use in various materials applications. However, acrylate and methacrylate photopolymerizations are a radical chain growth process and so suffer from oxygen inhibition and the formation of heterogeneous networks characterized by increased shrinkage and shrinkage stress. Consequently, we considered the use of fluorinated alkenes to develop semi-fluorinated materials through the thiol-ene reaction.

As mentioned, semi-fluorinated thiol-ene materials have been synthesized, though they are scarcely reported in the literature. Additionally, all reported networks rely on the use of perfluoroalkyl chains and thus do not benefit from the incorporation of fluorine in the backbone of the polymer network.[20, 32, 79] Literature precedent exists for the small molecule addition of a thiyl radical to certain fluorinated alkenes[80, 81], though such reactions have never been explored in the context of the thiol-ene network polymerization. As such, Chapter IV details the direct incorporation of fluorine atoms

into the backbone of a polymer network via a thiol-ene photopolymerization utilizing a fluorinated alkene to generate well-defined, semi-fluorinated materials.

1.4 Summary

In summary, this dissertation aims to impart the unique properties of catechol-based adhesive monomers and semi-fluorinated crosslinks to photopolymerized thiol-ene networks. The use of thiol-ene photopolymerizations provides not only a robust, versatile, and rapid synthetic pathway to the generation of functional materials, but also, owing to the well-defined network structure, provides a clear insight into how an incorporated chemistry (i.e. a catechol or semi-fluorinated linkage) influences macromolecular properties. Inspired by the intertidal marine mussel, Chapter II investigates the synthesis and incorporation of an oil-soluble catechol-monomer into a photopolymerized thiol-ene network. The adhesive ability of the catechol combined with the rapid and robust nature of the thiol-ene polymerization may lead to the generation of well-defined and "on-demand" curing adhesives capable of improved binding to a variety of substrates. Further, in Chapter III, we seek to extend the binding capabilities of the catechol-based thiol-ene adhesives to aqueous environments by the synergistic incorporation of hydrophobic groups meant to assist in the removal of water from a substrate interface. Finally, in Chapter IV, by use of a fluorinated alkene, the synthesis of semi-fluorinated thiol-ene networks containing high concentrations of fluorine in the backbone of the polymer network is reported. Though varied in their chemistry, all chapters of this dissertation focus on the synthesis of functional thiol-ene materials, and the development of the fundamental structure-property relationships governing their macromolecular performance.

10

1.5 References

(1). Kharasch, M. S.; Mayo, F. R. *Chem. Ind.* **1938,** *57*, 752-754.

(2). Hoyle, C. E.; Bowman, C. N. Thiol–Ene Click Chemistry *Angew. Chem. Int. Ed.* **2010,** *49*, 1540-1573.

(3). Lowe, A. B. Thiol-Ene "Click" Reactions and Recent Applications in Polymer and Materials Synthesis *Polym. Chem.* **2010,** *1*, 17-36.

(4). Kade, M. J.; Burke, D. J.; Hawker, C. J. The Power of Thiol-Ene Chemistry *J. Polym. Sci. A: Polym. Chem.* **2010,** *48*, 743-750.

(5). Lowe, A. B.; Hoyle, C. E.; Bowman, C. N. Thiol-Yne Click Chemistry: A Powerful and Versatile Methodology for Materials Synthesis *J. Mater. Chem.* **2010,** *20*, 4745-4750.

(6). Hoogenboom, R. Thiol-Yne Chemistry: A Powerful Tool for Creating Highly Functional Materials *Angew. Chem. Int. Ed.* **2010,** *49*, 3415-3417.

(7). Kolb, H. C.; Finn, M. G.; Sharpless, K. B. Click Chemistry: Diverse Chemical Function from a Few Good Reactions *Angew. Chem. Int. Ed.* **2001,** *40*, 2004-2021.

(8). Armstrong, D. A. Thermochemistry of Sulfur Radicals. In *S-Centered Radicals*, Alfassi, Z. B., Ed. John Wiley & Sons: Chichester, England, 1999.

(9). Denisov, E.; Chatgilialoglu, C.; Shestakov, A.; Denisova, T. Rate Constants and Transition-State Geometry of Reactions of Alkyl, Alkoxyl, and Peroxyl Radicals with Thiols *International Journal of Chemical Kinetics* **2009,** *41*, 284-293.

(10). Dénès, F.; Pichowicz, M.; Povie, G.; Renaud, P. Thiyl Radicals in Organic Synthesis *Chem. Rev.* **2014,** *114*, 2587-2693.

(11). Luo, Y., *Handbook of Bond Dissociation Energies in Organic Compounds*. CRC press: Boca Raton, FL, 2003.

(12). Brocks, J. J.; Beckhaus, H.-D.; Beckwith, A. L. J.; Rüchardt, C. Estimation of Bond Dissociation Energies and Radical Stabilization Energies by Esr Spectroscopy *J. Org. Chem.* **1998,** *63*, 1935-1943.

(13). Blanksby, S. J.; Ellison, G. B. Bond Dissociation Energies of Organic Molecules *Acc. Chem. Res.* **2003,** *36*, 255-263.

(14). Northrop, B. H.; Coffey, R. N. Thiol–Ene Click Chemistry: Computational and Kinetic Analysis of the Influence of Alkene Functionality *J. Am. Chem. Soc.* **2012,** *134*, 13804-13817.

(15). Cramer, N. B.; Bowman, C. N. Kinetics of Thiol–Ene and Thiol–Acrylate Photopolymerizations with Real-Time Fourier Transform Infrared *J. Polym. Sci. A: Polym. Chem.* **2001,** *39*, 3311-3319.

(16). Hoyle, C. E.; Lee, T. Y.; Roper, T. Thiol–Enes: Chemistry of the Past with Promise for the Future *J. Polym. Sci. A: Polym. Chem.* **2004,** *42*, 5301-5338.

(17). Donovan, B. R.; Ballenas, J. E.; Patton, D. L. Thiol–Trifluorovinyl Ether (Tfve) Photopolymerization: An on-Demand Synthetic Route to Semifluorinated Polymer Networks *Macromolecules* **2016**, 10.1021/acs.macromol.6b01822.

(18). Li, Q.; Zhou, H.; Hoyle, C. E. The Effect of Thiol and Ene Structures on Thiol–Ene Networks: Photopolymerization, Physical, Mechanical and Optical Properties *Polymer* **2009,** *50*, 2237-2245.

(19). Odian, G. Step Polymerization. In *Principles of Polymerization*, John Wiley & Sons, Inc.: 2004, 39-197.

(20). Xiong, L.; Kendrick, L. L.; Heusser, H.; Webb, J. C.; Sparks, B. J.; Goetz, J. T.; Guo, W.; Stafford, C. M.; Blanton, M. D.; Nazarenko, S.; Patton, D. L. Spray-Deposition and Photopolymerization of Organic–Inorganic Thiol–Ene Resins for Fabrication of Superamphiphobic Surfaces *ACS Appl. Mater. Interfaces* **2014,** *6*, 10763-10774.

(21). Sparks, B. J.; Hoff, E. F. T.; Xiong, L.; Goetz, J. T.; Patton, D. L. Superhydrophobic Hybrid Inorganic–Organic Thiol-Ene Surfaces Fabricated Via Spray-Deposition and Photopolymerization *ACS Appl. Mater. Interfaces* **2013,** *5*, 1811-1817.

(22). Meng, Y.; Tsai, M.; Schmidt, G. R.; Anthamatten, M. Gradient-Index Materials Based on Thiol–Ene Networks *ACS Appl. Mater. Interfaces* **2015,** *7*, 8601-8605.

(23). Bhagat, S. D.; Chatterjee, J.; Chen, B.; Stiegman, A. E. High Refractive Index Polymers Based on Thiol–Ene Cross-Linking Using Polarizable Inorganic/Organic Monomers *Macromolecules* **2012,** *45*, 1174-1181.

(24). Amato, D. V.; Amato, D. N.; Flynt, A. S.; Patton, D. L. Functional, Sub-100 Nm Polymer Nanoparticles Via Thiol-Ene Miniemulsion Photopolymerization *Polym. Chem.* **2015,** *6*, 5625-5632.

(25). Durham, O. Z.; Krishnan, S.; Shipp, D. A. Polymer Microspheres Prepared by Water-Borne Thiol–Ene Suspension Photopolymerization *ACS Macro Lett.* **2012,** *1*, 1134-1137.

(26). Amato, D. N.; Amato, D. V.; Mavrodi, O. V.; Braasch, D. A.; Walley, S. E.; Douglas, J. R.; Mavrodi, D. V.; Patton, D. L. Destruction of Opportunistic Pathogens Via Polymer Nanoparticle-Mediated Release of Plant-Based Antimicrobial Payloads *Adv. Healthc. Mater.* **2016,** *5*, 1094-1103.

(27). Du, H.; Zha, G.; Gao, L.; Wang, H.; Li, X.; Shen, Z.; Zhu, W. Fully Biodegradable Antibacterial Hydrogels Via Thiol-Ene "Click" Chemistry *Polym. Chem.* **2014,** *5*, 4002-4008.

(28). Caldwell, S.; Johnson, D. W.; Didsbury, M. P.; Murray, B. A.; Wu, J. J.; Przyborski, S. A.; Cameron, N. R. Degradable Emulsion-Templated Scaffolds for Tissue Engineering from Thiol-Ene Photopolymerisation *Soft Matter* **2012,** *8*, 10344-10351.

(29). Lovelady, E.; Kimmins, S. D.; Wu, J.; Cameron, N. R. Preparation of Emulsion-Templated Porous Polymers Using Thiol-Ene and Thiol-Yne Chemistry *Polym. Chem.* **2011,** *2*, 559-562.

(30). Nair, D. P.; Cramer, N. B.; Scott, T. F.; Bowman, C. N.; Shandas, R. Photopolymerized Thiol-Ene Systems as Shape Memory Polymers *Polymer* **2010,** *51*, 4383-4389.

(31). Ware, T. H.; Perry, Z. P.; Middleton, C. M.; Iacono, S. T.; White, T. J. Programmable Liquid Crystal Elastomers Prepared by Thiol–Ene Photopolymerization *ACS Macro Lett.* **2015,** *4*, 942-946.

(32). Sangermano, M.; Bongiovanni, R.; Malucelli, G.; Priola, A.; Harden, A.; Rehnberg, N. Synthesis of New Fluorinated Allyl Ethers for the Surface Modification of Thiol–Ene Ultraviolet-Curable Formulations *J. Polym. Sci. A: Polym. Chem.* **2002,** *40*, 2583-2590.

(33). Kinloch, A. J. The Science of Adhesion *J. Mater. Sci.* **1980,** *15*, 2141-2166.

(34). Wilker, J. J. Biomatierls: Redox and Adhesion on the Rocks *Nat. Chem. Biol.* **2011,** *7*, 579-580.

(35). Hiemenz, P. C.; Lodge, T. P., *Polymer Chemistry*. 2nd ed.; Taylor & Francis Group: Florida, 2007.

(36). Awaja, F.; Gilbert, M.; Kelly, G.; Fox, B.; Pigram, P. J. Adhesion of Polymers *Prog. Polym. Sci.* **2009,** *34*, 948-968.

(37). Gupta, B. S.; Reiniati, I.; Laborie, M.-P. G. Surface Properties and Adhesion of Wood Fiber Reinforced Thermoplastic Composites *Colloid Surface A* **2007,** *302*, 388-395.

(38). Awaja, F.; Gilbert, M.; Kelly, G.; Fox, B.; Pigram, P. J. Adhesion of Polymers *Progress in Polymer Science* **2009,** *34*, 948-968.

(39). Autumn, K. Gecko Adhesion: Structure, Function, and Applications *MRS Bulletin* **2007,** *32*, 473-478.

(40). Autumn, K.; Peattie, A. M. Mechanisms of Adhesion in Geckos *Integr. Comp. Biol.* **2002,** *42*, 10801-1090.

(41). Huber, G.; Mantz, H.; Spolenak, R.; Mecke, K.; Jacobs, K.; Gorb, S. N.; Arzt, E. Evidence for Capillarity Contributions to Gecko Adhesion from Single Spatula Nanomechanical Measurements *PNAS* **2005,** *45*, 16293-16296.

(42). Boesel, L. F.; Greiner, C.; Arzt, E.; del Campo, A. Gecko-Inspired Surfaces: A Path to Strong and Reversible Dry Adhesives *Adv. Mater.* **2010,** *22*, 2125-2137.

(43). Kwak, M. K.; Pang, C.; Jeong, H.-E.; Kim, H.-N.; Yoon, H.; Jung, H.-S.; Suh, K.-Y. Towards the Next Level of Bioinspired Dry Adhesives: New Designs and Applications *Adv. Func. Mater.* **2011,** *21*, 3606-3616.

(44). Kamperman, M.; Kroner, E.; del Campo, A.; McMeeking, R. M.; Arzt, E. Functional Adhesive Surfaces with "Gecko" Effect: The Concept of Contact Splitting *Adv. Eng. Mater.* **2010,** *12*, 335-348.

(45). Yu, M.; Hwang, J.; Deming, T. J. Role of L-3,4-Dihydroxyphenylalanine in Mussel Adhesive Proteins *J. Am. Chem. Soc.* **1999,** *121*, 5825-5826.

(46). Lee, P. B.; Messersmith, P. B.; Israelachvili, J. N.; Waite, J. H. Mussel-Inspired Adhesives and Coatings *Annu. Rev. Mater. Res.* **2011,** *41*, 99-132.

(47). Moulay, S. Dopa/Catechol-Tethered Polymers: Bioadhesives and Biomimetic Adhesive Materials *Polym. Rev.* **2014,** *54*, 436-513.

(48). Faure, E.; Falentin-Daudré, C.; Jérôme, C.; Lyskawa, J.; Fournier, D.; Woisel, P.; Detrembleur, C. Catechols as Versatile Platforms in Polymer Chemistry *Prog. Polym. Sci.* **2013,** *38*, 236-270.

(49). Yu, J.; Wei, W.; Menyo, M. S.; Masic, A.; Waite, J. H.; Israelachvili, J. N. Adhesion of Mussel Foot Protein-3 to Tio2 Surfaces: The Effect of Ph *Biomacromolecules* **2013,** *14*, 1072-1077.

(50). Lana-Villarreal, T.; Rodes, A.; Pérez, J. M.; Gómez, R. A Spectroscopic and Electrochemical Approach to the Study of the Interactions and Photoinduced Electron Transfer between Catechol and Anatase Nanoparticles in Aqueous Solution *J. Am. Chem. Soc.* **2005,** *127*, 12601-12611.

(51). Lee, H.; Scherer, N. F.; Messersmith, P. B. Single-Molecule Mechanics of Mussel Adhesion *PNAS* **2006,** *103*, 12999-13003.

(52). Akemi Ooka, A.; Garrell, R. L. Surface-Enhanced Raman Spectroscopy of Dopa-Containing Peptides Related to Adhesive Protein of Marine Mussel, Mytilus Edulis *Biopolymers* **2000,** *57*, 92-102.

(53). Wang, J.; Tahir, M. N.; Kappl, M.; Tremel, W.; Metz, N.; Barz, M.; Theato, P.; Butt, H. Influence of Binding-Site Density in Wet Bioadhesion *Adv. Mater.* **2008,** *20*, 3872-3876.

(54). Dreyer, D. R.; Miller, D. J.; Freeman, B. D.; Paul, D. R.; Bielawski, C. W. Perspectives on Poly(Dopamine) *Chem. Sci.* **2013,** *4*, 3796-3802.

(55). Liu, Y.; Ai, K.; Lu, L. Polydopamine and Its Derivative Materials: Synthesis and Promising Applications in Energy, Environmental, and Biomedical Fields *Chem. Rev.* **2014,** *114*, 5057-5115.

(56). Lee, H.; Dellatore, S. M.; Miller, W. M.; Messersmith, P. B. Mussel-Inspired Surface Chemistry for Multifunctional Coatings *Science* **2007,** *318*, 426-430.

(57). Petrie, E. M. Environment, Production, Applications. In *Handbook of Adhesives and Sealants*, 2 ed.; McGraw-Hill: New York, New York, 2007.

(58). Schneberger, G. L. Polymer Structure and Adhesive Behavior. In *Adhesives and Manufacturing*, Marcel Dekker: New York, New York, 1983.

(59). Li, Y.; Qin, M.; Li, Y.; Cao, Y.; Wang, W. Single Molecule Evidence for the Adaptive Binding of Dopa to Different Wet Surfaces *Langmuir* **2014,** *30*, 4358-4366.

(60). Mian, S. A.; Yang, L.-M.; Saha, L. C.; Ahmed, E.; Ajmal, M.; Ganz, E. A Fundamental Understanding of Catechol and Water Adsorption on a Hydrophilic Silica Surface: Exploring the Underwater Adhesion Mechanism of Mussels on an Atomic Scale *Langmuir* **2014,** *30*, 6906-6914.

(61). Akdogan, Y.; Wei, W.; Huang, K.-Y.; Kageyama, Y.; Danner, E. W.; Miller, D. R.; Martinez Rodriguez, N. R.; Waite, J. H.; Han, S. Intrinsic Surface-Drying Properties of Bioadhesive Proteins *Angew. Chem. Int. Ed.* **2014,** *53*, 11253-11256.

(62). Maier, G. P.; Rapp, M. V.; Waite, J. H.; Israelachvili, J. N.; Butler, A. Adaptive Synergy between Catechol and Lysine Promotes Wet Adhesion by Surface Salt Displacement *Science* **2015,** *349*, 628-632.

(63). Maier, G. Low Dielectric Constant Polymers for Microelectronics *Prog. Polym. Sci.* **2001,** *26*, 3-65.

(64). Scheirs, J., *Modern Fluoropolymers*. Wiley: New York, 1997.

(65). Améduri, B.; Boutevin, B.; Kostov, G. Fluoroelastomers: Synthesis, Properties and Applications *Prog. Polym. Sci.* **2001,** *26*, 105-187.

(66). Liu, F.; Hashim, N. A.; Liu, Y.; Abed, M. R. M.; Li, K. Progress in the Production and Modification of Pvdf Membranes *J. Membrane Sci.* **2011,** *375*, 1-27.

(67). Cui, Z.; Drioli, E.; Lee, Y. M. Recent Progress in Fluoropolymers for Membranes *Prog. Polym. Sci.* **2014,** *39*, 164-198.

(68). Vitale, A.; Bongiovanni, R.; Ameduri, B. Fluorinated Oligomers and Polymers in Photopolymerization *Chem. Rev.* **2015,** *115*, 8835-8866.

(69). Arcella, V.; Ghielmi, A.; Tommasi, G. High Performance Perfluoropolymer Films and Membranes *Ann. N.Y. Acad. Sci.* **2003,** *984*, 226-244.

(70). Feiring, A. E. Fluoroplastics. In *Organofluorine Chemistry: Principles and Commercial Applications*, Banks, R. E.; Smart, B. E.; Tatlow, J. C., Eds. Springer US: Boston, MA, 1994, 339-372.

(71). Hirao, A.; Sugiyama, K.; Yokoyama, H. Precise Synthesis and Surface Structures of Architectural Per- and Semifluorinated Polymers with Well-Defined Structures *Prog. Polym. Sci.* **2007,** *32*, 1393-1438.

(72). Dhara, M. G.; Banerjee, S. Fluorinated High-Performance Polymers: Poly(Arylene Ether)S and Aromatic Polyimides Containing Trifluoromethyl Groups *Prog. Polym. Sci.* **2010,** *35*, 1022-1077.

(73). Asandei, A. D. Photomediated Controlled Radical Polymerization and Block Copolymerization of Vinylidene Fluoride *Chem. Rev.* **2016,** *116*, 2244-2274.

(74). Montefusco, F.; Bongiovanni, R.; Sangermano, M.; Priola, A.; Harden, A.; Rehnberg, N. New Difunctional Fluoro-Epoxide Monomers: Synthesis, Photopolymerization and Characterization *Polymer* **2004,** *45*, 4663-4668.

(75). Bongiovanni, R.; Medici, A.; Zompatori, A.; Garavaglia, S.; Tonelli, C. Perfluoropolyether Polymers by Uv Curing: Design, Synthesis and Characterization *Polym. Int.* **2012,** *61*, 65-73.

(76). Kim, J.; Rolland, J. P.; Carbonell, R. G.; DeSimone, J. M. Ultrathin Cross-Linked Perfluoropolyether Film Coatings from Liquid Co2 and Subsequent Uv Curing *CHem. Mater.* **2010,** *22*, 2411-2413.

(77). Priola, A.; Bongiovanni, R.; Malucelli, G.; Pollicino, A.; Tonelli, C.; Simeone, G. Uv-Curable Systems Containing Perfluoropolyether Structures: Synthesis and Characterisation *Macromol. Chem. Phys.* **1997,** *198*, 1893-1907.

(78). Liu, C.; Nie, J.; He, Y. High Compatible Free Radical Uv-Curable Fluorine-Containing Polyacrylic Acrylate Prepolymer *J. Fluor. Chem.* **2015,** *173*, 47-54.

(79). Lin, H.; Wan, X.; Jiang, X.; Wang, Q.; Yin, J. A "Thiol-Ene" Photo-Curable Hybrid Fluorinated Resist for the High-Performance Replica Mold of Nanoimprint Lithography (Nil) *J. Mater. Chem.* **2012,** *22*, 2616-2623.

(80). Harris, J. F.; Stacey, F. W. The Free Radical Addition of Trifluoromethanethiol to Fluoroolefins *J. Am. Chem. Soc.* **1960,** *83*, 840-844.

(81). Harris, J. F. The Free Radical Addition of Hydrogen Sulfide to Fluoroethylenes *J. Am. Chem. Soc.* **1962,** *84*, 3148-3153.

CHAPTER II – THIOL-ENE ADHESIVES FROM CLOVE OIL DERIVATIVES

2.1 Abstract

Chapter II reports the synthesis of catechol-functionalized thiol-ene polymer networks as photocurable adhesives, where the adhesive interactions are derived from 4-allylpyrocatechol – a monofunctional alkene readily obtained from natural products of Syzygium aromaticum flower buds (clove). The thiol-ene photopolymerization process enables rapid cure times, low energy input, and solvent-free processing. The resulting polymer networks show improved macroscopic adhesion to a variety of substrates – including glass, marble, aluminum, and steel – by varying the concentration of 4-allylpyrocatechol in the network. Additionally, the effects of the catechol moiety on polymerization kinetics, thermomechanical, and mechanical properties were determined by comparing the synthesized catechol moiety to a series of control monomers such as eugenol (one phenol group) and methyl eugenol (no phenol group).

2.2 Introduction

The use of commercial adhesives is ever growing due to their cost effectiveness, high design flexibility, and ability to join dissimilar materials.[1] Because of these features, adhesives have found use everywhere from the household to aerospace applications. Simultaneously, the global culture, both industrially and academically, is beginning to make a conscious effort to further the use of environmentally friendly and sustainable processes and products. Naturally, the adhesive industry has followed suit and research in bio-inspired adhesives has moved rapidly forward in the past decade. Several examples of robust adhesive systems exist in nature, including that of the marine mussel, which is characterized by its unique ability to bond under wet, harsh, intertidal conditions to

21

complex heterogeneous substrates. While this naturally occurring adhesive system

contains a complex variety of proteins,[2] the mussel plaque proteins can contain near 30

mol % of the amino acid 3,4-dihydroxyphenylalanine (DOPA), responsible, in part, for

both the cohesive and adhesive interactions of the mussel's adhesive plaques.[3, 4] The

catechol moiety present in DOPA is capable of adhesive interactions via hydrogen

bonding,[5, 6] π-π aromatic interactions, and metal-ligand complexations,[4, 5, 7, 8] and also

cohesive interactions via di-DOPA linkages[9] by oxidative,[10, 11] enzymatic,[10-12] or redox-

induced radical chemistry.[5, 9, 13] The proteins located in the interfacial plaque of the

mussel's adhesive byssus structure can be harvested however, this process is time

consuming, expensive, and yields minimal material. Alternatively, DOPA-analogues can

be synthesized in a variety of ways to develop biomimetic adhesives, including from

naturally occurring small molecules.[14, 15]

   The earliest work published on synthetic, DOPA-containing polymers focused on

designing synthetic polypeptides,[16-18] and has since expanded to include linear, [19-23] and

crosslinked polymeric systems.[22, 24, 25] While polypeptide synthesis, thermal radical

polymerization, and oxidative crosslinking have been successfully utilized to develop

both bio- and synthetic adhesives,[19, 22] photopolymerization offers several advantages

over conventional radical polymerizations, particularly in the case of elastomers and

thermosets. These advantages include rapid, large area cures, ambient conditions, low

energy requirements, and solvent free compositions. In general, visible or UV

photopolymerization facilitates eco-friendly polymerization processes on a potentially

industrial scale. Recent literature contains several examples of photopolymerized,

DOPA-analogue containing networks. Chung et al.[24] photopolymerized dopamine

methacrylamide and 2-methoxyethyl acrylate copolymers while varying the amount of crosslinker to investigate the effect changes in viscoelastic properties had on wet and dry adhesion. Lightly crosslinked networks showed the highest work of adhesion under wet conditions, while the non-crosslinked system showed the highest work of adhesion under dry conditions. More recently, Xue et al. photopolymerized a monofunctional[25] and multifunctional[26] catechol containing methacrylate monomer, crosslinked with modified poly(vinyl alcohol) – a system showing adhesion strength increases upwards of 150% compared to control samples. Acrylate and methacrylate polymer networks have found common use in a wide range of applications, but in general, yield heterogeneous networks and suffer from oxygen inhibition, resulting in longer cure times.[27]

UV thiol-ene photopolymerizations eliminate some of the drawbacks associated with acrylate or methacrylate polymerizations, including oxygen inhibition and heterogeneous network structure,[28-30] due to the unique thiol-ene polymerization mechanism. Thiol-ene networks form via a free-radical step-growth process facilitated by rapid chain transfer, which generates highly homogenous networks resulting in well-defined physical and mechanical properties, typically reflected by a narrow glass transition (T_g). The well-defined properties of thiol-enes have led to their utilization in a wide range of functional materials[28, 30, 31] including recent work by our group[32] in which dopamine acrylamide (DAm) was incorporated into a thiol-ene network to generate adhesive functionality, and also to investigate how the catechol moiety influenced network properties. Their findings showed that DAm imparted adhesive functionality to the thiol-ene system, while influencing network properties by changes in crosslink density and the amount of internetwork hydrogen bonding. While the work by Sparks et

23

al.[32] was the first to incorporate a DOPA analogue into a thiol-ene network, DAm was not soluble without the use of small amounts of DMF, thus diminishing the eco-friendly aspects of solvent-free photopolymerizations.

In this work, we aim to develop a ternary thiol-ene network, based on a catechol monomer (4-allylpyrocatechol, EugOH) incorporated with pentaerythritol triallyl ether (APE), and pentaerythritol tetra(3-mercaptopropionate) (PETMP). 4-allylpyrocatechol is readily obtained from precursors such as eugenol or methyl eugenol – two natural products predominately extracted from the essential oils of *Syzygium aromaticum* flower buds (commonly known as clove buds) by hydrodistillation.[33, 34] The energy efficiency and solvent-free conditions of photopolymerization, along with adhesive moieties readily available from natural product derivatives, enable the development of an eco-friendly route to thiol-ene adhesives. The robustness of thiol-ene photopolymerizations of APE-PETMP networks makes it an ideal system for studying the influence the catechol moiety has on photopolymerization kinetics, thermomechanical, mechanical, and adhesive properties. To further elucidate the influence of the catechol moiety, analogous APE-PETMP networks will be synthesized containing the monofunctional monomers methyl eugenol (MeEug) and eugenol (Eug).

2.3 Experimental

2.3.1 Materials

All reagents and solvents were obtained at the highest purity available from Aldrich Chemical Co. and used without further purification unless otherwise specified. Methyl eugenol and eugenol were purchased as natural grade from Aldrich. Pentaerythritol triallyl ether (APE), and sodium sulfate were obtained from Sigma-

Aldrich; Irgacure 2022 was obtained from BASF; and pentaerythritol tetra(3-mercaptopropionate) (PETMP) was obtained from Bruno Bock.

2.3.2 Synthesis of Triethylsilane-eugenol (EugTES)

EugTES was synthesized using a modified method developed by Hawker et. al.[15] In a typical reaction, 8.00 g (45 mmol) of methyl eugenol was dissolved into 50 mL of dry toluene and a catalytic amount (0.25 wt%) of tris(pentafluorophenyl)borane (TPFPB), under an N_2 atmosphere, followed by the slow addition of 16 mL (100 mmol, 2.2 mol equiv.) triethylsilane. Methane gas was rapidly evolved as the reaction proceeded. After reaction completion was determined by ^{1}H NMR, the catalyst was removed by passing the reaction mixture through a neutral alumina plug with CH_2Cl_2 as the eluent, followed by removal of solvent under vacuum to recover the pure product as a colorless oil (Yield, 93%); δ_H (300MHz, $CDCl_3$; Me_4Si) 0.70-0.78 (12H, m, CH_2), 0.96-1.01 (18H, t, CH_3), 3.25 (2H, d, CH_2), 5.00-5.05 (2H, m, $CH=CH_2$), 5.87-6.00 (1H, m, $CH=CH_2$), 6.58-6.74 (3H, m, Ar-H); δ_C (300MHz, $CDCl_3$, Me_4Si) 5.06, 6.68, 39.4, 115.3, 120.2, 120.9, 121.3, 133.0, 137.8, 144.9, 146.5. (Appendix B − Figures B1 and B2 for NMR spectra).

2.3.3 Synthesis of 4-allylpyrocatechol (EugOH)

8.00 g EugTES (21 mmol) was dissolved in 10 mL of THF and purged with N_2 for 45 minutes. The solution was then transferred, under N_2, to a reaction vessel containing HCl solution, and mixed rapidly. The reaction proceeded quickly and completion was confirmed via thin layer chromatography. The organic layer was extracted into CH_2Cl_2 and then washed with H_2O, followed by drying and filtration. The solvent was removed via vacuum to recover the pure product as a white solid (Yield, 54%); δ_H (300MHz, $CDCl_3$; Me_4Si) 3.25 (2H, d, CH_2), 5.03-5.08 (2H, m, $CH=CH_2$), 5.24

(1H, s, OH), 5.32 (1H, s, OH), 5.86-5.99 (1H, m, CH=CH$_2$), 6.62-6.81 (3H, m, Ar-H); δ_C

(300MHz, CDCl$_3$, Me$_4$Si) 39.5, 115.4, 115.6, 121.1, 133.4, 137.6, 141.5, 143.3.

(Appendix B – Figures B3 and B4 for NMR spectra).

2.3.4 Film Preparation

Monomer resins were prepared at a 1:1 SH:alkene mol ratio from APE, a

monofunctional alkene, PETMP, and 3 wt.% of a photoinitiator. The alkene ratio was

varied from 0 – 50 mol % of the monofunctional alkenes methyl eugenol, eugenol, and

EugOH. Aluminium Q-panels (A-36 with a smooth mill finish), steel Q-panels (QD-36

with a smooth finish), and white polished venation marble, obtained from Lowe's Home

Improvement, were prepared by wiping away any oils or dust in a downward direction.

Glass substrates were cleaned using acetone and ethanol. Monomer resins, prepared as

previously described, were drawn down across various substrates at a thickness of 2 mils

($\sim$ 50 μm). The samples were subsequently cured for 20 minutes under a medium

pressure mercury UV lamp at an intensity of 15 mW/cm^2.

2.3.5 Adhesion Testing

Cross-hatch adhesion was measured using a Cross-Cut Tape Test Kit by Precision

Guage and Tool Company according to ASTM D-3359.[35] The adhesive properties of the

materials from the cross-hatch test are graded on a scale of 5B to 0B based on

approximate percentage of film removed by the tape. A sample classified as 5B can be

described as a lattice where the edges of the cut films remain completely smooth and

intact. Classes 4B-1B describe the degree in which the film has been removed from the

lattice, where less than 5% of the film is removed in 4B and a sample described as 1B has

35 – 65 % of the film removed from the lattice. If greater than 65% of the film has flaked

or delaminated from the substrate, it is classified as 0B. Quantitative adhesion was measured via a single-lap joint adhesively bonded glass sample according to a modified version of ASTM D-1002.[36] Thiol-ene formulation was applied to glass substrates which were then overlapped (1.0 cm x 25.0 cm) with uniform surface coverage, followed by a 20 minute cure under UV light at an intensity of 15 mW/cm^2. All trials were performed using an MTS Insight material testing machine equipped with a 10 kN load cell, moving with a crosshead speed of 0.5cm/min. At least five trails were performed per sample to obtain a statistical average.

2.3.6 Characterization

A Varian Mercury Plus 300 MHz NMR spectrometer operating at a frequency of 300.13 MHz with VNMR 6.1C software was used for structure analysis of EugTES and EugOH. Kinetic data was obtained using real time FTIR (RT-FTIR) spectroscopy by determining the conversions of the thiol and alkene group functionalities. The RT-FTIR studies were conducted using a Nicolet 8700 spectrometer with a KBr beam splitter and a MCT/A detector with a 320−500 nm filtered ultraviolet light source. Each sample was sandwiched between two NaCl plates and exposed to a UV light with an intensity of approximately 20 mW/cm^2. A series of scans were recorded, where spectra were taken approximately 3 scan/s with a resolution of 4 cm^{-1}. Dynamic mechanical analysis (DMA) was performed using a TA Instruments Q800 dynamic mechanical analyzer in tension film mode equipped with a gas cooling accessory. Samples were secured and the strain applied was 0.05%. Samples were heated from −40 to 60 °C at a ramp rate of 2 °C/min. Mechanical testing was performed using a MTS Insight material testing machine equipped with a 10 kN load cell and pre-set to collect 10 data points per second. Dog

bone samples with cross-sectional dimensions of 0.120 in ± 0.08 in and 0.59 in ± 0.05 in

(thickness and width) were carefully centered in clamps and deformed in tensile mode at

a strain rate of 0.2 in/min. Young's modulus was determined from the initial linear elastic

region of the stress−strain curve. Strain at break was determined concurrently during the

tensile tests.

2.4 Results and Discussion

2.4.1 Synthesis of EugOH

The eugenol and triethylsilane protection/deprotection sequence developed by

Hawker et al.[15], shown in Figure 2.1a, provides a facile and mild synthetic procedure to
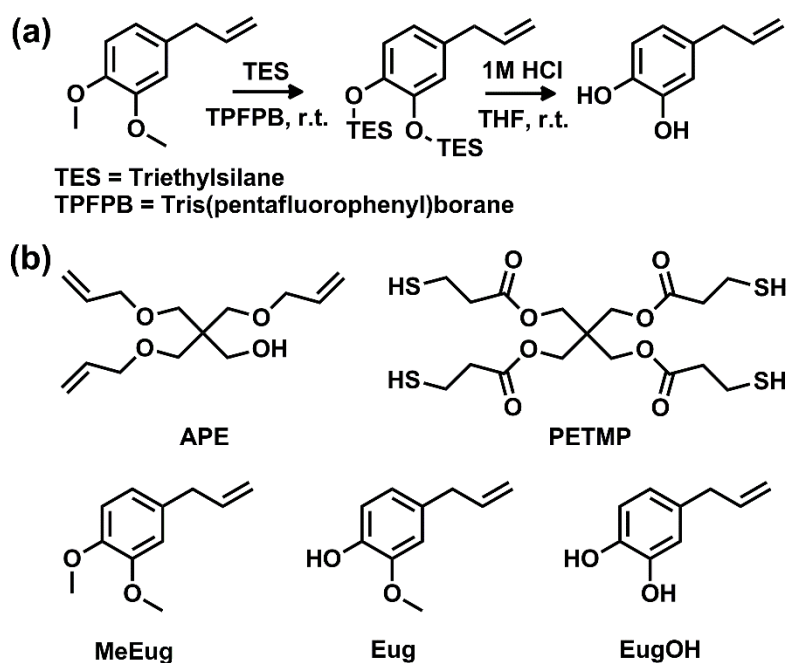
Figure 2.1 (a) Synthetic scheme for the preparation of 4-allylpyrocatechol (EugOH) from methyl eugenol (b) Chemical structures of thiol-ene monomers, including the various clove oil derivatives.

yield an unsaturated catechol monomer. Triethylsilane, in the presence of TPFPB, is

susceptible to nucleophilic attack from both hydroxy and methoxy functional groups,

generating the silyl ether upon release of hydrogen and methane gas.[37] Triethylsilane can

then be easily removed under mild acidic conditions to generate the catechol moiety. The synthesized 4-allylpyrocatechol (for NMR spectra, see Appendix B – Figure B3 and Figure B4), showed improved solubility over acrylamide containing catechol monomers,[24, 32] and was successfully incorporated into thiol-ene resins without the use of additional solvent or heat, maintaining the green aspects of thiol-ene photopolymerization.

2.4.2 Photopolymerization and Kinetics of Ternary Thiol-Ene/EugOH Polymer Networks

Thiol-ene polymer networks, based on a trifunctional alkene and a tetrafunctional thiol, were synthesized containing various mol % of monofunctional alkenes, including methyl eugenol, eugenol, and 4-allylpyrocatechol (Figure 2.1b). All monofunctional alkenes were fully soluble in network precursors. The solubility of the eugenol derivatives in the thiol-ene resin precursors is a major distinction from our previous work with dopamine acrylamide,[32] which was crystalline, insoluble, and required DMF for homogeneous photopolymerization. Catechol and phenol functionalities are powerful radical scavengers making it a common practice to carry out radical-mediated polymerizations using protected versions of catechol monomers.[38] However, recent work by our group and others[25, 26, 32] has demonstrated that it is possible to generate polymer structures in photopolymerizations of our eugenol derivative series. The IR spectra for formulations containing EugOH, pre-polymerization, are shown in Figure 2.2(a), with highlighted thiol and alkene peaks at 2570 cm^{-1} (green box) and 3078 cm^{-1} (blue box), respectively (see Appendix B – Figures B5 and B6 for MeEug and Eug FTIR spectra).

29
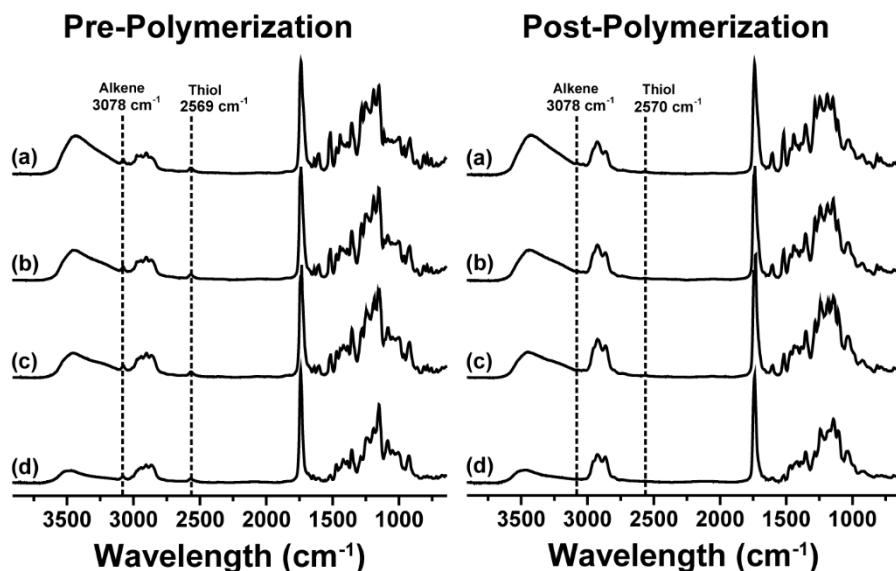
Figure 2.2 FTIR of unpolymerized EugOH-APE-PETMP monomer resins (left) and FTIR of polymerized EugOH-APE-PETMP ternary polymer networks (right). (a) 50% EugOH (b) 35% EugOH (c) 25% EugOH (d) 10% EugOH.

Figure 2.2(b) shows the resulting IR spectra, post UV exposure, of the EugOH formulations and the corresponding disappearance of both the thiol and alkene peak.

Photopolymerization kinetics were monitored in real time, by measuring the change in area of the thiol and alkene peaks upon UV exposure. The change in area was converted to percent conversion values and plotted against time for formulations containing each of the eugenol derivatives. Final conversion values extracted from the conversion plots are presented in Table 2.1. The thiol-ene photopolymerization of networks containing MeEug showed quantitative thiol and alkene conversion at all mol % loadings (Appendix B – Figure B7a). Eug exhibited incomplete conversions only in formulations containing 35 mol % and 50 mol %, with conversion values reaching 95% and 94%, respectively (Appendix B – Figure B7b). The catechol containing EugOH however, showed more significant decreases in conversion with final values decreasing from 89% at 25 mol % loading, down to 80% at 50 mol % loading as shown in Figure
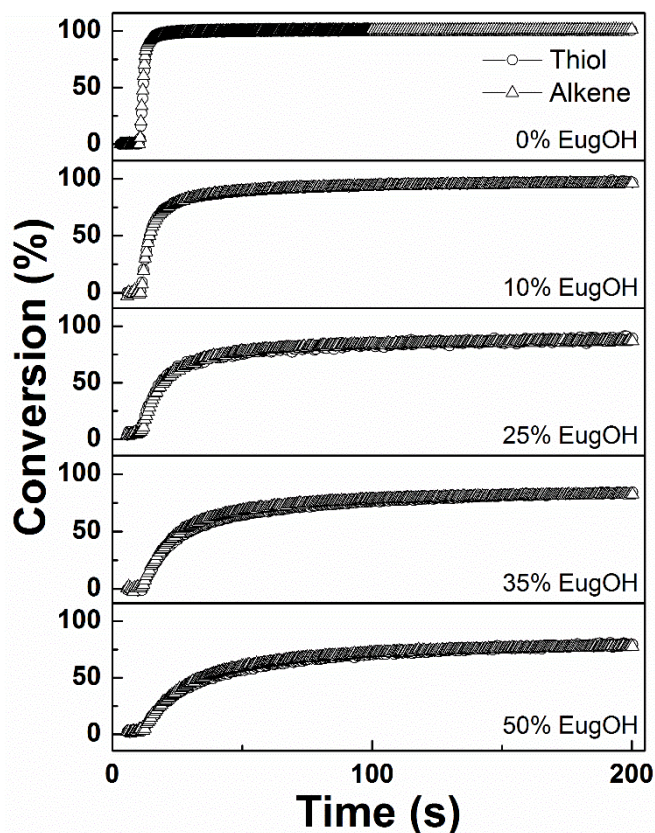
Figure 2.3 Kinetic plots of conversion vs time for EugOH-APE-PETMP thiol networks formulated with 0 to 50 mol % EugOH.

2.3. Figure 2.3 additionally shows evidence of retardation, observed as a decrease in the slope of the initial portion of the RTIR conversion plots. A decrease in initial polymerization rate with increasing EugOH concentrations was observed and can be attributed to the retarding effects of the catechol (similar trends are seen in the Eug system, containing a phenol moiety, but not in the MeEug system, which has no retarding group). The kinetic results are consistent with previous work done in our group using dopamine acrylamide containing thiol-ene networks,[32] as well as recent work by Ai et. al[39] which showed final conversion values and initial rate values decrease as the concentration of a catechol-containing monomer was increased within an acrylate system polymerized by radical-mediated photopolymeization. While retardation becomes more

31

significant at higher concentrations of EugOH, ternary thiol-ene networks were still

effectively formed via UV photopolymerization.

Table 2.1

Conversion percentage values of ternary APE-PETMP networks containing methyl

eugenol, eugenol, and 4-allypyrocatechol.

Monofunctional Monomer	Alkene mol Ratio				
	0:100	10:90	25:75	35:65	50:50
MeEug	>99	>99	>99	98	98
Eug	>99	>99	96	95	94
EugOH	>99	97	89	86	80

2.4.3 Thermomechanical and Mechanical Properties

The thermomechanical properties of the catechol-derivative thiol-ene polymer

networks were investigated using DMA, where the glass transition temperature (T_g) was

determined in strain film mode at a heating rate of 2 °C/min from the peak maximum of

the tan δ curve. T_g values and additional thermomechanical properties of the various

ternary thiol-ene networks are presented in Table 2.2. Figure 2.4 shows the change of the

storage modulus for the EugOH-APE-PETMP networks as a function of temperature. A

clear decrease in the rubbery storage modulus was observed with increasing EugOH

concentrations due to a decrease in crosslink density upon greater incorporation of the

monofunctional monomer in the network. The same trend in rubbery storage modulus

was observed in MeEug (Appendix B − Figure B8) and Eug (Appendix B − Figure B9)

networks. In order to develop a quantitative description of the observed trends in the

rubbery storage modulus, the crosslink density (ρ_x) of the polymer networks was

estimated from the rubbery plateau storage modulus at $T_g + 40$ °C according to the theory

of rubber elasticity,[40] $\rho_x = E'/2(1 + \gamma)RT$, where E' is the rubbery storage modulus at temperature T, R is the gas constant, and γ is Poisson's ratio, which is assumed to be 0.5 for incompressible networks. Crosslink density values decrease with increasing monofunctional monomer content (Table 2.2) and also decrease from MeEug to Eug to EugOH at the equivalent loading percentages. The decreasing conversion with increasing hydroxyl content, and therefore increasing radical scavenging ability, likely contributes to the trends observed in the rubbery plateau regime.

Table 2.2

Thermomechanical properties of ternary APE-PETMP networks containing methyl eugenol, eugenol and 4-allylpyrocatechol.

Alkene Ratio	T_g (°C)	fwhm (°C)[a]	E'Rub, T_g+40 °C (MPa)	ρ_x (10^{-3}mol cm^{-3})[b]
MeEug-APE-PETMP				
0:100	9.3	11.9	29.8	3.71
10:90	4.7	13.0	18.4	2.33
25:75	3.4	12.6	14.6	1.85
35:65	2.4	13.5	8.34	1.06
50:50	-0.67	13.7	1.90	0.244
Eug-APE-PETMP				
0:100	9.3	11.9	29.8	3.71
10:90	1.2	13.1	18.3	2.33
25:75	-0.67	15.9	9.76	1.25
35:65	-0.98	13.3	4.56	0.586
50:50	-1.4	13.8	1.46	0.188
EugOH-APE-PETMP				
0:100	9.3	11.9	29.8	3.71
10:90	-0.71	11.2	15.5	1.99
25:75	-3.0	12.3	4.70	0.608
35:65	-3.8	13.7	3.03	0.393
50:50	-7.2	19.9	0.295	0.0326

afwhm obtained from the tan δ curves; bcrosslink density (ρx)
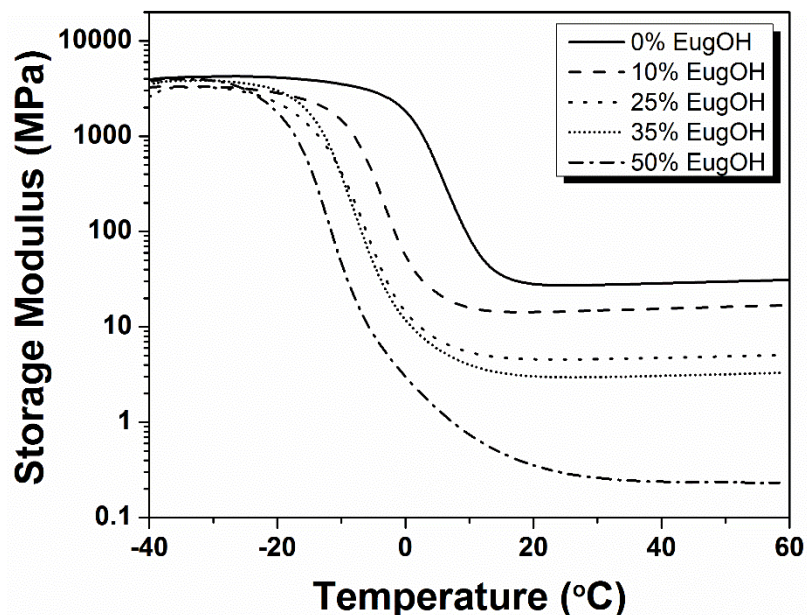
Figure 2.4 Storage modulus vs temperature for the EugOH-APE-PETMP polymer networks with varying concentrations of EugOH (0-50 mol %).

Figure 2.5 shows the tan δ curves for the ternary EugOH-APE-PETMP networks with increasing EugOH concentration. The neat system shows a narrow glass transition temperature at 9.3 °C, which is typical of the APE-PETMP thiol-ene system with comparable loadings of photoinitiator.[41] As the concentration of EugOH is increased, the T_g systematically decreases to -7.2 °C for 50 mol % EugOH. Similar results are observed in both the MeEug and Eug systems, where the T_g decreases to -0.67 °C and -1.4 °C for 50 mol % loadings, respectively (Appendix B – Figures B10 and B11). The systematic decrease in T_g can be attributed to the increasing incorporation of monofunctional monomer and a decrease in crosslink density. The catechol moiety does not provide significant inter-network hydrogen bonding, and its incorporation diminishes the number of chemical crosslinks within the network structure and, hence, decreases the T_g. The EugOH systems show the lowest T_g values at all loading percentages because catechol moiety is also limiting overall monomer conversion, which contributes further to a
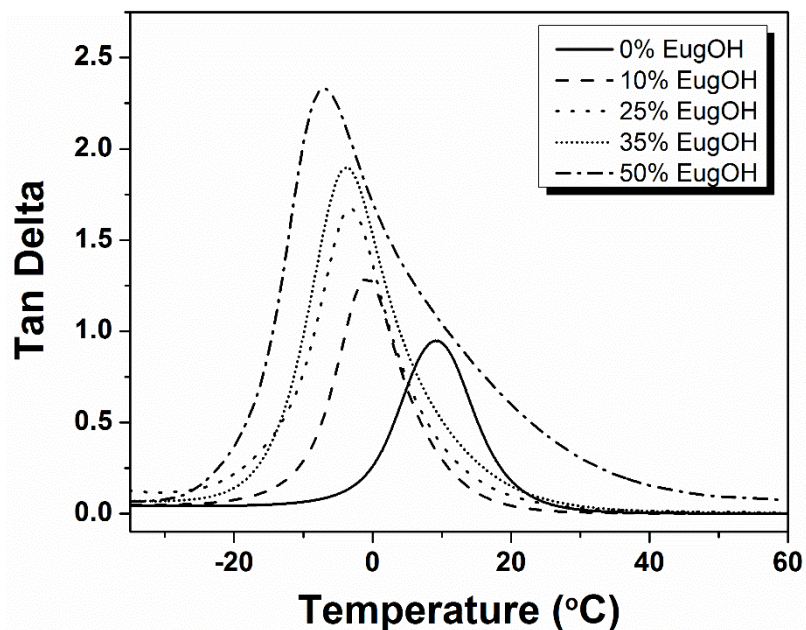
34

Figure 2.5 Tan δ vs temperature for the EugOH-APE-PETMP polymer networks with varying concentrations of EugOH (0-50 mol %).

decrease in chemical crosslinks. The effect of decreased conversion is exemplified in the 50 mol % EugOH-APE-PETMP network, where less complete and less uniform network formation causes a broadening in tan delta peak. These results contrast with our previous work, where we incorporated an amide containing monofunctional catechol monomer into an APE-PETMP network leading to an increase in T_g.[32] The amide provides significant hydrogen bonding sites within the network which act as physical crosslinks and serve to diminish the effect of increasing monofunctional monomer content and decreasing conversion. The lack of an amide in the EugOH systems results in thermomechanical properties being primarily dictated by decreases in crosslink density and conversion.

Young's modulus and elongation at break of the MeEug, Eug, and EugOH containing APE-PETMP networks were studied using tensile tests, and structure-property relationships of the networks were developed as a function of

35
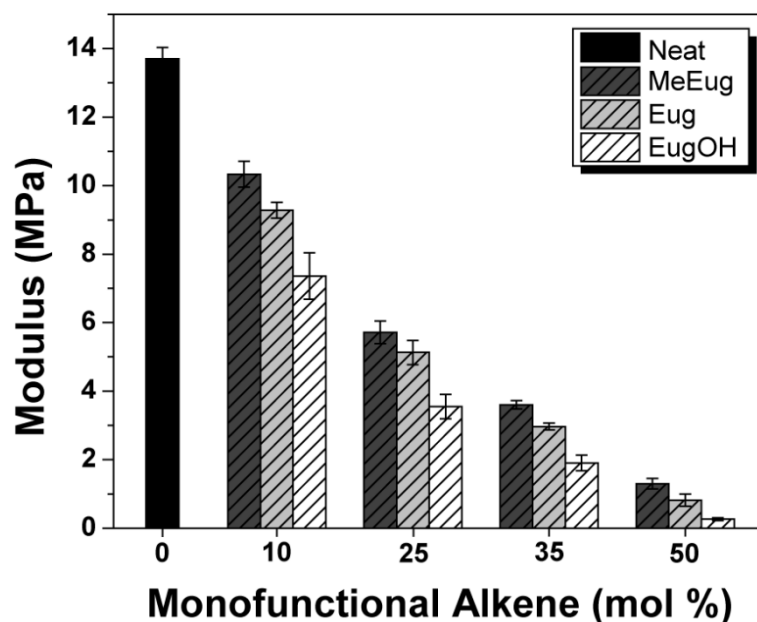
Figure 2.6 Young's modulus of thiol-ene adhesive networks as a function of monofunctional monomer content.

monofunctional monomer loading. Samples were prepared as previously described and cured into dog bones using UV irradiation. The samples were subjected to a strain rate 0.2 in/min and the Young's modulus and strain at break values are shown in Figures 2.6 and 2.7, respectively (numerical values provided in Table 2.3). The neat APE-PETMP system has the highest Young's modulus (13.7 ± 0.33 MPa), and the lowest strain at break (25.6 ± 6.27 %). Upon increasing monofunctional monomer concentration, the modulus begins to decrease and the strain at break gradually increases (until 50 mol %). Both the decrease in modulus and strain at break are attributed to the decrease in crosslink density with increasing monofunctional monomer content. The incorporation of the monofunctional alkene monomers introduces more free chain ends into the network, decreasing rigidity and therefore modulus, while enabling increased chain

36
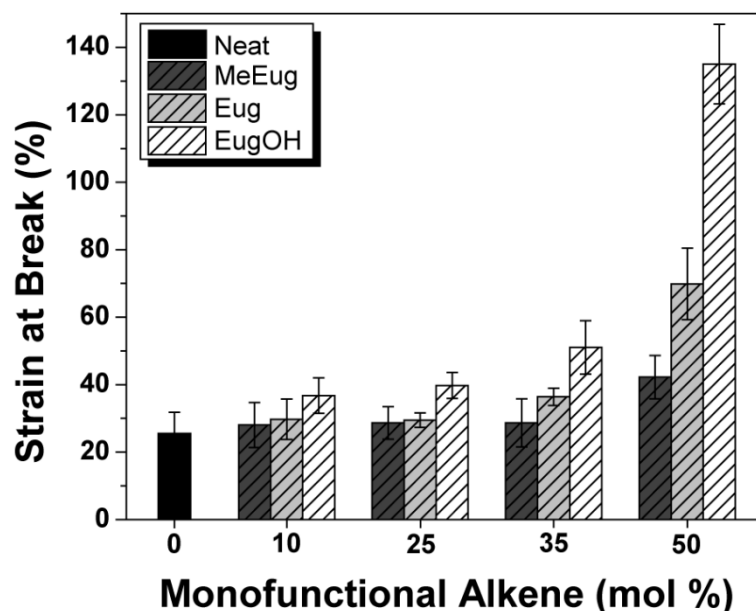
Figure 2.7 Strain at break of thiol-ene adhesive networks as a function of monofunctional monomer content.

rearrangement upon network deformation. For example, the modulus values for

the EugOH system decrease from 7.36 ± 0.68 MPa at 10 mol % loading to $0.266 \pm$

0.039 MPa at 50 mol % loading, while the strain at break values increase from

36.7 ± 5.27 % at 10 mol % loading to 135.0 ± 11.8 % at 50 mol % loading.

Interestingly, the modulus decreases with increasing hydroxyl content in the

monofunctional monomers, while the strain at break simultaneously increases.

MeEug showed the highest modulus values, but lowest strains at break and

contains no phenolic hydroxyl groups, while EugOH showed the lowest modulus

values, and the largest strains at break, containing the dihydroxyl, catechol moiety

(Eug shows intermediate values in both cases). While it may be expected that the

increase in hydroxyl content (MeEug to Eug to EugOH) would lead to increased

hydrogen bonding within the network and therefore higher modulus values, similar

37

to results observed in our thermomechanical testing, the phenolic and catechol

hydroxyl groups lead to radical inhibition that outweighs any potential benefits

from hydrogen bonding by lowering the overall polymerization conversion values.

The decreases in conversion contribute further to a lowering of the crosslink

density and therefore decreases in modulus and increases in strain at break.

EugOH shows the lowest conversion values and crosslink densities thus, while

inter-network hydrogen bonding may be present, the modulus of the ternary thiol-

ene systems is dominated by the change in crosslink density.

Table 2.3

Mechanical properties of ternary APE-PETMP networks containing methyl eugenol,

eugenol and 4-allylpyrocatechol.

Alkene Ratio	Young's Modulus (MPa)	Strain at Break (%)
MeEug-APE-PETMP		
0:100	13.7 ± 0.33	25.6 ± 6.3
10:90	10.3 ± 0.38	28.1 ± 6.6
25:75	5.72 ± 0.33	28.7 ± 4.9
35:65	3.60 ± 0.12	28.7 ± 7.1
50:50	1.30 ± 0.15	42.3 ± 6.4
Eug-APE-PETMP		
0:100	13.7 ± 0.33	25.6 ± 6.3
10:90	9.28 ± 0.23	29.8 ± 6.0
25:75	5.13 ± 0.35	29.5 ± 2.2
35:65	2.97 ± 0.10	36.4 ± 2.6
50:50	0.820 ± 0.18	69.9 ± 10.6
EugOH-APE-PETMP		
0:100	13.7 ± 0.33	25.6 ± 6.3
10:90	7.36 ± 0.68	36.7 ± 5.3
25:75	3.55 ± 0.36	39.7 ± 3.8
35:65	1.90 ± 0.23	51.1 ± 7.9
50:50	0.27 ± 0.39	135.0 ± 11.8

2.4.4 Adhesive Properties

Adhesive behavior is a function of various factors, including chemistry, viscoelastic response, surface preparation, and substrate type. In this study, we wanted to investigate the effect catechol concentration had on the adhesive performance of the thiol-ene films. Using MeEug and Eug as controls should help to deconvolute, to some extent, the adhesive behavior resulting from changes in viscoelastic properties and the adhesive behavior resulting from changes in catechol monomer concentration. As previously described, MeEug, Eug, and EugOH ternary thiol-ene films were drawn down at 2 mils (~50 µm) onto aluminum, steel, glass, and marble substrates, cured, and subjected to the cross-hatch adhesion test.

The results from the cross-hatch adhesion test are summarized in Table 2.4. The neat system, as well as 10 mol % loadings of both the control, MeEug, and phenol containing monomer, Eug, showed similar results, with all films being classified as 0B on all substrate types. The films in each case were completely removed from the substrates as a result of the adhesion test. Both MeEug and Eug demonstrate increasing adhesion to steel and marble from 25 to 50 mol % loading, with Eug showing a higher rating for adhesion, having films classified at 2B at 25 mol % to 4B at 50 mol%. Because the MeEug system has no adhesive moiety, the increase in adhesion can be attributed to the change in viscoelastic properties. As the mol % of MeEug increases, the T_g decreases, leading to a tackier resin capable of more mechanical interlocking on the rough steel surface and porous marble surface. These viscoelastic changes do not lead to measureable increases in adhesion on glass or aluminium (until 50 mol %) because they are much smoother surfaces, and lack significant sites to facilitate mechanical adhesion.

This same effect is observed in the Eug system, as the T_g decreases with increasing

loading percentage, the adhesion values increase on steel and marble, but not aluminium

or glass (until 50 mol %). The adhesion values for Eug, however, are greater when

compared to the MeEug system due to the presence of the single hydroxyl moiety of Eug,

capable of hydrogen bonding interactions with the substrate surface. While viscoelastic

properties likely contribute to the increase in adhesion for the Eug system, the magnitude

of change in the T_g values between MeEug and Eug at the various loading percentages

are likely not significant enough to cause observable changes in adhesion.

Table 2.4

Cross-hatch adhesion results for methyl eugenol, eugenol, and 4-allylpyrocatechol

ternary polymer networks based on APE-PETMP on various substrates.

Thiol-Ene System	Aluminum	Glass	Steel	Marble
MeEug-APE-PETMP				
10:90	0B	0B	0B	0B
25:75	0B	0B	1B	1B
35:65	0B	0B	1B	3B
50:50	1B	1B	3B	3B
Eug-APE-PETMP				
10:90	0B	0B	0B	0B
25:75	0B	0B	2B	2B
35:65	0B	0B	3B	3B
40:40	2B	1B	4B	4B
EugOH-APE-PETMP				
10:90	0B	2B	1B	0B
25:75	1B	3B	2B	1B
35:65	4B	3B	4B	4B
50:50	5B	5B	5B	5B

The EugOH-APE-PETMP system, containing the known adhesive catechol

moiety, shows significant increases in adhesion. The EugOH films show enhanced

adhesion on all substrates at all loading percentages, compared to MeEug and Eug.

Knowing the glass substrate is smooth compared to the other substrates, and strong adhesion was not observed for the MeEug and Eug systems, the increase in adhesion may be attributed to chemical interaction between the glass surface and the catechol moiety. The EugOH films on glass are classified from 2B at 10 mol % to 5B at 50 mol %, significantly higher than the MeEug and Eug analogues. Similar results were observed on the other substrates as well, with adhesion values reaching 4B at 35 mol % and 5B at 50 mol % on aluminium, steel, and marble. Only light flaking was observed for films at 4B, while the 5B films remain perfectly intact, showing strong adhesion performance.

Additionally, lap shear adhesion testing was performed to develop a more thorough understanding of our thiol-ene adhesives. Due to our use of UV photopolymerization, only glass substrates were able to be prepared for lap shear testing. However, lap shear adhesion testing combined with cross-hatch adhesion testing helps to elucidate and understand both the interfacial adhesive interactions, and the bulk cohesive interactions at work within our thiol-ene thin films. As shown in Figure 2.8, the EugOH system out-performs the MeEug and Eug systems at all mol % of monofunctional monomer loading, reaching an adhesion value of 1.8 ± 0.15 MPa at 50 mol % EugOH; significantly higher than the neat APE-PETMP system (0.93 ± 0.090 MPa). The Eug system shows slightly increased adhesion values from the neat system, but plateaus at approximately 1.1 MPa. The MeEug system however, shows the opposite trend; as the concentration of MeEug in the system is increased, a decrease in adhesion is observed. At first, this appears contradictory to our cross-hatch results. However, lap shear adhesion also probes bulk cohesive interactions, which change as we incorporate more of the monofunctional alkene (i.e. the crosslink density is decreasing). Because MeEug has

41

no significant chemical interaction with the substrate interface, and its crosslink density and modulus are being systematically decreased with increasing monofunctional monomer concentration, lower adhesion values are observed at higher mol % incorporation. The bulk material is becoming weaker, and with no increase in interfacial interaction like that observed for the Eug system, and more prominently, the EugOH system, the MeEug thiol-ene adhesive fails at lower forces.
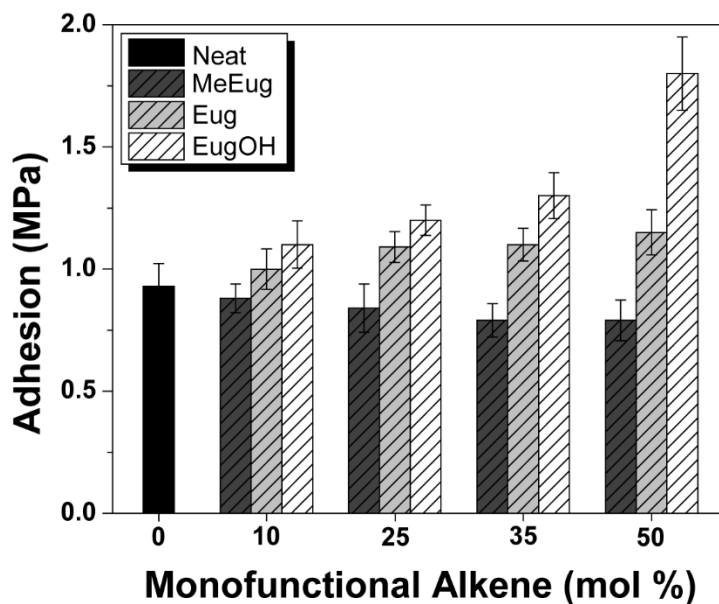
Figure 2.8 Lap shear adhesion values for methyl eugenol, eugenol, and 4-allylpyrocatechol ternary polymer networks.

2.5 Conclusions

We have demonstrated the synthesis of catechol-functionalized thiol-ene polymer networks as photocurable adhesives, where the adhesive interactions are derived from 4-allylpyrocatechol – a monofunctional alkene readily obtained from natural products of *Syzygium aromaticum* flower buds (clove). The thiol-ene photopolymerization process enables rapid cure times, low energy input, and solvent-free processing. Increasing the concentration of EugOH in the thiol-ene networks resulted in improved adhesion on a

42

variety of substrates, including glass, aluminium, steel, and marble. In addition, EugOH networks were studied in comparison to networks containing eugenol and methyl eugenol. These comparative studies illuminate the role catechol plays in dictating polymerization kinetics, mechanical, and thermomechanical properties, and adhesion in these thiol-ene materials. While adhesive properties have been imparted to the model APE-PETMP thiol-ene resin by incorporating a natural product catechol containing monomer, this same synthetic technique could be applied to variety of network materials leading to the generation of photocurable sealants, hydrogels, and adhesives for dental, biomedical, and advanced applications based on sustainable chemistries.

Reproduced from Donovan, B. R.; Cobb, J. S.; Hoff, E. F. T.; Patton, D. L. Thiol-ene adhesives from clove oil derivatives *RSC Advances* **2014**, *4*, 61927-61935 with permission from the Royal Society of Chemistry.

2.6 References

(1). Kinloch, A. J. The Science of Adhesion *J. Mater. Sci.* **1980,** *15*, 2141-2166.

(2). Zhao, H.; Waite, J. H. *J. Biol. Chem.* **2006,** *281*, 26150-26158.

(3). Waite, J. H.; Tanzer, M. L. Polyphenolic Substance of Mytilus Edulis: Novel Adhesive Containing L-Dopa and Hydroxyproline *Science* **1981,** *212*, 1038-1040.

(4). Lee, P. B.; Messersmith, P. B.; Israelachvili, J. N.; Waite, J. H. Mussel-Inspired Adhesives and Coatings *Annu. Rev. Mater. Res.* **2011,** *41*, 99-132.

(5). Lana-Villarreal, T.; Rodes, A.; Pérez, J. M.; Gómez, R. A Spectroscopic and Electrochemical Approach to the Study of the Interactions and Photoinduced Electron Transfer between Catechol and Anatase Nanoparticles in Aqueous Solution *J. Am. Chem. Soc.* **2005,** *127*, 12601-12611.

(6). Mian, S. A.; Gao, X.; Nagase, S.; Jang, J. Adsorption of Catechol on a Wet Silica Surface: Density Functional Theory Study *Theor. Chem. Acc.* **2011,** *130*, 333-339.

(7). Akemi Ooka, A.; Garrell, R. L. Surface-Enhanced Raman Spectroscopy of Dopa-Containing Peptides Related to Adhesive Protein of Marine Mussel, Mytilus Edulis *Biopolymers* **2000,** *57*, 92-102.

(8). Wang, J.; Tahir, M. N.; Kappl, M.; Tremel, W.; Metz, N.; Barz, M.; Theato, P.; Butt, H. Influence of Binding-Site Density in Wet Bioadhesion *Adv. Mater.* **2008,** *20*, 3872-3876.

(9). Monahan, J.; Wilker, J. J. Cross-Linking the Protein Precursor of Marine Mussel Adhesives: Bulk Measurements and Reagents for Curing *Langmuir* **2004,** *20*, 3724-3729.

(10). Suci, P. A.; Geesey, G. G. Influence of Sodium Periodate and Tyrosinase on Binding of Alginate to Adlayers of Mytilus Edulis Foot Protein 1 *J. Colloid. Inter. Sci.* **2000,** *230*, 340-348.

(11). Fant, C.; Sott, K.; Elwing, H.; Hook, F. Adsorption Behavior and Enzymatically or Chemically Induced Cross-Linking of a Mussel Adhesive Protein *Biofouling* **2000,** *16*, 119-132.

(12). Burzio, L. A.; Waite, J. H. Cross-Linking in Adhesive Quinoproteins: Studies with Model Decapeptides† *Biochemistry* **2000,** *39*, 11147-11153.

(13). Hight, L. M.; Wilker, J. J. Synergistic Effects of Metals and Oxidants in the Curing of Marine Mussel Adhesive *J. Mater. Sci.* **2007,** *42*, 8934-8942.

(14). Vendamme, R.; Schüwer, N.; Eevers, W. Recent Synthetic Approaches and Emerging Bio-Inspired Strategies for the Development of Sustainable Pressure-Sensitive Adhesives Derived from Renewable Building Blocks *J. Appl. Polym. Sci.* **2014,** *131*, 40669-40685.

(15). Heo, J.; Kang, T.; Jang, S. G.; Hwang, D. S.; Spruell, J. M.; Killops, K. L.; Waite, J. H.; Hawker, C. J. Improved Performance of Protected Catecholic Polysiloxanes for Bioinspired Wet Adhesion to Surface Oxides *J. Am. Chem. Soc.* **2012,** *134*, 20139-20145.

(16). Yu, M.; Deming, T. J. Synthetic Polypeptide Mimics of Marine Adhesives *Macromolecules* **1998,** *31*, 4739-4745.

(17). Tatehata, H.; Mochizuki, A.; Kawashima, T.; Yamashita, S.; Yamamoto, H. Model Polypeptide of Mussel Adhesive Protein. I. Synthesis and Adhesive Studies of Sequential Polypeptides (X-Tyr-Lys)N and (Y-Lys)N *J. Appl. Polym. Sci.* **2000,** *76*, 929-937.

(18). Yu, M.; Hwang, J.; Deming, T. J. *J. Am. Chem. Soc.* **1999,** *121*, 5825-5826.

(19). Matos-Pérez, C. R.; White, J. D.; Wilker, J. J. Polymer Composition and Substrate Influences on the Adhesive Bonding of a Biomimetic, Cross-Linking Polymer *J. Am. Chem. Soc.* **2012,** *134*, 9498-9505.

(20). Stepuk, A.; Halter, J. G.; Schaetz, A.; Grass, R. N.; Stark, W. J. *Chem. Commun.* **2012,** *48*, 6238-6240.

(21). Ma, W.; Xu, H.; Takahara, A. Substrate-Independent Underwater Superoleophobic Surfaces Inspired by Fish-Skin and Mussel-Adhesives *Adv. Mater. Inter.* **2014,** *1*, 1300092-1300097.

(22). Meredith, H. J.; Jenkins, C. L.; Wilker, J. J. Enhancing the Adhesion of a Biomimetic Polymer Yields Performance Rivaling Commercial Glues *Adv. Func. Mater.* **2014,** *24*, 3259-3267.

(23). White, E. M.; Seppala, J. E.; Rushworth, P. M.; Ritchie, B. W.; Sharma, S.; Locklin, J. Switching the Adhesive State of Catecholic Hydrogels Using Phototitration *Macromolecules* **2013,** *46*, 8882-8887.

(24). Chung, H.; Glass, P.; Pothen, J. M.; Sitti, M.; Washburn, N. R. Enhanced Adhesion of Dopamine Methacrylamide Elastomers Via Viscoelasticity Tuning *Biomacromolecules* **2010,** *12*, 342-347.

(25). Xue, J.; Wang, T.; Nie, J.; Yang, D. Preparation and Characterization of a Bioadhesive with Poly (Vinyl Alcohol) Crosslinking Agent *J. Appl. Polym. Sci.* **2013,** *127*, 5051-5058.

(26). Xue, J.; Wang, T.; Nie, J.; Yang, D. Preparation and Characterization of a Photocrosslinkable Bioadhesive Inspired by Marine Mussel *J. Photoch. Photobio. B* **2013,** *119*, 31-36.

(27). Schwalm, R., *Uv Coatings: Basic, Recent Developments and New Applications*. Elsevier: Amsterdam: London, 2007.

(28). Hoyle, C. E.; Bowman, C. N. Thiol-Ene Click Chemistry *Angew. Chem. Int. Ed.* **2010,** *49*, 1540-1573.

(29). Hoyle, C. E.; Lee, T. Y.; Roper, T. J. *J. Polym. Sci. A: Polym. Chem.* **2004,** *42*, 5301-5338.

(30). Hoyle, C. E.; Lowe, A. B.; Bowman, C. N. *Chem. Soc. Rev.* **2010,** *39*, 1355-1387.

(31). Lowe, A. B. Thiol-Ene "Click" Reactions and Recent Applications in Polymer and Materials Synthesis: A First Update *Polym. Chem.* **2014**, 4820-4870.

(32). Sparks, B. J.; Hoff, E. F. T.; Hayes, L. P.; Patton, D. L. *Chem. Mater.* **2012,** *24*, 3633-3642.

(33). Bilel, H.; Hamdi, N.; Zagrouba, F.; Fischmeister, C.; Bruneau, C. Eugenol as a Renewable Feedstock for the Production of Polyfunctional Alkenes Via Olefin Cross-Metathesis *RSC Advances* **2012,** *2*, 9584-9589.

(34). Kamatou, G. P.; Vermaak, I.; Viljoen, A. M. Eugenol—from the Remote Maluku Islands to the International Market Place: A Review of a Remarkable and Versatile Molecule *Molecules* **2012,** *17*, 6953-6981.

(35). Astm D3359-09e2 Standard Test Methods for Measuring Adhesion by Tape Test. ASTM International: West Conshohocken, PA, 2009.

(36). Astm D1002-10 Apparent Shear Strength of Single-Lap-Join Adhesively Bonded Metal Specimens by Tension Loading (Metal-to-Metal). ASTM Internationl: West Conshohocken, PA, 2010.

(37). Blackwell, J. M.; Foster, K. L.; Beck, V. H.; Piers, W. E. B(C6f5)3-Catalyzed

Silation of Alcohols: A Mild, General Method for Synthesis of Silyl Ethers *J. Org.*

Chem. **1999,** *64*, 4887-4892.

(38). Daly, W. H.; Moulay, S. J. *J. Polym. Sci.: Polym. Symp.* **1986,** *74*, 227-242

(39). Ai, Y.; Nie, J.; Wu, G.; Yang, D. The Dopa-Functionalized Bioadhesive with

Properties of Photocrosslinked and Thermoresponsive *J. Appl. Polym. Sci.* **2014**, DOI:

10.1002/app.41102.

(40). Flory, P. J. *Polymer* **1979,** *20*, 1317-1320.

(41). Shin, J.; Nazarenko, S.; Phillips, J.; Hoyle, C. Physical and Chemical Modifications

of Thiol-Ene Networks to Control Activation Energy of Enthalpy Relaxation *Polymer*

2009, *50*, 6281-6286.

CHAPTER III INVESTIGATING THE UTILITY OF HYDROPHOBIC FUNCTIONAL GROUPS IN UNDERWATER ADHESIVES VIA THIOL-ENE CHEMISTRY

3.1 Abstract

Herein, we report the improved adhesive binding of a UV-polymerized, catechol-based thiol-ene network under wet conditions by the incorporation of covalently attached, hydrophobic pendant chains. Networks were prepared containing varying mol percentages of alkyl, ethylene glycol, and perfluoroalkyl pendant chains, and the influence of pendant chain concentration on polymerization kinetics, thermomechanical, and adhesive properties was investigated. Serendipitously, increased concentrations of pendant chains resulted in increased polymerization conversions, mitigating the inhibition effects caused by the presence of a catechol moiety. The increased conversions caused an increase in crosslink density relative to a control network containing no pendant chains. However, increased pendant chain concentration simultaneously caused moderate decreases in network T_g. Adhesion testing revealed that when lap shear adhesion samples were polymerized under water, the inclusion of 50 mol % of a perfluoroalkyl chain facilitated a moderate recovery of adhesion strength relative to a completely dry condition. When adhesion testing was conducted under milder conditions, with polymerizations carried out in atmosphere on wet substrates, the 50 mol % perfluoroalkyl containing network demonstrated a complete recovery of adhesive strength, effectively eliminating the detrimental effects of water on adhesion.

3.2 Introduction

The design and implementation of synthetic, polymer adhesives capable of binding underwater or in aqueous environments has been a persistent and prevalent challenge in the adhesives industry. Due to the polar nature of many adhesives, water may permeate the resin and alter both the bulk and adhesive polymer properties. In the bulk, water acts as a plasticizer and may lower the T_g and modulus of a resin, decreasing its cohesive strength.[1] At the adhesive/substrate interface, water competes for surface binding sites through hydrogen bonding and may displace or delaminate a polymeric adhesive.[2] Commercially, moisture resistance has been imparted to synthetic adhesives by utilizing polymers with low water diffusion coefficients, chemically modifying polymeric adhesives, utilizing primed or prepared substrates, or coating an adhesive joint in water resistant material.[1] Albeit promising, modification of existing polymers or substrates to improve water resistance may be time consuming and costly. Consequently, researchers have turned to nature for inspiration, attempting to elucidate the remarkable underwater binding capabilities of organisms such as the marine mussel[3, 4], sandcastle worm[5], and barnacle.[6, 7] The most widely studied of these natural adhesives has been that of the marine mussel – an organism capable of binding in the harsh, turbulent conditions of an intertidal zone. Though complex, it has been discovered that the presence of the rare amino acid, 3,4-dihydroxyphenylalanine (DOPA), plays a principle role in the naturally occurring adhesive mechanism of the marine mussel.[8, 9] Specifically, the catechol moiety of DOPA has been determined to provide adhesive interactions to a variety of substrates[10, 11] and may bind preferentially to a substrate surface in the presence of water.[12]

In Chapter II, we reported the synthesis of a photopolymerized, catechol-based thiol-ene adhesive that may facilitate the generation of photocurable sealants, hydrogels, and adhesives for dental, biomedical, and advanced applications.[13] While encouraging, no underwater adhesion data was reported due to the inability of the bio-inspired adhesive to achieve sufficient binding strengths in wet conditions. As such, we sought to impart underwater binding to the catechol-based adhesives, and returned to the marine mussel for inspiration. While it has been long understood that DOPA plays a key role in mussel adhesion[3, 4, 14, 15], recent reports detail additional and synergistic mechanisms of action. Most recently, it was discovered that the mussel adhesive proteins contain a number of lysine residues capable of penetrating and replacing the salt layers commonly found on an underwater surface.[16] In this way, the lysine residue acts as a "primer" and readies the substrate surface for catechol binding. In a similar mechanism, it was discovered that the mussel excretes hydrophobic proteins onto a substrate surface to "dry" it before adhesive binding.[17] The presence of hydrophobic groups disrupts the hydration layers surrounding a substrate interface and facilitates stronger and more reliable adhesive binding. Though the natural proteins associated with the mechanisms described above are highly complex, their discovery points to additional modes of action that may be readily mimicked.

The inclusion of lysine-like or ionic residues has been utilized substantially in the development of bio-inspired underwater adhesives and coacervates[5, 18-21] , however, few examples utilize hydrophobic groups to enhance underwater binding strength; those that do focus on the prevention of DOPA oxidation rather than the expulsion of water from the adhesive/substrate interface.[18, 22] Thus, a unique opportunity exists to investigate

synthetic mimics of the mussel's surface drying approach by directly incorporating

chemistries of varying hydrophobicity into adhesive polymer networks. To this task, we

utilize both the advantages of thiol-ene photopolymerization (oxygen and moisture

insensitive polymerizations, and well-defined network structures), and the presence of

thiol functional groups, to selectively and statistically, modify and incorporate pendant

chains of varying hydrophobicity into a catechol-based, adhesive thiol-ene polymer

network. It is believed that the presence of hydrophobic pendant chains will help remove

water from the substrate interface when the adhesive resin is placed in intimate contact

with the substrate, thus improving adhesive binding strength underwater. Further, the use

of thiol-ene photochemistry will enable spatial and temporal control over polymerization,

and the resulting homogeneous network structures will provide insight into the influence

of both the catechol and hydrophobic pendant chains on polymerization kinetics,

thermomechanical properties, and dry and wet adhesive properties.

3.3 Experimental

3.3.1 Materials

All materials were purchased from Sigma Aldrich and used without additional

purification unless specified otherwise. Pentaerythritol tetrakis(3-mercaptopropionate)

[PETMP] and trimethylolpropane tris(3-mercaptopropionate) [TMPMP] were purchased

from Bruno Bock, 2-(perfluorohexyl)ethyl acrylate (F6) was purchased from Oakwood

Chemical, and Darocur 1173 was purchased from BASF.

3.3.2 Synthesis of 4-allylpyrocatechol (EugOH)

EugOH and its precursor, EugTES, were synthesized following the procedures

described in Sections **2.3.2** and **2.3.3**.

3.3.3 Synthesis of Modified PETMP (Mod-PETMP)

Modified PETMPs were synthesized following a modified literature procedure[23] by statistically adding of one of three acrylates – lauryl acrylate, poly(ethylene glycol) acrylate (PEG, MW ~375), and 2-(perfluorohexyl)ethyl acrylate (F6) – to PETMP. The general synthetic procedure is as follows: PETMP (10.0 g) and 1,8-diazabicyclo(5.4.0)undec-7-ene (DBU, 1 mol % relative to PETMP) were dissolved in 60 mL of acetone at room temperature. An acrylate (in a 1:1 mol ratio with PETMP) was dissolved in 30 mL of acetone and added dropwise, slowly, to the PETMP solution. Reactions proceeded overnight followed by the removal of solvent under rotary evaporation and vacuum. No additional purification was conducted. See Appendix C – Figures C1 – C3 for ^{1}H NMR product spectrum.

3.3.4 Network Preparation

Based on the results from Chapter II, all network formulations contained 35 mol % EugOH to ensure adhesive behavior without detrimental decreases in network properties. Ternary networks were synthesized containing pentaerythritol triallyl ether (APE) and EugOH in a 65:35 mol % alkene ratio. TMPMP and Mod-PETMP were subsequently added in a 100:0, 75:25, 50:50, and 0:100 TMPMP:Mod-PETMP mol ratio, maintaining a 1:1 SH:alkene mol ratio. All formulations contained 5 wt.% Darocur 1173 and were polymerized under a broadband mercury UV light at an intensity of 25 mW/cm^2 for 30 minutes into various molds.

3.3.5 Adhesion Testing

Quantitative adhesion was measured via a single-lap joint adhesively bonded glass sample according to a modified version of ASTM D-1002.[24] Underwater adhesion

was tested under two conditions, designated as "strict" and "moderate". Under the strict

condition, all glass substrates were subjected to plasma treatment for 5 minutes prior to

adhesive application. Plasma cleaning results in glass substrates that are

superhydrophilic and are expected to have an increased affinity for water. Further, under

strict conditions, the entirety of the photopolymerization is conducted while the lap shear

sample is submerged in a deionized (DI) water bath. Under moderate conditions, no

plasma cleaning is conducted and photopolymerizations are conducted in air. In both

cases, (strict and moderate) glass substrates are soaked in deionized water for 30 minutes

followed by direct application of the various adhesive resins (8 µL) to the wet substrate

surface. Samples are then overlapped (1.2 cm x 2.5 cm), clamped, and exposed to 25

mW/cm^2 UV light for 15 minutes, before the clamps are removed and the samples are

subjected to an additional 15 minutes of UV exposure. Cured samples were then

trimmed to ensure that all adhesive forces originate from the overlapped region, and lap

shear testing was performed using an MTS Insight material testing machine equipped

with a 500 N load cell, moving with a crosshead speed of 0.5cm/min. At least five trails

were performed per sample to obtain a statistical average

3.3.6 Characterization

A Varian Mercury Plus 300 MHz NMR spectrometer operating at a frequency of

300.13 MHz with VNMR 6.1C software was used for structural analysis of EugTES,

EugOH, and the Mod-PETMPs. Kinetic data was obtained using real time FTIR (RT-

FTIR) spectroscopy by determining the conversion of the thiol functional group. The RT-

FTIR studies were conducted using a Nicolet 8700 spectrometer with a KBr beam splitter

and a MCT/A detector with a 320−500 nm filtered ultraviolet light source. Each sample

was sandwiched between two NaCl plates and exposed to a UV light with an intensity of approximately 25 mW/cm^2. A series of scans were recorded, where spectra were taken approximately 3 scan/s with a resolution of 4 cm^{-1}. Dynamic mechanical analysis (DMA) was performed using a TA Instruments Q800 dynamic mechanical analyzer in tension film mode equipped with a gas cooling accessory. Samples were secured and the strain applied was 0.05%. Samples were heated from −40 to 60 °C at a ramp rate of 2 °C/min. Static water contact angle measurements were performed using a Rame-Hart 200-00 Std.-Tilting B. goniometer. Static angles were measured using a 6 µL drop and the average of three measurements is reported.

3.4 Results and Discussion

3.4.1 Synthesis of Modified PETMP (Mod-PETMP)
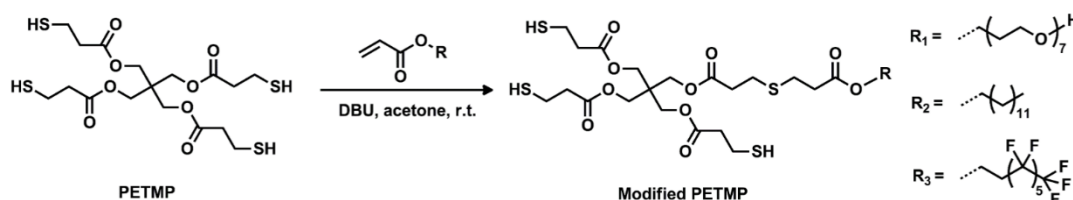
Figure 3.1 Synthesis of modified PETMPs via a thiol-Michael reaction. Modified PETMPs are designated as follows: R$_1$ = PEG-PETMP, R$_2$ = Lauryl-PETMP, R$_3$ = F6-PETMP.

In order to elucidate the influence of a hydrophobic pendant chain incorporated into a catechol-based adhesive network, a series of modified PETMPs were synthesized via thiol-Michael addition according to Figure 3.1. The acrylates were incorporated in a 1:1 PETMP:acrylate mol ratio to statistically modify PETMP, and were chosen to impart a range of wetting behavior to the resulting polymer networks (PEG-PETMP targets hydrophilic networks, lauryl-PETMP targets slightly hydrophobic networks, and F6-PETMP targets hydrophobic networks). Reaction conversion was monitored via ^{1}H

NMR and reaction completion was confirmed upon complete consumption of the acrylate functional group. Product ^{1}H NMR spectra confirm the approximate mono-addition of the varying acrylates (Appendix C – Figures C1-C3), and the described technique demonstrates the ease and versatility with which thiol monomers may be modified with additional functional groups.

3.4.2 Adhesive Thiol-Ene Network Preparation and Characterization
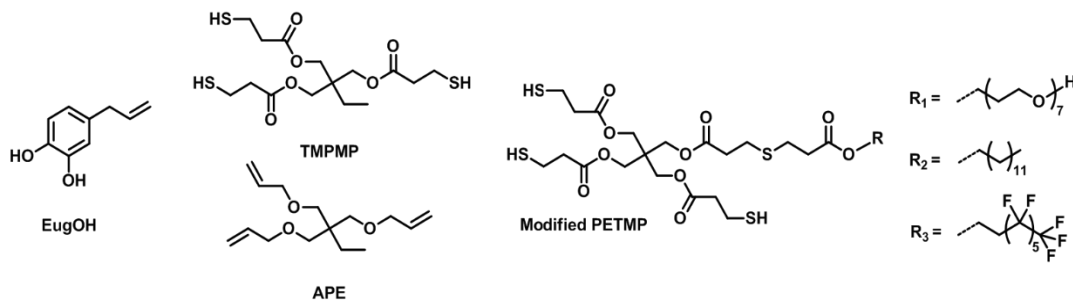
Figure 3.2 Thiol-ene monomers used to prepare adhesive networks of varying hydrophobicity.

Thiol-ene polymer networks were prepared utilizing the monomers shown in Figure 3.2. All formulations contained a 65:35 APE:EugOH mol alkene ratio in order to impart catechol-based adhesive behavior, while avoiding significant catechol-induced inhibition effects.[13] TMPMP and the Mod-PETMPs mol ratios were varied from 100:0, 75:25, 50:50, and 0:100 TMPMP:Mod-PETMP in order to selectively alter the wetting behavior of the polymer networks without altering the crosslink density, allowing the direct study of pendant chain influence on adhesive and network properties. All monomer formulations were homogeneous following mixing with the exception of the 25 mol % F6-PETMP which required small amounts of heat to solubilize (~35 °C).

Due to the step-growth nature of a thiol-ene polymerization, high conversion values are necessary to achieve appreciable network formation and properties. Therefore,

the influence of both the catechol and the pendant chains on photopolymerization kinetics

were studied via real-time FTIR (RT-FTIR), by monitoring the change in area of the thiol

peak (2570 cm^{-1}) over 10 minutes. Due to spectral overlap between the alkene and
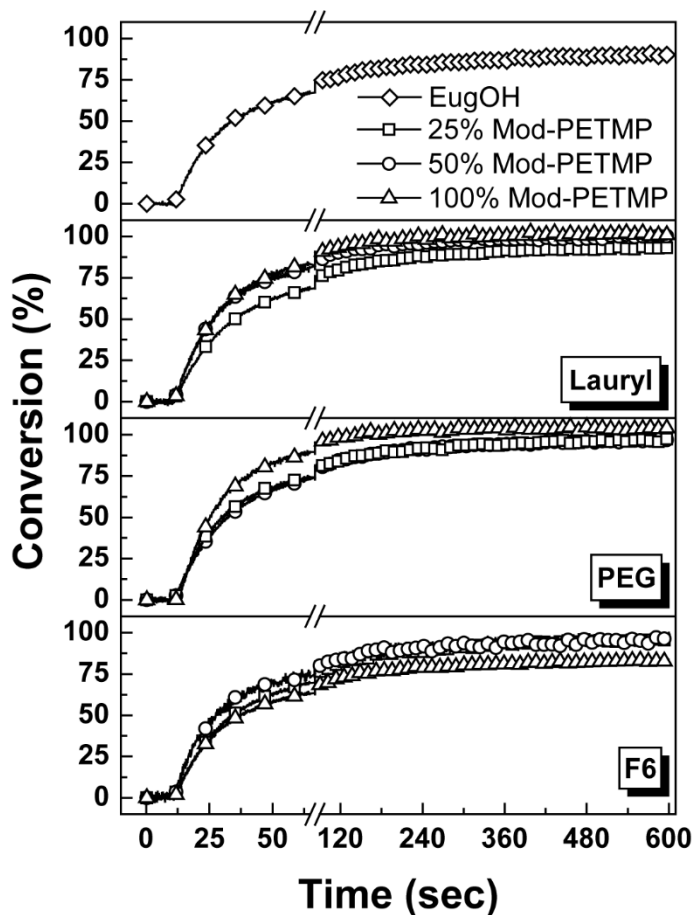
Figure 3.3 RT-FTIR conversion plots of catechol-based thiol-ene adhesive networks synthesized containing varying mol % of Mod-PETMPs. EugOH designates a control polymer network containing no Mod-PETMP.

hydroxyl peaks, the alkene kinetics were not monitored. The results are shown in Figure

3.3 and summarized in Table 3.1. In the absence of any pendant chains, network

conversion reaches 91% (EugOH control network). The lack of quantitative conversion

is a likely result of catechol-induced inhibition and retardation. As demonstrated in

Chapter II, the incorporation of 35 mol % EugOH resulted in an 86% conversion for a

EugOH-APE-PETMP network (Figure 2.3).[13] The increased conversion observed in the

EugOH curve of Figure 3.3 is a result of both increased photoinitiator concentration and

Table 3.1

Network Conversion Values for Photopolymerized Mod-PETMP Networks

| Network | mol % Mod-PETMP | | | |
Comp.	0	25	50	100
EugOH	91%	-	-	-
Lauryl-PETMP	-	93%	99%	>99%
PEG-PETMP	-	97%	97%	>99%
F6-PETMP	-	96%	96%	83%

reaction times. Interestingly, for all Mod-PETMP networks (with the exception of 100%

F6-PETMP) an increase in final conversion is observed with increasing Mod-PETMP

concentration. The decreased conversion observed in the 100% F6-PETMP (83%) is a

suspected result of polymerization induced phase separation. Considering the three

pendant chains are dissimilar in chemical structure (alkyl, ethylene glycol,

perfluoroalkyl), the increased conversion is not readily explainable. Autoaccelartion and

increased polymerization conversions have been observed in the network polymerizations

of acrylates due to the Trommsdorff effect, however, this mechanism has been theorized

and experimentally proven for chain growth polymerizations[25, 26], and to the best of our

knowledge has never been reported for a purely step-growth radical reaction. Further

complicating matters is the inhibition and retardation caused by the catechol moiety.

Although a definitive conclusion cannot be drawn, the increased conversions as a

function of Mod-PETMP concentration at a constant catechol concentration is ultimately

beneficial to network preparation and may provide a route towards mitigating or

competing with the catechol-based inhibition.

Mod-PETMP networks were next subjected to thermomechanical testing to

determine the influence of the varying pendant chains on T_g and crosslink density.
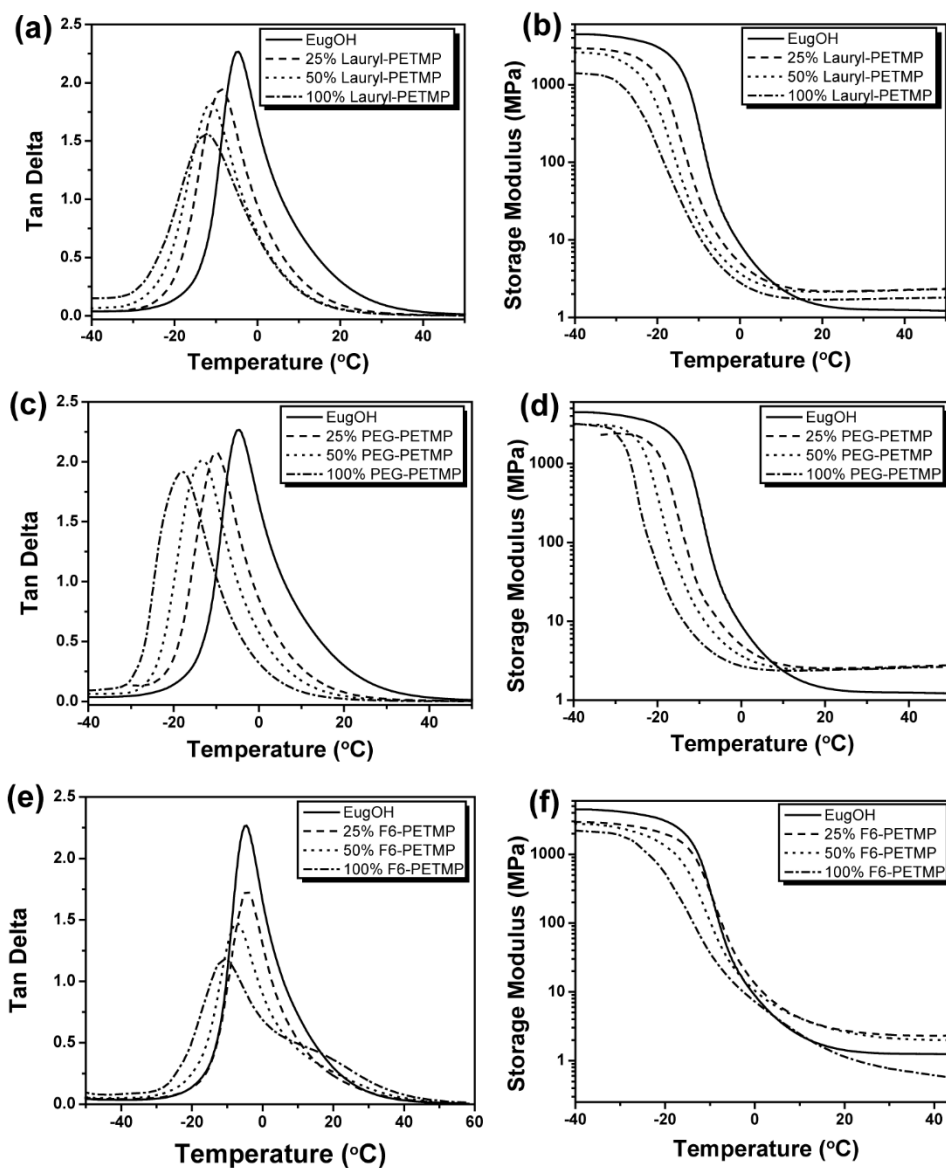
Figure 3.4 Dynamic mechanical analysis plots for Mod-PETMP networks. (a) Tan δ and (b) storage modulus curves of Lauryl-PETMP networks (c) Tan δ and (d) storage modulus curves of PEG-PETMP networks (e) Tan δ and (f) storage modulus curves of F6-PETMP.

Table 3.2

Thermomechanical Properties of Mod-PETMP Thiol-ene Networks

mol % Mod-PETMP.	T_g (°C)	fwhm (°C)[a]	ρ_x (10^{-3}mol cm^{-3})[b]
EugOH	-4.58	14.0	0.163
Lauryl-PETMP			
25%	-8.74	14.9	0.291
50%	-11.4	15.1	0.287
100%	-12.4	18.0	0.229
PEG-PETMP			
25%	-10.0	13.2	0.342
50%	-13.2	14.4	0.333
100%	-17.8	14.9	0.329
F6-PETMP			
25%	-4.49	14.2	0.302
50%	-7.29	15.5	0.272
100%	-10.8	20.5	0.105

a fwhm obtained from the tan δ curves bcrosslink density (ρx)

Films were prepared according to section **2.3.4** and analyzed via dynamic mechanical

analysis (strain film mode, heating rate 2.0 °C/min). Results are shown in Figure 3.4 and

summarized in Table 3.2. From the tan δ curves of Figure 3.4 (a), (c), and (e), it is clear

that the incorporation of a long, pendant chain, regardless of chemical composition,

results in a decrease in the T_g at all concentrations of Mod- PETMP relative to the

EugOH control (T_g = -4.58 °C). The largest decreases in T_g are observed for the PEG-

PETMP system, with T_g's decreasing to -10.0 °C, -13.2 °C, and -17.8 °C for 25, 50, and

100 mol % PEG-PETMP, respectively. Decreased T_g as function of pendant chain

concentration has been well-characterized and is due to internal plasticization and

disruption of chain packing caused by the presence of pendant chains.[27] The increased

magnitude in T_g change for the PEG-PETMP system relative to the Lauryl and F6

systems is due to the increased length of the PEG repeat unit, and therefore increased

length of the total pendant chain.[28-30] Additionally, the increased incorporation of the

Mod-PETMPs caused a slight increase in the full-width at half max (fwhm) of the tan δ curves, indicating small increases in network homogeneity. The tan δ curve of the 100% F6-PETMP (Figure 3.4(e)), however, shows a bimodal distribution indicative of significant network heterogeneity likely caused by the high concentrations and aggregation of non-polar perfluoroalkyl chains.[31] Ultimately, however, all networks (excluding 100 mol % F6-PETMP) show fwhm values similar to those previously reported for catechol-based thiol-ene networks, indicating a well-defined network structure.[13]

The crosslink density (determined from the rubbery plateau region of the storage modulus curves shown in Figure 3.4 (b), (e), and (f)), conversely, increased for all Mod-PETMP networks relative to the EugOH control, excluding the 100% F6-PETMP. Crosslink densities increased from $0.163 \cdot 10^{-3}$ mol cm^{-3} for EugOH to 0.291, 0.342, and $0.302 \cdot 10^{-3}$ mol cm^{-3} for 25 mol % Lauryl-PETMP, 25 mol% PEG-PETMP, and 25 mol % F6-PETMP, respectively. Typically, one may expect the crosslink density to decrease with T_g, however, the increased conversion of the Mod-PETMP networks relative to the EugOH control results in an increased crosslink density. As the thiol-ene networks are formed via a step-growth reaction, even slight increases in final network conversion would lead to significant increases in the degree of polymerization.[32] This effect is observed in the 25 mol % PEG-PETMP network, which has the lowest T_g of all 25 mol % Mod-PETMP networks but has the highest network conversion, and therefore highest crosslink density. Within a Mod-PETMP series, however, the crosslink density decreases with increasing Mod-PETMP concentration owing to the increased free volume within the polymer network with increasing pendant chain concentration.[29, 30] The low
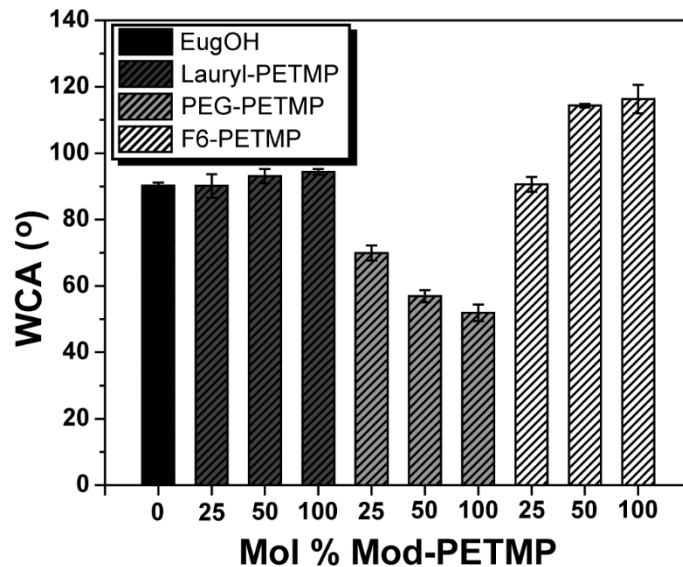
Figure 3.5 Water contact angles measured for Lauryl-, PEG-, and F6-PETMP thiol-ene adhesive networks.

crosslink density observed for 100 mol %F6-PETMP network ($0.105 \cdot 10^{-3}$ mol cm^{-3}) is again likely caused by an increase in network heterogeneity due to the aggregation of perfluoroalkyl chains.

To probe pendant chain influence on network hydrophobicity, static water contact angle measurements were conducted on Mod-PETMP networks. Samples were prepared such that one side of the polymerization mold remained open to atmosphere. The results are presented in Figure 3.5. Lauryl chains showed little to no change in network hydrophobicity, with water contact angles increasing from 90.2°±0.9° (EugOH) to 90.1°±3.5°, 93.1°±2.2°, and 94.4°±0.8° for 25, 50, and 100 mol % Lauryl-PETMP networks, respectively. As relatively minimal changes in water contact angle were observed, the Lauryl-PETMP networks will facilitate an understanding of how changes in thermomechanical properties influence dry and underwater adhesion. Incorporation of PEG chains resulted in decreases in water contact angle with values of 69.9°±2.3°,

56.9°±1.8°, and 51.9°±2.5° measured for a 25, 50, and 100 mol % PEG-PETMP

networks, respectively. The study of hydrophilic networks serves as an additional control

to help deconvolute the role of water and network wettability on adhesion strength.

Conversely, the inclusion of perfluoroalkyl chains resulted in increases in water contact

angle to 90.6°±2.4°, 114.3°±0.5°, and 116.3°±4.3° for 25, 50, and 100 mol % F6-PETMP

networks, respectively (the minimal increased observed for the 100 mol% F6-PETMP

sample is likely due to the saturation of the film interface with perfluoroalkyl chains[33]).

F6-PETMP networks will be used to test the hypothesis that the inclusion of hydrophobic

groups will improve underwater adhesion by forcing water from the adhesive/substrate

interface.

3.4.3 Underwater Adhesion Testing

To investigate pendant chain influence on underwater adhesion, lap shear

adhesion testing was carried out according to a modified procedure outlined by ASTM D-

1002.[24] Since the thiol-ene adhesive networks are synthesized via photopolymerization,

adhesion testing was limited to glass substrates. As described in section 3.3.5,

underwater/wet adhesion was tested under two conditions, designated as "strict" and

"moderate" (see Appendix C – Figure C4). Briefly, strict conditions utilize plasma

treated glass slides, and lap shear samples are prepared entirely underwater. Plasma

treatment results in superhydrophilic glass slides that are expected to have an increased

affinity for water during sample preparation. Moderate conditions do not use plasma

treated glass, and thus the substrates are not superhydrophilic. Further, polymerizations

are conducted in atmosphere (not underwater), resulting in a milder wet condition. Under

both conditions, slides were soaked in DI H_2O prior to adhesive application, and all
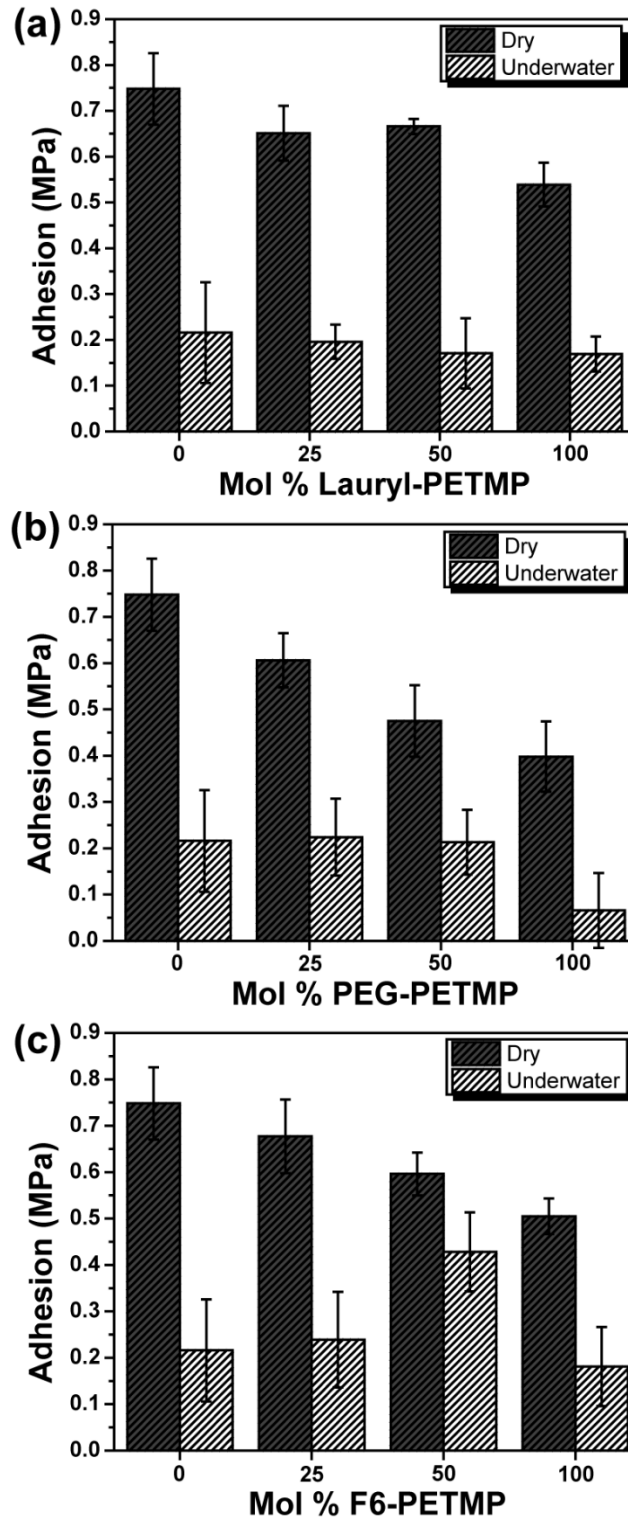
Figure 3.6 Lap shear adhesion testing under dry and strict underwater conditions for (a) Lauryl-PETMP networks (b) PEG-PETMP networks (c) F6-PETMP networks.

Table 3.3

Adhesion Strength of Mod-PETMP Networks Under Strict Conditions

mol % Mod-PETMP	Dry (MPa)	Underwater (MPa)
EugOH	0.748±0.078	0.216±0.110
Lauryl-PETMP		
25	0.651±0.060	0.196±0.037
50	0.666±0.017	0.171±0.076
100	0.539±0.048	0.169±0.038
PEG-PETMP		
25	0.606±0.058	0.224±0.083
50	0.475±0.077	0.214±0.070
100	0.398±0.076	0.0657±0.081
F6-PETMP		
25	0.677±0.079	0.239±0.103
50	0.596±0.046	0.428±0.085
100	0.505±0.039	0.181±0.085

samples were prepared without substrate drying. Lap shear adhesion results for strict

conditions are shown in Figure 3.6 and summarized in Table 3.3. As shown, the presence

of lauryl chains has minimal effect on both dry and underwater adhesion. A small

decrease in adhesive strength was observed under dry conditions, with adhesive strength

shifting from 0.748±0.078 MPa for the EugOH control network (0% Mod-PETMP) to

0.539±0.048 MPa for the 100 mol % Lauryl-PETMP network, while no change, within

error, was observed in underwater adhesion strength. It is worth noting that samples

characterized by an adhesive strength of approximately ≤0.200 MPa are extremely weak

and may fracture under handling pressures. The minimal changes in adhesion strength

observed for the Lauryl-PETMP samples suggest that the slight changes observed in

thermomechanical properties for the Mod-PETMP networks have minimal influence on

the dry and wet adhesion values. PEG-PETMP networks exhibited the most striking

decreases in dry adhesive strength, with values decreasing to 0.475±0.077 MPa and

0.398±0.076 MPa for 50 and 100 mol % PEG-PETMP networks, respectively. The weak

adhesion observed for the dry PEG-PETMP networks is likely due to the increased water

content absorbed into the polymer network from atmosphere due to the hydrogen bonding

capabilities of PEG chains.[34, 35] Under water, the 25 and 50 mol % PEG-PETMP

networks showed similar adhesive strength compared to the EugOH control, while the

100 mol % PEG-PETMP networks showed drastic decreases in underwater adhesion

strength, further exemplifying the detrimental influence of water on adhesion. F6-

PETMP networks showed similar decreases in dry adhesion, with adhesion strengths of

0.677±0.079, 0.596±0.046 and 0.505±0.039 for 25, 50, and 100 mol % F6-PETMP

networks, respectively. The decrease in dry adhesive strength for the semi-fluorinated

networks is expected, as perfluoroalkyl chains are known to be non-adhesive.[36, 37] Under

water, no improvement in adhesion is observed for the 25 mol % F6-PETMP network.

The 50 mol % F6-PETMP network, however, showed an increase in underwater adhesion

strength to 0.428±0.085 MPa relative to the EugOH control (0.216±0.110 MPa).

Considering the similar thermomechanical properties observed for all Mod-PETMP

networks, and the lack of improved underwater adhesion in the Lauryl- and PEG-PETMP

networks, the improvement in underwater adhesion observed for the F6-PETMP samples

is likely a function of the increased network hydrophobicity. It is suspected, that upon

application of the hydrophobic resin to the wet substrate surface, bulk water is pushed

away from both the substrate surface and the adhesive resin, allowing a more intimate

and uniform contact between the substrate and adhesive. Further, as the lap shear sample

is prepared and the two glass substrates are pushed together, the flow and spread of the

hydrophobic adhesive resin forces additional water from the overlap area. The removal

of water (confirmed visually on the macroscopic scale, only) would allow 1) a more

uniform and complete adhesive coating to be generated in the overlap region, and 2)

would facilitate the binding of the catechol group to the substrate surface. A combination

of these factors would lead to the observed increase in underwater adhesion strength.

Although the 100 mol % F6-PETMP network showed a similar water contact angle to the

50 mol % F6-PETMP network, the increased network heterogeneity in the 100 mol %

F6-PETMP sample limits its adhesive ability under aqueous conditions.
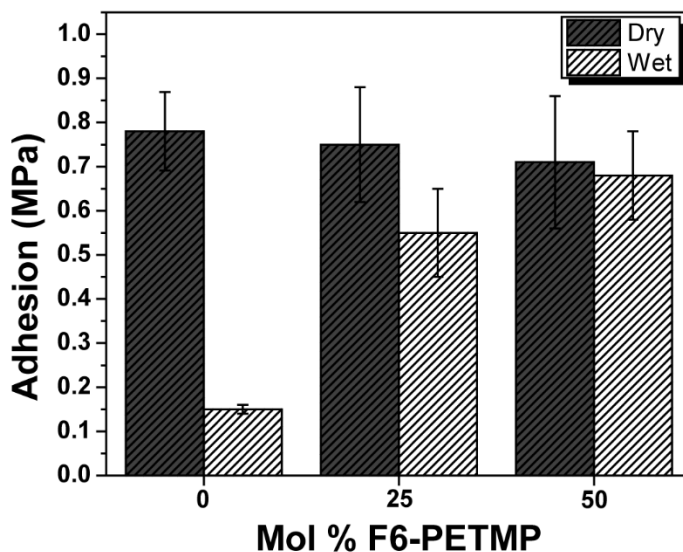
Figure 3.7 Lap shear adhesion testing for F6-PETMP networks under moderate
conditions.

While encouraging, adhesive binding for the F6-PETMP networks remains

challenging under strict conditions. Following polymerization, a de-wetting effect was

commonly observed near the edge of the overlapped region, suggesting water may be

either difficult to completely remove from the overlapped region, or is capable of

diffusing into the edges of the lap shear sample. As such, lap shear samples were

prepared under "moderate" conditions, where substrates were not plasma cleaned and

polymerizations were conducted in air. Without plasma cleaning, glass substrates did not exhibit superhydrophilic wetting and are thus expected to have a decreased affinity for water during sample preparation. Conducting polymerizations in atmosphere further mitigates the influence of water, by preventing any diffusion effects that may occur during the length of the polymerization. Adhesion testing results under moderate conditions are shown in Figure 3.7. From the data shown, a clear increase in wet adhesion strength is observed, with adhesion values increasing from 0.150±0.012 MPa for the EugOH control to 0.551±0.101 MPa for the 25 mol % F6-PETMP network and 0.682±0.099 MPa for the 50 mol % F6-PETMP network (100 mol % F6-PETMP samples were not prepared due to the observed phase separation behavior). Although the wet conditions tested in Figure 3.7 are not as rigorous as those observed in the strict, underwater condition, the presence of water on the glass substrates alone leads to catastrophic decreases in adhesion for the EugOH network. Utilizing a hydrophobic adhesive, however, leads to increased wet adhesive strength, with a complete recovery of adhesion strength (relative to the dry condition) being observed for the 50 mol % F6-PETMP network. While adhesive binding under submerged conditions remains challenging, binding under milder, wet conditions, may be facilitated by the presence of a hydrophobic adhesive.

3.5 Conclusions

In summary, we have demonstrated that the incorporation of a hydrophobic pendant chain, specifically, a perfluoroalkyl chain leads to improvements in underwater/wet adhesion on glass substrates for a catechol-based thiol-ene network. The inclusion of a pendant chain caused a decrease in network T_g, though serendipitously,

resulted in improved polymerization conversions, mitigating the radical inhibition and retardation effects observed in catechol-based materials. By comparison to a series of controls, improved underwater and wet adhesion strength for a semi-fluorinated, catechol-based thiol-ene network was rationalized by an increased network hydrophobicity and removal of bulk water from the substrate and resin interface. The results are moderately surprising as perfluoroalkyl chains are commonly considered non-adhesive. However, adhesion results revealed a synergy between interacting (catechol) and non-interacting (perfluoroalkyl) components of an adhesive resin, and suggests that underwater adhesion may be improved by incorporation of hydrophobic chemistries into biomimetic, synthetic aqueous adhesives. Though the polymers developed in this Chapter are a model system, this works demonstrates a mild synthetic pathway to the generation of light-responsive, bio-inspired adhesives with improved adhesion in aqueous environments that may facilitate the development of adhesives for more advanced dental or biomedical applications.

3.6 References

(1). Petrie, E. M. Environment, Production, Applications. In *Handbook of Adhesives and Sealants*, 2 ed.; McGraw-Hill: New York, New York, 2007.

(2). Schneberger, G. L. Polymer Structure and Adhesive Behavior. In *Adhesives and Manufacturing*, Marcel Dekker: New York, New York, 1983.

(3). Waite, J. H.; Andersen, N. H.; Jewhurst, S.; Sun, C. Mussel Adhesion: Finding the Tricks Worth Mimicking *J. Adhesion* **2005,** *81*, 297-317.

(4). Waite, J. H. Nature's Underwater Adhesive Specialist *Int. J. Adhes. Adhes.* **1987,** *7*, 9-14.

(5). Stewart, R. J.; Wang, C. S.; Shao, H. Complex Coacervates as a Foundation for Synthetic Underwater Adhesives *Adv. Colloid Interface Sci.* **2011,** *167*, 85-93.

(6). Kamino, K. Mini-Review: Barnacle Adhesives and Adhesion *Biofouling* **2013,** *29*, 735-749.

(7). Khandeparker, L.; Anil, A. C. Underwater Adhesion: The Barnacle Way *Int. J. Adhes. Adhes.* **2007,** *27*, 165-172.

(8). Waite, J. H.; Tanzer, M. L. Polyphenolic Substance of Mytilus Edulis: Novel Adhesive Containing L-Dopa and Hydroxyproline *Science* **1981,** *212*, 1038-1040.

(9). Lee, P. B.; Messersmith, P. B.; Israelachvili, J. N.; Waite, J. H. Mussel-Inspired Adhesives and Coatings *Annu. Rev. Mater. Res.* **2011,** *41*, 99-132.

(10). Li, Y.; Qin, M.; Li, Y.; Cao, Y.; Wang, W. Single Molecule Evidence for the Adaptive Binding of Dopa to Different Wet Surfaces *Langmuir* **2014,** *30*, 4358-4366.

(11). Sedó, J.; Saiz-Poseu, J.; Busqué, F.; Ruiz-Molina, D. Catechol-Based Biomimetic Functional Materials *Adv. Mater.* **2013,** *25*, 653-701.

(12). Mian, S. A.; Yang, L.-M.; Saha, L. C.; Ahmed, E.; Ajmal, M.; Ganz, E. A Fundamental Understanding of Catechol and Water Adsorption on a Hydrophilic Silica Surface: Exploring the Underwater Adhesion Mechanism of Mussels on an Atomic Scale *Langmuir* **2014,** *30*, 6906-6914.

(13). Donovan, B. R.; Cobb, J. S.; Hoff, E. F. T.; Patton, D. L. Thiol-Ene Adhesives from Clove Oil Derivatives *RSC Advances* **2014,** *4*, 61927-61935.

(14). Wilker, J. J. Biomaterials: Redox and Adhesion on the Rocks *Nat. Chem. Biol.* **2011,** *7*, 579-580.

(15). Bandara, N.; Zeng, H.; Wu, J. Marine Mussel Adhesion: Biochemistry, Mechanisms, and Biomimetics *J. Adhes. Sci. Technol.* **2013,** *27*, 2139-2162.

(16). Maier, G. P.; Rapp, M. V.; Waite, J. H.; Israelachvili, J. N.; Butler, A. Adaptive Synergy between Catechol and Lysine Promotes Wet Adhesion by Surface Salt Displacement *Science* **2015,** *349*, 628-632.

(17). Akdogan, Y.; Wei, W.; Huang, K.-Y.; Kageyama, Y.; Danner, E. W.; Miller, D. R.; Martinez Rodriguez, N. R.; Waite, J. H.; Han, S. Intrinsic Surface-Drying Properties of Bioadhesive Proteins *Angew. Chem. Int. Ed.* **2014,** *53*, 11253-11256.

(18). Seo, S.; Das, S.; Zalicki, P. J.; Mirshafian, R.; Eisenbach, C. D.; Israelachvili, J. N.; Waite, J. H.; Ahn, B. K. Microphase Behavior and Enhanced Wet-Cohesion of Synthetic Copolyampholytes Inspired by a Mussel Foot Protein *J. Am. Chem. Soc.* **2015,** *137*, 9214-9217.

(19). Shao, H.; Stewart, R. J. Biomimetic Underwater Adhesives with Environmentally Triggered Setting Mechanisms *Adv. Mater.* **2010,** *22*, 729-733.

(20). White, J. D.; Wilker, J. J. Underwater Bonding with Charged Polymer Mimics of Marine Mussel Adhesive Proteins *Macromolecules* **2011,** *44*, 5085-5088.

(21). Stewart, R. J. Protein-Based Underwater Adhesives and the Prospects for Their Biotechnological Production *J. Appl. Microbiol. Biotechnol.* **2011,** *89*, 27-33.

(22). Wei, W.; Yu, J.; Broomell, C.; Israelachvili, J. N.; Waite, J. H. Hydrophobic Enhancement of Dopa-Mediated Adhesion in a Mussel Foot Protein *J. Am. Chem. Soc.* **2013,** *135*, 377-383.

(23). Kwisnek, L.; Nazarenko, S.; Hoyle, C. E. Oxygen Transport Properties of Thiol−Ene Networks *Macromolecules* **2009,** *42*, 7031-7041.

(24). Astm D1002-10 Apparent Shear Strength of Single-Lap-Join Adhesively Bonded Metal Specimens by Tension Loading (Metal-to-Metal). ASTM Internationl: West Conshohocken, PA, 2010.

(25). Dvornić, P. R.; Jaćović, M. S. The Viscosity Effect on Autoacceleration of the Rate of Free Radical Polymerization *Polym. Eng. Sci.* **1981,** *21*, 792-796.

(26). O'Shaughnessy, B.; Yu, J. Autoacceleration in Free Radical Polymerization *Phys. Rev. Lett.* **1994,** *73*, 1723-1726.

(27). Immergut, E. H.; Mark, H. F. Principles of Plasticization. In *Plasticization and Plasticizer Processes*, ACS: 1965, Vol. 48, 1-26.

(28). Reimschuessel, H. K. On the Glass Transition Temperature of Comblike Polymers: Effects of Side Chain Length and Backbone Chain Structure *J. Polym. Sci. Chem. Ed.* **1979,** *17*, 2447-2457.

(29). Stutz, H.; Illers, K. H.; Mertes, J. A Generalized Theory for the Glass Transition Temperature of Crosslinked and Uncrosslinked Polymers *J. Polym. Sci. B: Polym. Phys.* **1990,** *28*, 1483-1498.

(30). Kwisnek, L.; Kaushik, M.; Hoyle, C. E.; Nazarenko, S. Free Volume, Transport, and Physical Properties of N-Alkyl Derivatized Thiol−Ene Networks: Chain Length Effect *Macromolecules* **2010,** *43*, 3859-3867.

(31). Vitale, A.; Bongiovanni, R.; Ameduri, B. Fluorinated Oligomers and Polymers in Photopolymerization *Chem. Rev.* **2015,** *115*, 8835-8866.

(32). Odian, G. Step Polymerization. In *Principles of Polymerization*, John Wiley & Sons, Inc.: 2004, 39-197.

(33). Xiong, L.; Kendrick, L. L.; Heusser, H.; Webb, J. C.; Sparks, B. J.; Goetz, J. T.; Guo, W.; Stafford, C. M.; Blanton, M. D.; Nazarenko, S.; Patton, D. L. Spray-Deposition and Photopolymerization of Organic–Inorganic Thiol–Ene Resins for Fabrication of Superamphiphobic Surfaces *ACS Appl. Mater. Interfaces* **2014,** *6*, 10763-10774.

(34). Feng, Z., *Antifouling Surfaces and Materials*. 1 ed.; Springer-Verlag Berlin Heidelberg: Heidelberg, Germany, 2015.

(35). Meredith, H. J.; Wilker, J. J. The Interplay of Modulus, Strength, and Ductility in Adhesive Design Using Biomimetic Polymer Chemistry *Adv. Func. Mater.* **2015,** *25*, 5057-5065.

(36). Anton, D. Surface-Fluorinated Coatings *Adv. Mater.* **1998,** *10*, 1197-1205.

(37). Sianesi, D.; Marchionni, G.; De Pasquale, R.; Banks, R., *Organofluorine Chemistry: Principles and Commercial Applications*. Plenum Press: New York, New York, 1994.

CHAPTER IV – THIOL-TRIFLUOROVINYL ETHER (TFVE) PHOTOPOLYMERIZATION: AN ON-DEMAND SYNTHETIC ROUTE TO SEMI-FLUORINATED POLYMER NETWORKS

4.1 Abstract

We report a first example of thiol-trifluorovinyl ether (thiol-TFVE) photopolymerization as a facile, cure-on-demand synthetic route to semi-fluorinated polymer networks. The thiol-TFVE reaction – which proceeds via anti-Markovnikov addition of a thiyl radial to the TFVE group – was elucidated using model small molecule reactions between phenyl trifluorovinyl ether and thiols with varying reactivity. These model reactions, characterized by ^{19}F NMR, ^{1}H NMR, and FTIR, also provided evidence of an oxygen-induced degradation pathway that may be circumvented by performing the reactions under an inert gas atmosphere. Photopolymerization of difunctional TFVE monomers with multifunctional thiols occurred with rapid kinetics and high conversions as observed with real-time FTIR, and provided homogeneous semi-fluorinated polymer networks with narrow glass transitions as observed with dynamic mechanical analysis. The semi-fluorinated ether/thioether linkage incorporated into the polymer network yielded hydrophobic materials with increased and tunable T_g, a 2-fold increase in strain at break, 4-fold increase in stress at break, and more than 5-fold increase in toughness relative to a thiol-ene material composed of a structurally similar hydrogenated ether/thioether linkage. The increased T_g and mechanical toughness are attributed to the

higher rigidity, hydrogen-bonding capacity, and stronger carbon-carbon bonds of the semi-fluorinated ether/thioether relative to the hydrogenated ether/thioether.

4.2 Introduction

Fluorinated polymers have found prolific use in many high performance applications owing to their mechanical strength, high thermal stability, unique optical and electronic properties, low surface energy, and chemical stability.[1-5] While desirable, fully fluorinated polymers are often limited in their application due to their high crystallinity and difficult processing conditions.   Hence, many contemporary synthetic efforts are focused on synthesizing amorphous semi-fluorinated polymers that exhibit analogous properties to fully fluorinated polymers but with improved processability. Of the reported approaches, the use of the trifluorovinyl ether (TFVE) group to synthesize perfluorocyclobutane polymers has provided an effective route to high-performance semi-fluorinated polymers and polymer networks.[6-9] The TFVE group undergoes a thermally induced [2 + 2] cyclodimerization reaction to form fully amorphous step-growth polymers with improved processability while maintaining the advantageous properties of fluoropolymers. Further, owing to the unique mechanism of TFVE synthesis from phenolic species, a broad library of TFVE-containing monomers can be synthesized under mild conditions with diverse chemical structure.[10, 11] With a host of potential monomers available, the TFVE group provides a unique opportunity to synthesize semi-fluorinated polymers with tunable and distinct macromolecular properties.[6, 12-20] Albeit successful in the design and synthesis of semi-fluorinated polymers, the TFVE cyclodimerization reaction requires high temperatures, long reaction times, and, in some instances, solvent and post-polymerization purification.[7, 8, 15, 16] By

contrast, light-mediated polymerizations offer several advantages over thermal polymerizations including shorter reaction times, solvent free polymerization conditions, lower energy consumption, and both spatial and temporal control over polymerization; however, photopolymerization routes involving TFVE monomers have not been reported. As such, we sought a method to synergistically combine the structural diversity provided by TFVE monomers with the benefits of photopolymerization. In this direction, we were inspired by the early work of Harris and Stacey that reported the efficient addition of the trifluoromethanethiyl radical across a trifluorovinyl methyl ether in the presence of UV irradiation.[21] It is particularly noteworthy that the addition of trifluoromethanethiol proceeded in 15 minutes (compared to hours or days for other fluorinated olefins) and occurred at the difluorinated, or "tail", carbon only (e.g. anti-Markovnikov addition). Subsequent work demonstrated that hydrogen sulfide, in the presence of X-ray or UV irradiation, also undergoes radical addition to a trifluorovinyl methyl ether, and while a 2:1 SH:vinyl ether adduct could be formed, only anti-Markovnikov addition was observed.[22] These results suggest that the TFVE group may be an ideal candidate for photopolymerization, where our interests are specifically the thiol-ene photopolymerization.

Thiol-ene photopolymerizations proceed via a radical step-growth mechanism, where a thiyl radical, formed by hydrogen abstraction from a photoinitiator, adds across a double bond to form a carbon-centered radical. The carbon-centered radical then undergoes an efficient and rapid chain transfer reaction with an additional thiol to generate the thiol-ene product and regenerate the propagating thiyl radical species. The radical step-growth nature of the polymerization mechanism imparts several unique

advantages to the synthesis of polymer networks including rapid polymerization times, high conversions, insensitivity to oxygen, and homogenous network structure characterized by uniform and tailorable thermal and mechanical properties.[23, 24] Few examples of semi-fluorinated thiol-ene materials have been reported in the literature,[25-27] and these examples all employ monomers containing semi-fluorinated pendent groups. Herein, we demonstrate a first example of thiol-trifluorovinyl ether (thiol-TFVE) photopolymerization as a facile, cure-on-demand synthetic route to semi-fluorinated polymer networks. The thiol-TFVE reaction was initially elucidated using model small molecule reactions between phenyl trifluorovinyl ether and thiols with varying reactivity. Photopolymerization of difunctional TFVE monomers with multifunctional thiols was assessed in terms of polymerization kinetics, while the mechanical and thermomechanical properties of the resulting semi-fluorinated networks were systematically characterized as a function of TFVE concentration.

4.3 Experimental

4.3.1 Materials

All reagents and solvents were purchased from Sigma Aldrich and used without additional purification unless otherwise specified. Petroleum ether and dichloromethane were purchased from Fisher Scientific; Irgacure 1173 was purchased from BASF; trimethylolpropane tris(3-mercaptopropionate) was purchased from Bruno Bock; and 1,2-dibromotetrafluoroethane and phenyl trifluorovinyl ether (Ph-TFVE) were purchased from SynQuest. Ph-TFVE was further purified by silica gel chromatography prior to use.

4.3.2 Thiol-TFVE Model Reactions

The following describes a typical thiol-TFVE model procedure: A thiol (methyl 3-mercaptopropionate) (M3MP), 1-propanethiol (PrSH), benzyl mercaptan (BnSH) and phenyl trifluorovinyl ether were combined in a 1:1 SH:TFVE mol ratio in the presence of a small weight percent of photoinitiator (1 – 3 wt.%; Irgacure 1173). The resulting mixture was exposed to 100 mW/cm^2 UV light and monitored by ^{1}H and ^{19}F NMR to determine conversion over time. Reactions conducted in inert atmosphere were subjected to three cycles of freeze-pump-thaw using high purity nitrogen. NMR spectra of purified compounds can be found in the Appendix D (Figures D1-D9). Chemical shifts of M3MP/Ph-TFVE are reported below: ^{1}H NMR (C$_2$D$_6$SO, 600 MHz): δ 7.43-7.31 (2H, Ar-H, t, J = 7.5 Hz), 7.21-7.18 (3H, Ar-H, dd, J = 15.3 Hz, 7.8 Hz), 6.65-6.55 (1H, CHF, d, J = 61.8), 3.64 (3H, CH$_3$, s), 3.16 (2H, CH$_2$, t, J = 6.9 Hz), 2.77 (2H, CH$_2$, t, J = 6.9 Hz), X = residual water (3.33) and residual C$_2$H$_6$SO (2.50); ^{19}F NMR (C$_2$D$_6$SO, ref. CF$_3$C$_6$H$_5$, 565 MHz): δ -90.22- -90.64 (1F, CF$_2$, ddd, J = 224.8 Hz, 11.7 Hz, 2.0 Hz), -92.00- -92.42 (1F, CF$_2$, ddd, J = 225.0 Hz, 14.8 Hz, 5.7 Hz) -138.79- -138.95 (1F, CHF, dt, J = 59.2 Hz, 14.3 Hz), X = CF$_3$C$_6$H$_5$; ^{13}C NMR (C$_2$D$_6$SO, 151 MHz): δ 171.3, 154.5, 130.0, 124.5, 116.8, 51.6, 34.5, 22.6.

4.3.3 Thiol-Alkene Model Reactions

Reactions between benzyl mercaptan and traditional alkene monomers were conducted in a similar fashion as the model reactions: benzyl mercaptan and an alkene monomer (5-norbornene-2-methanol (Norbornene), n-butyl vinyl ether (Vinyl Ether), allyl phenyl ether (Allyl Ether), methyl eugenol (Allyl), phenyl trifluorovinyl ether (TFVE)) were combined in a 1:1 SH:alkene mol ratio along with 1 wt.% Irgacure 1173.

Reaction vessels were subjected to three cycles of freeze-pump-thaw and polymerized under 100 mW/cm^2 UV light for 30 minutes. Conversion was monitored via ^{1}H NMR and integration of the alkene peak.

4.3.4 Synthesis of Bisphenol A Bisallyl Ether (Allyl-BPA)

Bisphenol A (15.00 g, 65.7 mmol) and potassium carbonate (22.7 g, 164.2 mmol) were dissolved in 75 mL of acetone before the addition of allyl bromide (19.88 g, 164.3 mmol). The reaction mixture was stirred overnight, followed by the removal of solvent under reduced pressure. The crude mixture was re-dissolved in 100 mL of CH_2Cl_2 and washed 3x100 mL with Na_2SO_4 solution and 1x100 mL with DI H_2O. The organic phase was separated, dried over $MgSO_4$, and solvent was removed via rotary evaporation. The crude oil was purified over a neutral alumina plug using neat petroleum ether as eluent to provide the product as a colorless oil; Isolated yield = 77%; ^{1}H NMR (CDCl$_3$, 600 MHz): δ 7.14 (4H, Ar-H, d, J = 6.6 Hz), 6.82 (4H, Ar-H, d, J = 6.7 Hz), 6.06 (2H, C$\underline{H}$=CH$_2$, m), 5.35 (4H, CH=C$\underline{H}_2$, dd, J = 80.3 Hz, 13.8 Hz), 4.52 (4H, CH$_2$, s), 1.65 (6H, CH$_3$, s); ^{13}C NMR (CDCl$_3$, 151 MHz): δ 156.2, 143.4, 133.7, 127.9, 117.6, 114.2, 68.9, 41.8, 31.2. Appendix D – D15-D16.

4.3.5 Synthesis of 1,1-Bis[4-(2-bromo-1,1,2,2-tetrafluoroethoxy)]isopropylidene (BrE-BPA)

BrE-BPA was synthesized according to a modified literature procedure.[11] BPA (15.00 g, 65.70 mmol) and Cs$_2$CO$_3$ (53.00 g, 162.6 mmol) were dissolved in 100 mL DMSO under inert atmosphere. The solution was brought to 50 °C and 1,2-dibromotetrafluoroethane (43.60 g, 167.9 mmol) was added slowly to the heated mixture. The reaction was stirred overnight, followed by slow dilution with 100 mL DI H_2O. The

mixture was extracted 5x100 mL with petroleum ether and the collected organic phase was washed 3x200 mL with DI H2O. Following drying with Na_2SO_4, the solution was filtered and concentrated via rotary evaporation. The crude oil was further purified by silica gel chromatography using a 98:2 (v:v) petroleum ether:CH_2Cl_2 eluent. Chromatography returned a colorless oil; Yield = 63%; ^{1}H NMR (CDCl$_3$, 600 MHz): δ 7.26 (4H, Ar-H, d, J = 7.5 Hz), 7.16 (4H, Ar-H, d, J = 6.4 Hz), 1.72 (6H, CH$_3$, s); ^{19}F NMR (CDCl$_3$, ref. CF$_3$C$_6$H$_5$, 565 MHz): δ -68.9 (2F, OCF$_2$CF$_2$Br, t, J = 4.8 Hz), -86.9 (2F, OCF$_2$CF$_2$Br, t, J = 4.7 Hz); ^{13}C NMR (CDCl$_3$, 151 MHz): δ 149.0, 147.0, 128.2, 121.3, 42.75, 31.0. Appendix D – D17-D19.

4.3.6 Synthesis of 1,1-Bis(4-trifluorovinyloxy)phenyl)isopropylidene (TFVE-BPA)

To a reaction flask fixed with a condenser was charged 100 mL of MeCN and 7.94 g (121.4 mmol) of zinc dust. The solution was brought to reflux and BrE-BPA (27.23 g, 46.46 mmol) was added slowly. The reaction was stirred overnight, cooled, and the mixture was vacuum filtered to remove residual zinc, followed by removal of MeCN under reduced pressure. The crude organic phase was dissolved in 50 mL hexanes and filtered a second time to remove addition Zn salts. Hexanes was removed under reduced pressure and the crude oil was purified by silica gel chromatography using 95:5 (v:v) petroleum ether:CH_2Cl_2 as an eluent to afford the pure product as a colorless oil; Isolated Yield = 60%; ^{1}H NMR (CDCl$_3$, 600 MHz): δ 7.26 (4H, Ar-H, d, J = 7.2 Hz), 7.05 (4H, Ar-H, d, J = 6.9 Hz), 1.71 (6H, CH$_3$, s); ^{19}F NMR (CDCl$_3$, ref. CF$_3$C$_6$H$_5$, 565 MHz): δ -121.0 (1F, C$\underline{F}_2$=CF, dd, J = 97.6 Hz, 57.9 Hz), -127.8 (1F, C$\underline{F}_2$=CF, dd, J = 109.7 Hz, 97.6 Hz), -134.6 (1F, CF$_2$=C$\underline{F}$, dd, J = 109.6 Hz, 58.0 Hz); ^{13}C NMR (CDCl$_3$, 151 MHz): δ 153.4, 147.2, 128.4, 115.7, 42.4, 31.0. Appendix D – D20-D22.

4.3.7 Network Preparation

Trimethylolpropane tris(3-mercaptopropionate) (TMPMP) and 1,6-hexanedithiol (HexSH$_2$) were combined in a 25:75 mol % SH ratio, along with 1 wt.% Irgacure 1173. The alkene ratio was varied from 0:100 to 100:0 mol % TFVE-BPA: Allyl-BPA maintaining a 1:1 SH:alkene mol ratio. Formulations were then cast into various molds under air and inert atmosphere and polymerized for 30 minutes under a 365 nm centered UV light at an intensity of 40 mW/cm^2.

4.3.8 Characterization

Structural analysis of synthesized compounds was conducted using a Bruker Ascend^{TM} 600 MHz spectrometer. Polymerization kinetic data was collected by real time FTIR (RT-FTIR) using a Nicolet 8700 spectrometer with a KBr beam splitter and a MCT/A detector. Samples were sandwiched between two NaCl salt plates in an N$_2$ atmosphere and polymerized under 20 mW/cm^2 UV light for 5 minutes. Scans were acquired at a rate of approximately 3 scans/s. Conversions were calculated by measuring the change in area under the thiol, allyl ether, and TFVE peaks. Dynamic mechanical analysis was performed using a TA Instruments Q800 dynamic mechanical analyzer in tension film mode. Samples were heated from -30 °C to 80 °C at a rate of 3 °C/min with a frequency amplitude of 15 μm. Mechanical testing was performed using a MTS Insight material testing machine equipped with a 2.5kN load cell. Dog bone samples were synthesized with approximate dimensions of 1.60 mm x 5.00 mm, and a gauge length of 16.70 mm. Materials were deformed at a constant rate of 50 mm/min. Stress and strain at break were determined directly from the tensile test. Toughness was calculated by determining the area under the curve using the Integrate function in Origin 8.6 software,

based on an average of at minimum three samples.   Static water contact angle

measurements were performed using a Rame-Hart 200-00 Std.-Tilting B. goniometer.

Static angles were measured using a 6 μL drop and the average of three measurements is

reported. Thermogravimetric analysis was conducted using a TA Instruments Q50

thermogravimetric analyzer with a platinum pan. Samples were equilibrated at 30.00 °C

before ramping 10.00 °C/min to 800.00 °C under a nitrogen atmosphere with a flow rate

of 10 mg/mL.

4.4 Results and Discussion

4.4.1 Model Thiol-TFVE Reactions
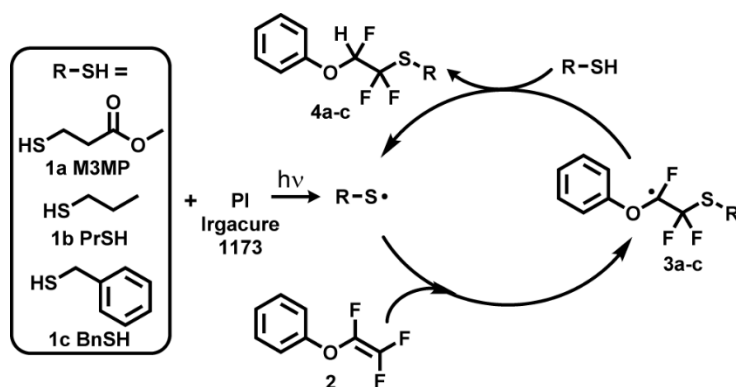
Figure 4.1 Model reaction between Ph-TFVE and a series of thiol monomers with
increasing reactivity in the order M3MP > PrSH > BnSH.

The thiol-TFVE reaction was initially investigated using model reactions between

phenyl trifluorovinyl ether (Ph-TFVE) and a series of thiols of increasing reactivity

(methyl 3-mercaptopropionate [M3MP] > 1-propanethiol [PrSH] > benzyl mercaptan

[BnSH]),[23] as shown in Figure 4.1. TFVE, thiol, and photoinitiator were combined

without solvent and exposed to UV light (100 mW/cm^2) in air. The structure of the thiol-

TFVE adduct was characterized using ^{1}H and ^{19}F NMR. Figure 4.2 shows the ^{1}H and ^{19}F

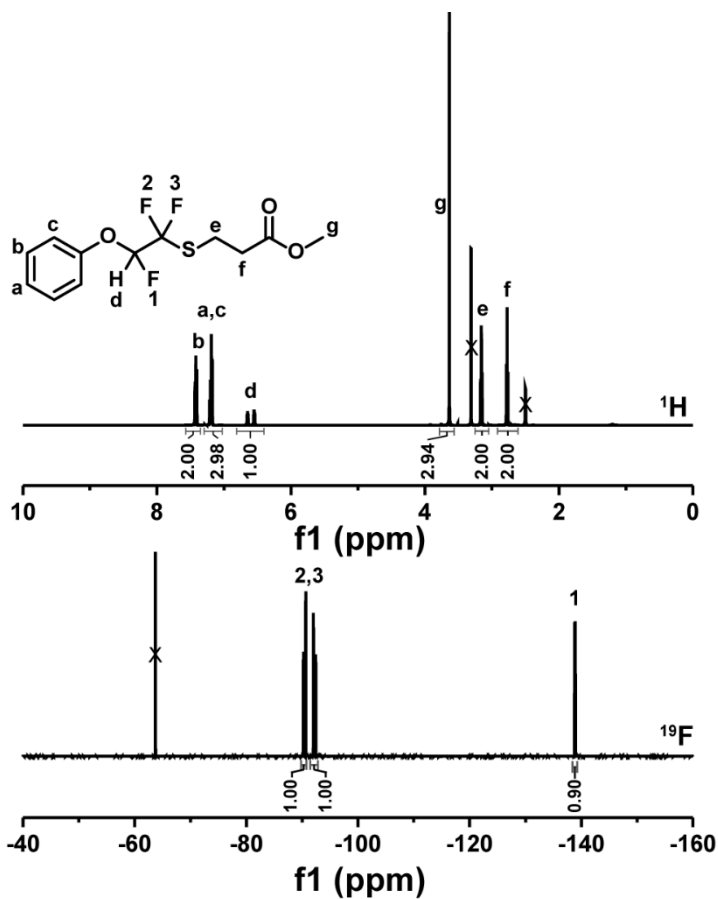NMR spectra for the M3MP/Ph-TFVE adduct (see Appendix D – D1-D9 for NMR of

Figure 4.2 ^{1}H NMR (top) and ^{19}F NMR (bottom) of M3MP/Ph-TFVE addition adduct.

other adducts). In each reaction, the thiol successfully added across the TFVE functional

group to afford a semi-fluorinated ether/thioether linkage. Control experiments

conducted with M3MP/Ph-TFVE in the absence of photoinitiator and UV light revealed

no reaction after 5 days (Appendix D – D10) suggesting the thiol addition does not

proceed through charge transfer or co-oxidation reactions.[28] The appearance of a single

proton peak, **d**, centered around 6.50 ppm represents the hydrogen on the carbon alpha to

the ether linkage, previously a part of the thiol functional group. Additionally, ^{19}F NMR

reveals the disappearance of the TFVE group and the formation of two doublets of

doublets of doublets (ddd) and a doublet of triplets (dt), representing fluorines **1** and **2**,

and **3**, respectively. The anti-Markovnikov addition product was confirmed by the close

inspection of the fluorine peak splitting patterns. The ddd peaks have splitting patterns

with J values of approximately 225 Hz, 13 Hz, and 3 Hz corresponding to geminal F-F

splitting, vicinal F-F splitting, and vicinal H-F splitting, respectively (Appendix D –

D11). The dt peak has splitting patterns with J values of approximately 59 Hz and 14 Hz

corresponding to geminal H-F splitting, and vicinal F-F splitting, respectively. The

splitting patterns and associated integration values confirm the anti-Markovnikov

addition of thiols to the TFVE.
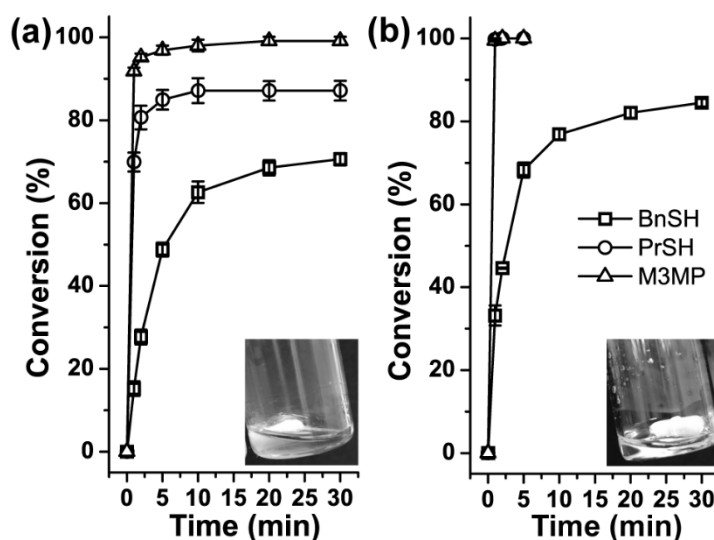
Figure 4.3 TFVE conversion kinetics for thiol/Ph-TFVE reactions conducted at 1 wt.%
photoinitiator and 100 mW/cm^2 UV light in (a) air and (b) N_2. Data points represent the
average of multiple runs; error bars represent ± 1 std. dev.

Thiol-ene reactions are typically characterized by rapid reaction rates, high

conversions, and an insensitivity to oxygen. Figure 4.3a shows the reaction kinetics

between small molecule thiols and Ph-TFVE in air under UV light (1 wt.% photoinitiator,

100 mW/cm^2). As expected, the reaction rates follow the order of thiol reactivity with

M3MP, PrSH, and BnSH reaching 92%, 70%, and 15% conversion, respectively, within

1 min. TFVE conversion values at 30 min follow a similar trend with M3MP reaching 99% conversion, while PrSH and BnSH reach 87% and 70%, respectively. The thiol-TFVE reactions, when conducted in air, also exhibit a change in color from clear to orange, as shown in inset of Figure 4.3a. The thiol-TFVE reactions were further investigated under an inert nitrogen atmosphere (1 wt.% photoinitiator, 100 mW/cm^2) and the conversion versus time plots are presented in Figure 4.3b. In all cases, an increase in both the initial reaction rates and final conversion values under nitrogen were observed. M3MP and PrSH approached quantitative conversion in approximately 1 minute, whereas BnSH showed a 15% increase in overall conversion (from 70% in air to 85% in nitrogen). Thiol-TFVE reactions carried out under nitrogen also remained colorless (Figure 4.3b, inset). It is worth noting that Ph-TFVE is difficult to homopolymerize under radical conditions.[29] Unsurprisingly, TFVE homopolymerization was not observed under our reaction conditions (Appendix D – D12) indicating that TFVE consumption is solely a function of thiol addition. Changes in photoinitiator concentration improved conversions in both air and nitrogen atmospheres, but BnSH-TFVE reactions in air still failed to reach quantitative conversion (Appendix D – D13). As a final control experiment, we ran the BnSH-TFVE reaction under UV exposure in an inert atmosphere and in the absence of photoinitiator. Under these conditions, the BnSH-TFVE reaction reached ~40% conversion (Appendix D – D13) and can be attributed to UV-induced cleavage of thiol into thiyl radicals resulting in photoinitiation (a common result for thiol-ene photoreactions[30]). The absence of Irgacure precludes the possibility of Irgacure serving as a base in the reaction.[31, 32] The combined results of these experiments suggest that the SH-TFVE reaction proceeds via a radical addition pathway.
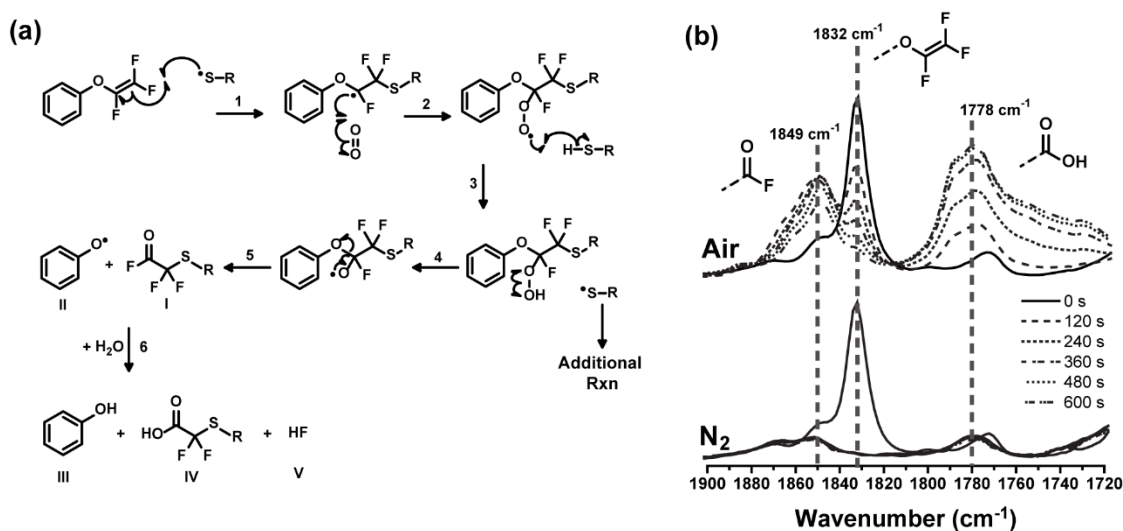
Figure 4.4 (a) Proposed mechanism for oxygen induced degradation pathway of thiol/TFVE radical reaction (b) FTIR spectrum presented at 2 minute intervals for the reaction of 1-dodecanethiol/Ph-TFVE 1 wt.% photoinitiator upon exposure to 20 mW/cm^2 UV light in air (top) and N$_2$ (bottom). Radical-radical termination reactions (e.g. disulfide formation and head-to-head coupling of carbon-centered radicals) common to thiol-ene reactions are not shown in the reaction scheme.

The differences between the kinetic results in nitrogen and air suggest that the thiol-TFVE reaction shows an increased sensitivity to oxygen. As such, we propose the oxygen induced degradation mechanism shown in Figure 4.4a. Traditionally, when oxygen interacts with the carbon-centered radical formed during the propagation step of the radical thiol-ene reaction, the formed peroxide radical can still participate in polymerization by removing the easily abstractable hydrogen of the thiol group, regenerating the propagating thiyl radical (equivalent to steps **1-3** in Figure 4.4a).[23, 33] In the case of the thiol-TFVE reaction, it appears that oxygen not only inhibits the reaction, but may also provide a pathway for product degradation (discoloration). Suspecting oxygen-induced degradation, two additional considerations are made. The first is that the hydroperoxide group formed after the reaction of the carbon-centered radical intermediate with oxygen can re-cleave to generate oxygen centered radicals (step **4** in

87

Figure 4.4a).[34-36] The second is that main chain fluoropolymers, and more specifically

perfluoroethers, can undergo β-scission when the propagating radical contains an α ether

linkage,[37] as well as several similar scission pathways when exposed to intense

irradiation (step **5** in Figure 4.4a).[38, 39] Steps **4** and **5** present a mechanistic pathway for

the decomposition of the formed hydroperoxide and the subsequent and spontaneous

scission of the addition product to form an acyl fluoride (**I**) and the stable phenoxyl

radical (**II**). The phenoxyl radical and acyl fluoride then hydrolyze in atmosphere (step

6) to yield the final decomposition products, **III**, **IV**, and **V**. Unfortunately, small

molecule separations and isolations of the degradation products were difficult and

prevented quantitative determination of degradation product structure. However,

spectroscopic techniques provided insight into the presence of the proposed carbonyl

containing degradation products. As such, a reaction between 1-dodecanethiol thiol and

phenyl trifluorovinyl ether in the presence of 1 wt.% photoinitiator and 20 mW/cm^2 UV

light was conducted over 10 minutes, and monitored in real-time using FTIR under both

air and nitrogen atmospheres (1-dodecanethiol was used to limit volatility issues and

prevent spectral overlap of functional groups). The results of the RT-FTIR study are

shown in Figure 4.4b. From Figure 4.4b, it is clear that in air, the slow disappearance of

the TFVE peak at 1832 cm^{-1} is accompanied by the appearance of two distinct peaks

centered at 1778 cm^{-1} and 1849 cm^{-1}. These peaks are associated with the products of the

oxygen degradation mechanism, and are noticeably absent when the reaction is conducted

in a nitrogen atmosphere. The peak centered at 1778 cm^{-1} is commonly identified with

the carbonyl moiety of a carboxylic acid functional group, and as such is assigned to the

formation of the stable degradation product, **IV**. The peak at 1849 cm^{-1} appears in a

region associated with acyl fluorides[40] and is assigned to the formation of degradation product, **I**, in good agreement with literature values for $-SCF_2COF$ IR absorptions.[41] It is also worth noting that the intensity of the $-COF$ peak quickly increased, before decreasing at longer times. The quick appearance of $-COF$ followed by its disappearance coupled with the continuous formation of $-COOH$, can be explained by the hydrolysis of the acyl fluoride, **I**, to the carboxylic acid, **IV**, as shown in step **6** of Figure 4.4a. Furthermore, two distinct singlets at -83.2 ppm and -83.6 ppm are displayed in the ^{19}F NMR spectrum of the product mixture in air, in agreement with literature values for the chemical shifts of CF_2 fluorines adjacent to carbonyl carbons (Appendix D – D14).[41, 42] The CF_2 peaks were not observed by ^{19}F NMR for reactions conducted under N_2.
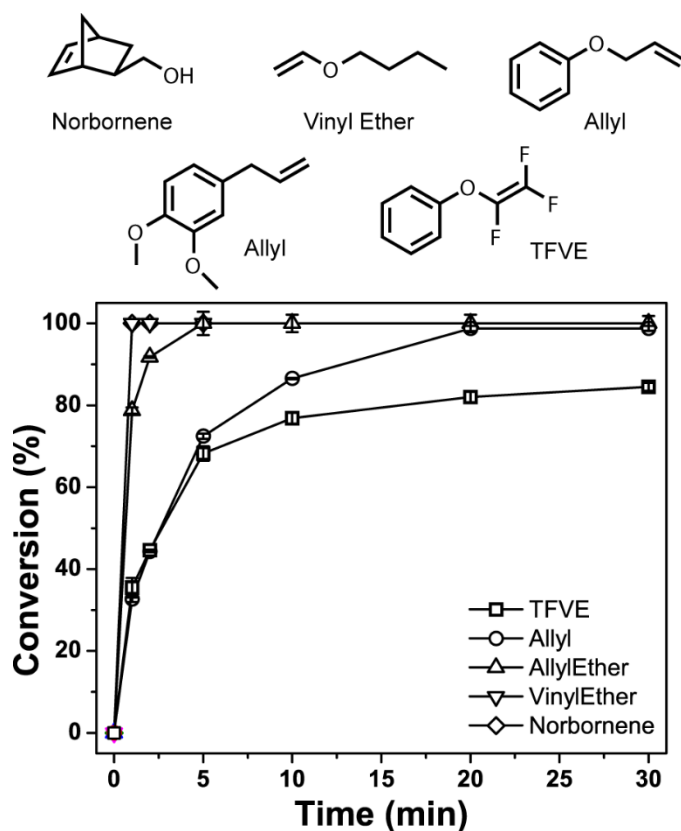

Figure 4.5 Alkene monomer structures and conversion kinetics for BnSH/alkene reactions conducted at 1 wt.% photoinitiator and 100 mW/cm^2 UV light in N_2.

After identifying the oxygen-sensitive nature of the thiol-TFVE photoreaction, subsequent experiments were conducted under nitrogen. Given the electron deficiency of the TFVE group, the kinetics and efficiency of the thiol-TFVE reaction were somewhat unexpected. To provide a point of reference, we ran the thiol-TFVE reaction parallel to thiol-ene reactions that employ more traditional electron-rich alkenes, such as norbornene, vinyl ether, allyl ether, and allyl groups, and the results are shown in Figure 4.5. BnSH, as the least reactive thiol of the series, was chosen for the alkene comparison experiment to enable facile capture of the kinetics. In each case, BnSH and the alkene were combined in the absence of solvent with 1 wt.% photoinitiator and reacted in an inert N_2 atmosphere for 30 minutes under 100 mW/cm^2 UV light intensity. As shown in Figure 4.5, the TFVE group is less reactive and exhibits slower reaction kinetics with BnSH than norbornene, vinyl ether, and allyl ether. However, TFVE reaction rates with BnSH are comparable to allyl reaction rates, though these reactions do not reach the same final conversions after 30 min. It is noteworthy that the kinetics of thiol-TFVE and thiol-ene reactions are indistinguishable (e.g. quantitative conversions within 1 min) when employing more reactive thiols, such as M3MP and PrSH. The unexpected reactivity of the TFVE group is a function of both the carbon-centered radical intermediate, and the lability of the thiol hydrogen. Following the propagation step, the carbon-centered radical sits alpha to the ether linkage which can inductively stabilize the radical,[43] lowering the energy barrier to addition. Following radical addition, the easily abstractable thiol hydrogen facilitates the chain-transfer step and the reaction proceeds as previously described. Encouraged by these results, we next explored the thiol-TFVE reaction for synthesis of semi-fluorinated polymer networks.

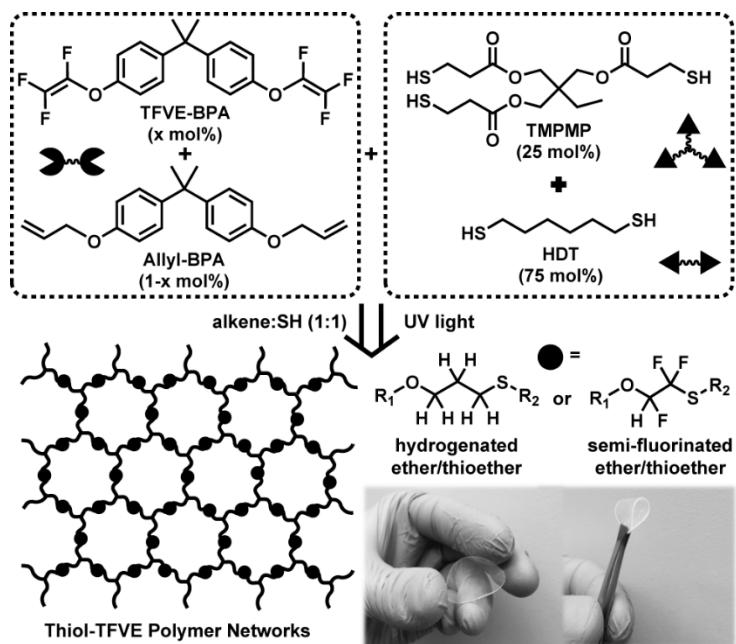**4.4.2 Semi-Fluorinated Networks**

Figure 4.6 Thiol/TFVE multifunctional network monomers and network preparation. Hydrogenated and semi-fluorinated ether/thioether linkages shown on left.

The rapid and efficient reaction kinetics between the TFVE and a variety of thiols make the thiol-TFVE photoreaction an ideal candidate to rapidly synthesize semi-fluorinated polymer networks with highly tunable properties. Therefore, a difunctional TFVE monomer based on bisphenol A (TFVE-BPA) was synthesized and formulated with di- and trifunctional thiol monomers, as shown Figure 4.6 (Appendix D – D15-D22 for NMR spectrum of synthesized difunctional monomers; a 75:25 SH mol ratio of HexSH$_2$:TMPMP was used to ensure monomer mixture homogeneity). TFVE-BPA was copolymerized with allyl-BPA to tailor the amount of semi-fluorinated linkages in the network and determine the effect of the TFVE group on the photopolymerization process. The structural similarity of allyl-BPA serves as a control to determine the influence of the semi-fluorinated linkage on polymer network properties. All formulations contained 1
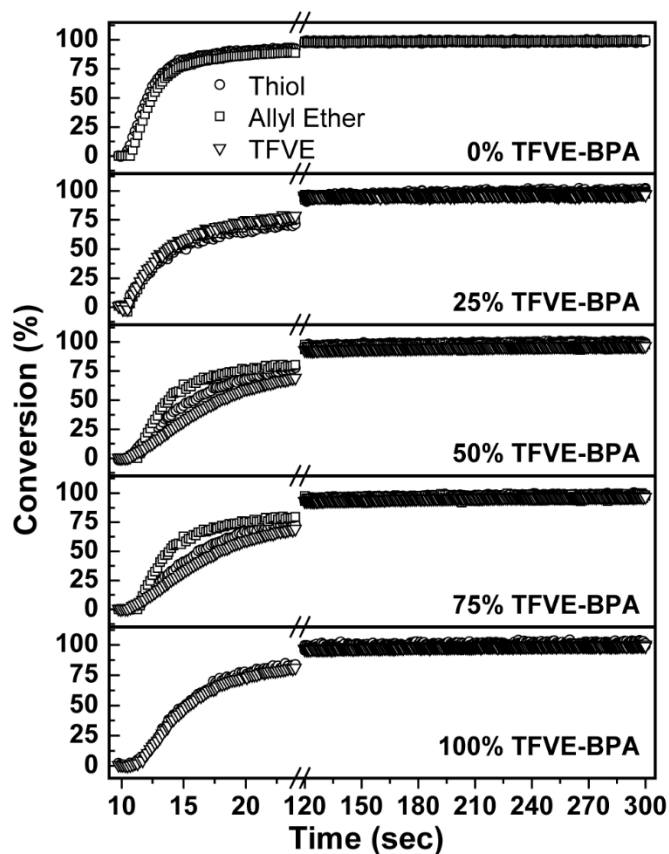
Figure 4.7 Real-time FTIR conversion plots of thiol/TFVE networks formulated with 0-100 mol % TFVE-BPA.

wt.% Irgacure 1173 and were polymerized with 20 mW/cm^2 UV light under an inert N$_2$ atmosphere. The mol % of TFVE groups was systematically varied from 0 mol % to 100 mol %. The polymerization kinetics as a function of TFVE-BPA concentration are shown in Figure 4.7. After 30 seconds, the 0% TFVE-BPA and 100% TFVE-BPA formulations respectively approached 95% and 85% functional group conversions, while maintaining a 1:1 thiol:alkene stoichiometry throughout the photopolymerization. In copolymerizations of TFVE-BPA and allyl-BPA, the difference in polymerization rate between the allyl ether and the TFVE groups can be observed early in the reaction, with the allyl ether groups reaching an approximately 6% higher conversion than the TFVE

groups at 30 seconds for the 50% and 75% TFVE-BPA formulations. The lower

reactivity of the TFVE group in the thiol-ene copolymerization is consistent with the

small molecule kinetics presented in Figure 4.5, as the allyl ether group is a more reactive

alkene under the current reaction conditions. However, after 2 minutes of UV exposure,

all network formulations reached near quantitative conversion with stoichiometric

conversion of all functional groups. These results confirm that under inert atmosphere,

semi-fluorinated networks can be rapidly synthesized, and that the TFVE group exerts

little to no influence on final conversion values.

The influence of the semi-fluorinated ether/thioether linkage on the

thermomechanical properties of the thiol-TFVE networks was investigated using

dynamic mechanical analysis (strain film mode, heating rate 2 °C/min). The glass

transition was taken as the peak maximum of the tan δ curves. Figure 4.8a shows the tan

δ curves of the thiol-TFVE networks as a function of TFVE-BPA concentration. At all

loadings of TFVE-BPA, the tan δ curves exhibit a narrow full width at half max (< 13

°C) and are characteristic of homogeneous polymer networks formed via a thiol-ene

radical step-growth mechanism.[44] Significant increases in T_g were observed as a function

of the semi-fluorinated ether/thioether linkage, with the T_g increasing from 7.1±1.3 °C, at

0% TFVE, to 29.2±2.3 °C, at 100% TFVE – an increase of more than 20 °C.

Interestingly, crosslink densities calculated from the rubbery plateau regions ($T_g + 40$ °C)

of the storage modulus curves (Figure 4.8b, Table 4.1) remain relatively constant.

Therefore, the observed increases in T_g are a function of the changes in the nature of the

crosslinks within the backbone of the polymer network. At 0% TFVE-BPA, the radical

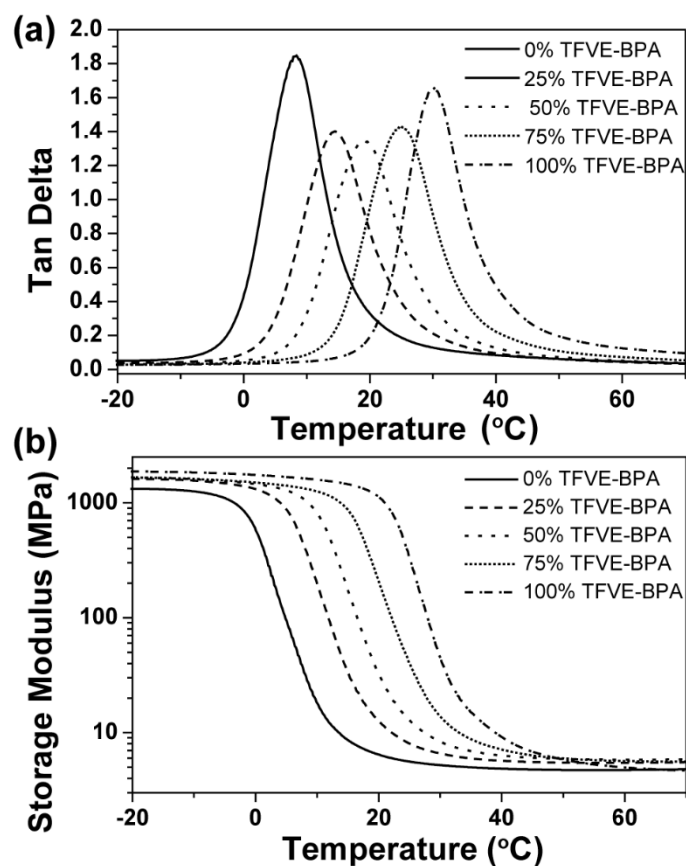addition of the thiol to the allyl-BPA results in the flexible ether/thioether linkage (Figure

93

Figure 4.8 Representative thermomechanical plots of 0-100 mol % TFVE-BPA polymer networks (a) Tan δ vs. temperature (b) Storage modulus vs. temperature.

Table 4.1

Thermomechanical Properties of 0-100 mol % TFVE-BPA Thiol/TFVE Polymer

Networks.

mol TFVE-BPA	T_g (°C)	fwhm (°C)[a]	ρ_x (mol cm^{-3}10^3)[b]
0	7.1±1.3	11.2±0.6	0.620±0.023
25	13.8±0.6	11.1±1.3	0.641±0.028
50	18.1±0.9	12.3±0.5	0.664±0.039
75	25.0±1.7	12.3±0.9	0.603±0.071
100	29.2±2.3	10.6±0.2	0.544±0.033

[a] fwhm obtained from tan δ curve [b]Crosslink density

4.6). As the allyl-BPA is replaced with TFVE-BPA, the majority of chemical linkages

formed within the polymer network are semi-fluorinated ether/thioethers (Figure 4.6).

94

The increase in T_g as a function of semi-fluorinated linkage can be attributed to a combination of factors. The incorporation of fluorine has been shown to increase the rigidity of polymers,[45, 46] as well as prevent certain modes of rotation through steric and electronic effects.[47] Additionally, the strong electron withdrawing nature of fluorine is capable of increasing the acidity of adjacent hydrogen atoms to facilitate hydrogen bonding.[48-50] The incorporation of large amounts of semi-fluorinated linkages therefore not only stiffens the ether/thioether linkage, but also provides a large number of hydrogen bonding sites, which effectively act as physical crosslinks.[51] The result is most dramatic when all alkenes are fluorinated, with the T_g of the material transitioning from a flexible rubber (0% TFVE) to a semi- glass like state (100% TFVE) at room temperature.
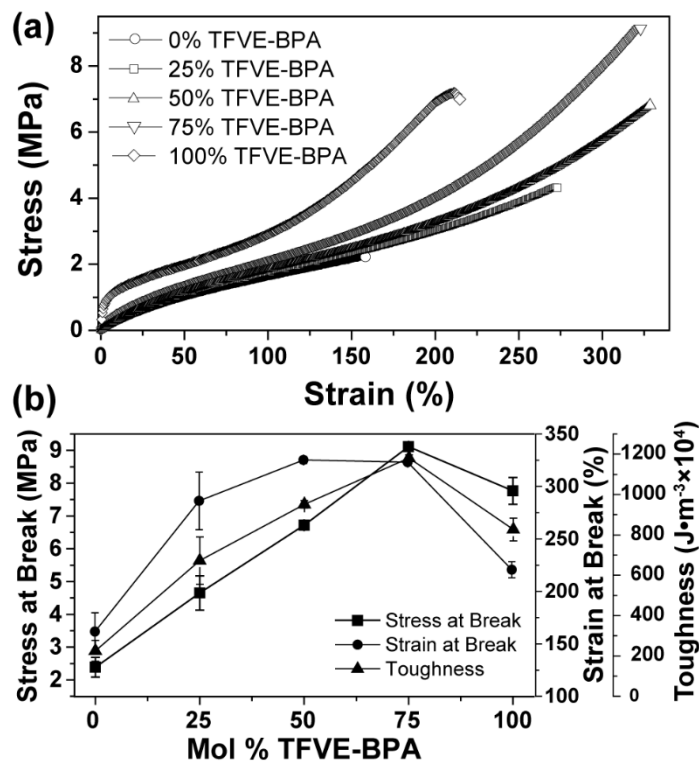

Figure 4.9 (a) Representative stress/strain curves of 0-100 mol % TFVE-BPA thiol/TFVE networks (b) Summation of thiol/TFVE polymer network tensile properties as a function of mol % TFVE-BPA. Results indicate a peak in mechanical properties at 75 mol % TFVE-BPA.

The influence of the semi-fluorinated ether/thioether linkage is also evident in the mechanical properties of the thiol-TFVE networks. Representative stress-strain curves are shown in Figure 4.9a and summarized in Figure 4.9b. In general, both stress at break and strain at break values increased with increasing TFVE-BPA concentration, with the 50-75% TFVE-BPA networks exhibiting a 2-fold increase in strain at break relative to the 0% TFVE-BPA sample. It is also clear that increasing the concentration of semi-fluorinated linkage within the network results in a 5-fold increase in toughness, peaking at 75 mol % TFVE, relative to the non-fluorinated network (0% TFVE). The 100% TFVE network showed a significant increase in initial modulus; however, a decrease in toughness was observed relative to the 50-75% TFVE samples. The decrease is toughness can be attributed to the more glass-like behavior of the 100% TFVE, as tensile testing was conducted at a temperature (25 °C) just below T_g. The increase in toughness with increasing semi-fluorinated linkage is attributed to an increase in the bond strength of the chemical crosslinks and to the contribution of hydrogen bonding to the absorption of mechanical deformation energy. Due to the inductive effect of fluorine on the skeletal carbon-carbon bonds, the semi-fluorinated ether-thioether linkage (HFC–CF$_2$) is expected to be stronger than the carbon-carbon bond of the hydrogenated ether-thioether linkage (H$_2$C–CH$_2$), which likely translates into an increase in mechanical toughness of the thiol-TFVE network at higher concentrations of TFVE-BPA. Simultaneously, the semi-fluorinated linkage provides hydrogen bonding sites as physical crosslinks that are capable of absorbing the energy of mechanical deformation and rupturing before the covalent crosslinks.[52] Ultimately, incorporating semi-fluorinated ether-thioether linkages

via thiol-TFVE photopolymerization provides a facile route to enhance the mechanical

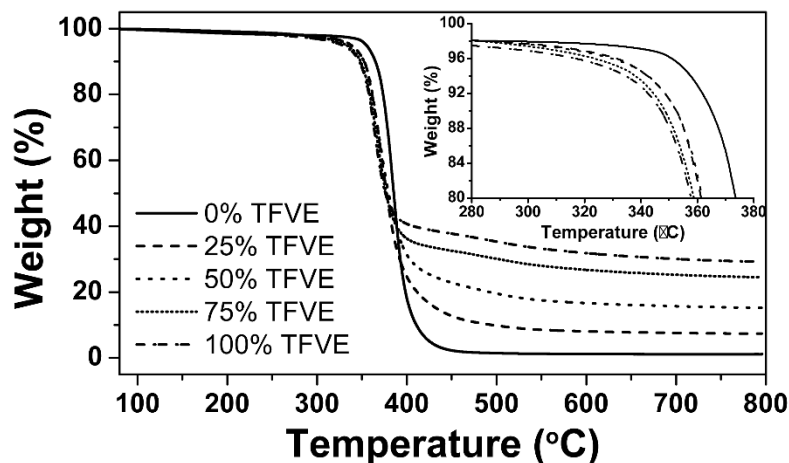properties of thiol-ene polymer networks.

Figure 4.10 Representative thermal degradation behavior of thiol/TFVE networks in a N_2
atmosphere. The inset shows a more detailed view of the onset region.

Table 4.2

Summary of Thermal Degradation Temperatures of Thiol/TFVE Polymer Networks.

mol TFVE-BPA	T_{d5} (°C)	T_{d10} (°C)	1st Deriv. Wt.% (°C)	Char Yield (%)
0	349.9±3.7	359.4±4.0	378.6±4.6	0.7±0.5
25	332.6±3.5	346.9±4.2	365.7±5.0	7.9±0.4
50	332.6±2.9	345.6±4.1	362.9±3.0	16.2±2.6
75	325.2±4.2	342.2±3.7	361.4±3.6	23.6±0.8
100	323.2±3.2	342.1±3.5	359.1±3.6	28.9±1.4

Thermogravimetric analysis was used to characterize the thermal stability of the

thiol-TFVE polymer networks. Samples were subjected to a 10 °C/min ramp rate from

30 to 800 °C under a nitrogen atmosphere. Figure 4.10 shows the TGA thermograms for

the thiol-TFVE samples as a function of TFVE-BPA concentration. The data is

summarized in Table 4.2. As illustrated by the 5% weight loss values (T_{d5}%), the onset

of thermal degradation depends on the concentration of semi-fluorinated ether-thioether

in the network, where the highest $T_{d5}\%$ was observed for the 0% TFVE-BPA sample.

Thiol-TFVE networks containing 25, 50, 75, and 100% TFVE-BPA showed $T_{d5}\%$ values

respectively at 332.6±3.5, 332.6±2.9, 325.2±4.2, and 323.2±3.2 °C. The decrease in

onset of degradation, though minimal between the semi-fluorinated polymer networks, is

significant from the 0% TFVE-BPA network to the 100% TFVE-BPA network ($T_{d5}\%$

values shifted ~30 °C and the 1st derivative of weight percent values shifted ~20 °C).

The change in thermal degradation behavior for the semi-fluorinated networks is

rationalized by an increase in abstractable hydrogens as more semi-fluorinated linkage is

incorporated into the polymer.[48] Hydrogen abstraction is a common fluoropolymer

degradation pathway and may result in the formation of HF, along with the initiation of

several radical scission pathways.[38, 53] HF thermally released from the polymer has the

potential to form inorganic salts leading to an increase in char yield (an advantageous

property for fire resistant materials), as illustrated by the increase from 0.7±0.5% at 0%

TFVE-BPA, to 28.9±1.4% at 100% TFVE-BPA.
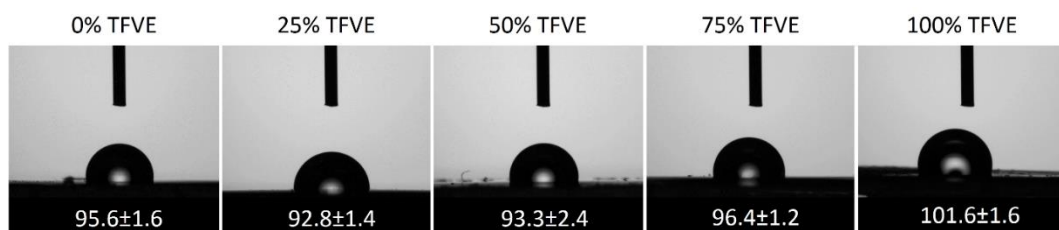
Figure 4.11 Static water contact angle measurements of 0% to 100% TFVE containing thiol-ene films.

Finally, contact angle measurements show the static water contact angle increases

from 95.6±1.6° at 0% TFVE to 101.6±1.6° at 100% TFVE (Figure 4.11). The increased

hydrophobicity of the networks with increasing TFVE-BPA concentration is attributed to

the contribution of the semi-fluorinated ether/thioether linkage to lower the surface

energy – an advantageous property for applications necessitating moisture resistance. The observed contact angles are consistent with other materials reported in literature that are derived from TFVE-based monomers.[13]

4.5 Conclusions

In summary, we have demonstrated the first example of thiol-trifluorovinyl ether photopolymerization as a facile synthetic route to semi-fluorinated polymer networks. The thiol-TFVE reaction – including anti-Markovnikov addition product and reaction kinetics with various thiols – was elucidated using small molecule model reactions. An oxygen-induced degradation pathway was identified and a mechanism, supported by NMR and FTIR spectroscopy, was proposed; however, this side reaction was circumvented by performing the reactions under a nitrogen atmosphere. Photopolymerization of difunctional TFVE monomers with multifunctional thiols occurred with rapid kinetics and high conversions, and provided homogeneous semi-fluorinated polymer networks with narrow glass transitions – all hallmark characteristics of the radical step-addition process. Directly incorporating the semi-fluorinated ether/thioether linkage into the polymer network yielded hydrophobic materials with increased T_g, a 2-fold increase in strain at break, 4-fold increase in stress at break, and more than 5-fold increase in toughness relative to a thiol-ene material composed of a structurally similar hydrogenated ether/thioether linkage. We anticipate that the simplicity and rapid cure kinetics of the thiol-TFVE photopolymerization coupled with on-demand access to tunable and enhanced materials properties will provide a framework for the design of new semi-fluorinated polymer thermosets for a range of applications.

4.6 References

(1). Maier, G. Low Dielectric Constant Polymers for Microelectronics *Prog. Polym. Sci.* **2001,** *26*, 3-65.

(2). Liu, F.; Hashim, N. A.; Liu, Y.; Abed, M. R. M.; Li, K. Progress in the Production and Modification of Pvdf Membranes *J. Membrane Sci.* **2011,** *375*, 1-27.

(3). Améduri, B.; Boutevin, B.; Kostov, G. Fluoroelastomers: Synthesis, Properties and Applications *Prog. Polym. Sci.* **2001,** *26*, 105-187.

(4). Cui, Z.; Drioli, E.; Lee, Y. M. Recent Progress in Fluoropolymers for Membranes *Prog. Polym. Sci.* **2014,** *39*, 164-198.

(5). Scheirs, J., *Modern Fluoropolymers*. Wiley: New York, 1997.

(6). Iacono, S. T.; Budy, S. M.; Jin, J.; Smith, D. W. Science and Technology of Perfluorocyclobutyl Aryl Ether Polymers *J. Polym. Sci. A: Polym. Chem.* **2007,** *45*, 5705-5721.

(7). Babb, D. A.; Ezzell, B. R.; Clement, K. S.; Richey, W. F.; Kennedy, A. P. Perfluorocyclobutane Aromatic Ether Polymers *J. Polym. Sci. A: Polym. Chem.* **1993,** *31*, 3465-3477.

(8). Jin, J.; Iacono, S. T.; Smith, D. W. Semifluorinated Polymers from Trifluorovinyl Aromatic Ether Monomers. In *Handbook of Fluoropolymer Science and Technology*, John Wiley & Sons, Inc.: Hoboken, 2014, 343-361.

(9). Jin, J. Chemistry of Aryl Trifluorovinyl Ethers *Chemistry in New Zealand* **2012,** *76*, 24-26.

(10). Rico, I.; Wakselman, C. Condensation of 1,2-Dibromotetrafluoroethane with Various Potassium Thiophenoixdes and Phenoxides *J. Fluor. Chem.* **1982,** *20*, 759-764.

(11). Li, J.; Qiao, J. X.; Smith, D.; Chen, B.-C.; Salvati, M. E.; Roberge, J. Y.; Balasubramanian, B. N. A Practical Synthesis of Aryl Tetrafluoroethyl Ethers Via the Improved Reaction of Phenols with 1,2-Dibromotetrafluoroethane *Tetrahedron Lett.* **2007,** *48*, 7516-7519.

(12). Brown, D. K.; Iacono, S. T.; Cracowski, J.-M.; Christensen, K.; Smith, D. W. Synthesis and Characterization of a Biphenyl Perfluorocyclobutyl (Bp-Pfcb) Polyethylene Glycol (Peg) Blend Compatibilizer *Polym. Adv. Technol.* **2016**, 1389-1396.

(13). He, F.; Gao, Y.; Jin, K.; Wang, J.; Sun, J.; Fang, Q. Conversion of a Biorenewable Plant Oil (Anethole) to a New Fluoropolymer with Both Low Dielectric Constant and Low Water Uptake *ACS Sustainable Chem. Eng.* **2016,** *4*, 4451-4456.

(14). Wang, J.; Jin, K.; Sun, J.; Fang, Q. Dendrimeric Organosiloxane with Thermopolymerizable -Ocf=F2 Groups as the Arms: Synthesis and Transformation to the Polymer with Both Ultra-Low K and Low Water Uptake *Polym. Chem.* **2016,** *7*, 3378-3382.

(15). Wong, S.; Ma, H.; Jen, A. K. Y.; Barto, R.; Frank, C. W. Highly Fluorinated Trifluorovinyl Aryl Ether Monomers and Perfluorocyclobutane Aromatic Ether Polymers for Optical Waveguide Applications *Macromolecules* **2003,** *36*, 8001-8007.

(16). Smith, D. W.; Babb, D. A. Perfluorocyclobutane Aromatic Polyethers. Synthesis and Characterization of New Siloxane-Containing Fluoropolymers *Macromolecules* **1996,** *29*, 852-860.

(17). Liu, S.; Jiang, X.; Ma, H.; Liu, M. S.; Jen, A. K. Y. Triarylamine-Containing Poly(Perfluorocyclobutane) as Hole-Transporting Material for Polymer Light-Emitting Diodes *Macromolecules* **2000,** *33*, 3514-3517.

(18). Ma, H.; Wu, J.; Herguth, P.; Chen, B.; Jen, A. K. Y. A Novel Class of High-Performance Perfluorocyclobutane-Containing Polymers for Second-Order Nonlinear Optics *Chem. Mater.* **2000,** *12*, 1187-1189.

(19). Klukovich, H. M.; Kean, Z. S.; Iacono, S. T.; Craig, S. L. Mechanically Induced Scission and Subsequent Thermal Remending of Perfluorocyclobutane Polymers *J. Am. Chem. Soc.* **2011,** *133*, 17882-17888.

(20). Zhu, Y.; Huang, Y.; Meng, W.-D.; Li, H.; Qing, F.-L. Novel Perfluorocyclobutyl (Pfcb)-Containing Polymers Formed by Click Chemistry *Polymer* **2006,** *47*, 6272-6279.

(21). Harris, J. F.; Stacey, F. W. The Free Radical Addition of Trifluoromethanethiol to Fluoroolefins *J. Am. Chem. Soc.* **1960,** *83*, 840-844.

(22). Harris, J. F. The Free Radical Addition of Hydrogen Sulfide to Fluoroethylenes *J. Am. Chem. Soc.* **1962,** *84*, 3148-3153.

(23). Hoyle, C. E.; Bowman, C. N. Thiol-Ene Click Chemistry *Angew. Chem. Int. Ed.* **2010,** *49*, 1540-1573.

(24). Lowe, A. B. Thiol-Ene "Click" Reactions and Recent Applications in Polymer and Materials Synthesis: A First Update *Polym. Chem.* **2014,** *5*, 4820-4870.

(25). Xiong, L.; Kendrick, L. L.; Heusser, H.; Webb, J. C.; Sparks, B. J.; Goetz, J. T.; Guo, W.; Stafford, C. M.; Blanton, M. D.; Nazarenko, S.; Patton, D. L. Spray-Deposition and Photopolymerization of Organic–Inorganic Thiol–Ene Resins for Fabrication of Superamphiphobic Surfaces *ACS Appl. Mater. Interfaces* **2014,** *6*, 10763-10774.

(26). Lin, H.; Wan, X.; Jiang, X.; Wang, Q.; Yin, J. A "Thiol-Ene" Photo-Curable Hybrid Fluorinated Resist for the High-Performance Replica Mold of Nanoimprint Lithography (Nil) *J. Mater. Chem.* **2012,** *22*, 2616-2623.

103

(27). Sangermano, M.; Bongiovanni, R.; Malucelli, G.; Priola, A.; Harden, A.; Rehnberg, N. Synthesis of New Fluorinated Allyl Ethers for the Surface Modification of Thiol–Ene Ultraviolet-Curable Formulations *J. Polym. Sci. A: Polym. Chem.* **2002,** *40*, 2583-2590.

(28). D'Souza, V. T.; Nanjundiah, R.; Baeza, J.; Szmant, H. H. Thiol-Olefin Cooxidation (Toco) Reaction. 7. A [1]h Nmr Study of Thiol Solvation *J. Org. Chem.* **1987,** *52*, 1720-1725.

(29). Antonucci, J. M. The Synthesis and Polymerization of Fluorostyrenes and Fluorinated Vinyl Phenyl Ethers. In *Fluoropolymers*, Wall, L. A., Ed. John Wiley & Sons, Inc.: New York, NY, 1972, 33-82.

(30). Cramer, N. B.; Scott, J. P.; Bowman, C. N. Photopolymerizations of Thiol−Ene Polymers without Photoinitiators *Macromolecules* **2002,** *35*, 5361-5365.

(31). Cîrkva, V.; Polák, R.; Paleta, O. Radical Additions to Fluoroolefins. Photochemical Fluoroalkylation of Alkanols and Alkane Diols with Perfluoro Vinyl Ethers; Photo-Supported O-Alkylation of Butane-1,4-Diol with Hexafluoropropene *J. Fluor. Chem.* **1996,** *80*, 135-144.

(32). Timperley, C. M. Fluoroalkene Chemistry: Part 2. Reactions of Thiols with Some Toxic 1,2-Dichlorinated Polyfluorocycloalkenes *J. Fluor. Chem.* **2004,** *125*, 1265-1272.

(33). O'Brien, A. K.; Cramer, N. B.; Bowman, C. N. Oxygen Inhibition in Thiol–Acrylate Photopolymerizations *J. Polym. Sci. A: Polym. Chem.* **2006,** *44*, 2007-2014.

(34). Rabek, J. F. Photochemical Aspects of Degradtion of Polymers. In *Polymer Photodegradation*, Springer Netherlands: 1995, 24-66.

(35). Chiantore, O.; Trossarelli, L.; Lazzari, M. Photooxidative Degradation of Acrylic and Methacrylic Polymers *Polymer* **2000,** *41*, 1657-1668.

(36). Herman, M. F., *Encyclopedia of Polymer Science and Technology*. 3rd ed.; Wiley: New Jersey, 2007.

(37). Yuan, Y.; Schoichet, M. S. Insights into the Properties of Novel Trifluorovinyl Ether Copolymers *Macromolecules* **1999,** *32*, 2669-2674.

(38). Dargville, T. R.; George, G. A.; HIll, D. J. T.; Scheler, U.; Whittaker, A. K. High-Speed Mas 19f Nmr Analysis of an Irradiated Fluoropolymer *Macromolecules* **2002,** *35*, 5544-5549.

(39). Lappan, U.; Geißler, U.; Scheler, U.; Lunkwitz, K. Identification of New Chemical Structures in Poly(Tetrafluoroethylene-Co-Perfluoropropyl Vinyl Ether) Irradiated in Vacuum at Different Temperatures *Radiat. Phys. Chem.* **2003,** *67*, 447-451.

(40). Cohen, O.; Sasson, R.; Rozen, S. A New Method for Making Acyl Fluorides Using Brf3 *J. Fluor. Chem.* **2006,** *127*, 433-436.

(41). Nguyen, T.; Wakselman, C. A New Route to Perfluorinated Sulphonic Acid Resin Intermediates *Eur. Polym. J.* **1991,** *27*, 435-438.

(42). Ciampello, F.; Venturi, M. T.; Sianesi, D. The 19f Chemical Shift in Oxygen Containing Carbon Fluorine Products *Org. Magn. Resonance* **1969,** *1*, 281-293.

(43). Henry, D. J.; Parkinson, C. J.; Mayer, P. M.; Radom, L. Bond Dissociation Energies and Radical Stabilization Energies Associated with Substituted Methyl Radicals *J. Phys. Chem. A* **2001,** *105*, 6750-6756.

(44). Hoyle, C. E.; Lee, T. Y.; Roper, T. Thiol–Enes: Chemistry of the Past with Promise for the Future *J. Polym. Sci. A: Polym. Chem.* **2004,** *42*, 5301-5338.

(45). Teng, H. Overview of the Development of the Fluoropolymer Industry *Appl. Sci.* **2012,** *2*, 496-512.

(46). Rigby, H. A.; Bunn, C. W. A Room-Temperature Transition in Polytetrafluoroethylene *Nature* **1949,** *164*, 583-585.

(47). Boufflet, P.; Hang, Y.; Fei, Z.; Treat, N. D.; Li, R.; Smilgies, D.-M.; Stingelin, N.; Anthopoulos, T. D.; Heeney, M. Using Molecular Design to Increase Hole Transport: Backbone Fluorination in the Benchmark Material Poly(2,5-Bis(3-Alkylthiophen-2-Yl)Thieno[3,2-*B*-]-Thiophene (Pbttt) *Adv. Func. Mater.* **2015,** *25*, 7038-7048.

(48). Moody, J. D.; VanDerveer, D.; Smith Jr., D. W.; Iacono, S. T. Synthesis of Internal Fluorinated Alkenes Via Facile Aryloxylation of Substituted Phenols with Aryl Trifluorovinyl Ethers *Org. Biomol. Chem.* **2011,** *9*, 4842-4849.

(49). Alkorta, I.; Rozas, I.; Elguero, J. Effects of Fluorine Substitution on Hydrogen Bond Interactions *J. Fluor. Chem.* **2000,** *101*, 233-238.

(50). Paul, A.; Griffiths, P. C.; James, R.; Willock, D. J.; Rogueda, P. G. Explaining the Phase Behaviour of the Pharmaceutically Relevant Polymers Poly(Ethylene Glycol) and Poly(Vinyl Pyrrolidone) in Semi-Fluorinated Liquids *J. Pharm. Pharmacol.* **2005,** *57*, 973-980.

(51). Kwei, T. K. The Effect of Hydrogen Bonding on the Glass Transition Temperatures of Polymer Mixtures *J. Polym. Sci. Polym. Lett. Ed.* **1984,** *22*, 307-313.

(52). Hayashi, M.; Noro, A.; Matsushita, Y. Highly Extensible Supramolecular Elastomers with Large Stress Generation Capability Originating from Multiple Hydrogen Bonds on the Long Soft Network Strands *Macromol. Rapid Commun.* **2016,** *37*, 678-684.

(53). Zulfiqar, S.; Zulfiqar, M.; Rizvi, M.; Munir, A.; McNeill, I. C. Study of the Thermal Degradation of Polychlorotrifluoroethylene, Poly(Vinylidene Fluoride) and Copolymers

of Chlorotrifluoroethylene and Vinylidene Fluoride *Polym. Degrad. Stab.* **1994,** *43*, 423-430.

CHAPTER V – SUMMARY AND FUTURE OUTLOOKS

In closing, this dissertation presents the utility and value in using thiol-ene chemistry to impart function to well-defined polymeric materials, while also providing a platform for the investigation of a new chemistries influence on structure-property relationships.

In Chapter II, we reported the use of a catechol monomer derived from the naturally occurring extracts of clove oil to develop mussel-inspired adhesives that exhibited improved adhesion to a variety of substrates. The use of thiol-ene photopolymerizations enabled rapid polymerization times, on-demand curing, and solvent-free processing conditions. Increasing the concentration of the catechol within the polymer network lead to increased dry adhesive strength, though simultaneously resulted in decreased thermomechanical and mechanical properties, due to the increased concentration of a monofunctional monomer and the radical inhibition effect of the catechol. Ultimately, Chapter II demonstrated the balance between adhesive and cohesive adhesion forces within a thiol-ene resin, revealing that the catechol, while adhesive, may limit radically polymerized materials to applications requiring lower modulus values.

Chapter III extended the work done in Chapter II by investigating the utility of the catechol-based thiol-ene adhesives in underwater applications. For a thiol-ene network containing a catechol adhesive monomer only, virtually no underwater adhesion was achieved. However, drawing additional inspiration from the underwater binding of the marine mussel, the inclusion of hydrophobic groups, specifically a perfluoroalkyl chain, lead to increased adhesion under completely submerged, and less stringent "wet"

conditions. The reported results were moderately surprising, as perfluoroalkyl groups are commonly considered non-adhesive. However, the use of a hydrophobic moiety in an underwater adhesive facilitated the removal of detrimental water from the substrate/adhesive resin interface, allowing a more uniform and intimate adhesive contact. Serendipitously, the inclusion of the hydrophobic chain also lead to increased polymerization conversions, mitigating the inhibitory effects of the catechol moiety observed in Chapter II.

Finally, Chapter IV reported the utilization of the trifluorovinyl ether group to develop rapidly synthesized, homogenous semi-fluorinated polymer networks. The inclusion of the TFVE group led to dramatic improvements in the thiol-ene thermomechanical and mechanical properties due to a combination of the increased C-F and C-C bond strengths, and the increased hydrogen bonding present in the polarized semi-fluorinated ether/thioether linkage. Unfortunately, the SH-TFVE reaction exhibited a sensitivity to oxygen, with spectroscopic evidence indicating a spontaneous cleavage of the forming ether/thioether linkage. However, oxygen sensitivity may be readily circumvented by conducting polymerizations in inert atmosphere, and the resulting polymerizations demonstrate a new and efficient pathway to the generation of semi-fluorinated materials.

The results presented above point to the utility of using the thiol-ene photopolymerization to synthesize functional thiol-ene adhesives and high toughness semi-fluorinated polymer networks. As such, it is recommended that additional studies probe deeper into the underlying mechanisms of action. For hydrophobic catechol-based adhesives, an investigation into the morphology of the thin films, and their corresponding

water diffusion coefficients would facilitate a micro and nanoscale understading of how water may be pushed away from a substrate interface. It is expected that the presence of water in the thin film would leave observable voids in the film morphology, decreasing the adhesive contact area and therefore adhesive strength. Further, the serendipitous increase in polymerization conversions as a function of chain end concentration is unexpected, and currently not understood. It may be possible to increase the concentration of catechol in the adhesive resin, resulting in greater adhesive strengths, if the inhibitory effects of the catechol can be mitigated by the presence of long pendant chains. For the semi-fluorinated thiol-ene networks, the observed increase in toughness is impressive when compared to the traditionally brittle nature of thiol-ene polymers. Therefore, it is worth investigating if the inclusion of TFVE-based monomers can impart toughness to a range of thiol-ene networks. The improvement in mechanical strength may lead to a greater number of thiol-ene materials being implemented in applied, and mechanically demanding applications. Further, the TFVE monomer structure may be readily altered to influence the polymeric mechanical properties (i.e. improved elasticity). Finally, the major drawback of the SH-TFVE photoreaction is the oxygen sensitivity. It is believed that the ability to form a stabilized phenoxy radical facilitates the spontaneous degradation observed under UV polymerization conditions. If a TFVE monomer could be synthesized such that no stable radical could be formed, oxygen sensitivity may be mitigated, restoring one of the primary benefits of the thiol-ene radical reaction.

APPENDIX A – HIGH REFRACTIVE INDEX THIN FILMS

FROM THIOL-ENE/SOL-GEL NETWORKS

A.1 Abstract

Herein we report the synthesis of hybrid organic/inorganic thiol-ene/TiO_2 thin films prepared from a sol-gel method. By selectively controlling the wt.% of titanium isopropoxide (a TiO_2 precursor) included in the sol-gel process, thin films of varying refractive index ($n = 1.65$ to 1.88) were developed that displayed a high transparency to visible light – ideal properties for optical applications. The inclusion of an organic thiol-ene polymer matrix synergistically increased the refractive index of the hybrid thin films relative to an acrylate control. By subjecting the sol-gel formulations to an aging process, increased film thickness was achieved and the morphology of the thin films may be adjusted by variation in the aging method.

A.2 Introduction

High refractive index polymers and composites have received wide attention due to their potential use in optical applications including microlens arrays[1, 2], waveguides[3], displays[4, 5], and organic light emitting diodes (OLEDs).[6, 7] As optoelectronic devices decrease in size, more efficient and scalable materials are required to maintain and improve device performance. While polymeric materials have facilitated decreased size in optoelectronic devices, a major challenge associated with such devices is the output efficiency of generated light. Owing to differences in refractive index within the device layers, significant amounts of generated light are lost to internal reflection and waveguiding modes within an individual layer.[8] As such, several research efforts are focused on utilizing refractive index matching internal and external layers. Externally,

the major approaches involve matching the refractive index of the electrode layer (typically indium tin oxide, ITO, n ~1.8) with the protective substrate layer (commonly glass, n ~1.5) to prevent internal reflection in the ITO layer, or using a macro-extractor placed on top of the glass layer ($n = 1.5 – 1.8$) to limit the optical loss in air ($n = 1.0$). Internally, high refractive index scattering layers usually consisting of high refractive index nanoparticles dispersed in a low refractive index polymer matrix, not only disrupt internal reflection modes, but also facilitate increased control over the direction and wavelength of output light.[8]

While several polymeric and composite systems have been utilized as high refractive index materials in optical applications[9, 10], the high molar refraction of sulfur-containing polymers and the inherent high sulfur content of thiol-ene polymer networks suggests thiol-ene photopolymerizations may provide unique advantages to the development of high refractive index materials. Thiol-ene photopolymerizations are characterized by rapid and oxygen insensitive reactions, homogenous network structures, low shrinkage, and both spatial and temporal control over polymerization – ideal properties for the synthesis of polymeric thin films. These advantages have been utilized in the synthesis of high refractive index thiol-ene monoliths[11] and gradient refractive index thiol-ene materials[12], but the refractive index remains low (<1.7) when considering use in semiconducting optoelectronics. Traditionally, organic/inorganic hybrid materials have been utilized to impart the advantages of an organic phase (flexibility, toughness) with the high refractive index of an inorganic phase (amorphous TiO_2, n ~2.5).[9, 13-15] Therefore, we investigated the use of thiol-ene/amorphous TiO_2 composite thin films as a

112

means to develop tunable high refractive index materials with high optical transparency and stability.

A.3 Experimental

A.3.1 Materials

All reagents and solvents were obtained from Fisher Scientific in the highest purity unless specified otherwise. Pentaerythritol triallyl ether (APE) and titanium isopropoxide (TIP) were obtained from Sigma Aldrich, trimethylolpropane tris(3-mercaptopropionate) (TMPMP) was obtained from Bruno Bock, pentaerythritol triacrylate (SR-444) was obtained from Sartomer, and Darocur 1173 was obtained from BASF.

A.3.2 Thiol-ene/TiO$_2$ Hybrid Thin Film Synthesis

Synthetic conditions reported below are the result of optimized reaction and processing conditions. To 20 mL of isopropyl alcohol, 100.0 mg TMPMP, 64.3 mg APE, and 2 wt.% Darocur 1173 (relative to organic) were added and homogenized (1:1 SH:ene mol ratio) under rapid stirring. Water, concentrated HCl, and titanium isopropoxide were then added, in that order, in the following ratios: H$_2$O:TIP – 1:1 mol equiv., HCl:TIP – 1:30 mol equiv, and TIP was added, dropwise, at 25, 35, 50, 65, 75, and 85 wt.%, with the wt.% calculated such that the total mass of TIP and thiol-ene would equal 100 wt.%. Sol-gel mixtures were then stirred rapidly until homogenous, and passed through a 0.45 μm PTFE filter onto plasma cleaned glass and silicon substrates for spin coating at 5,000 rpm for 60 seconds. The resulting thin films were then exposed to 15 mW/cm^2 broadband UV light for 5 minutes.

113

A.3.3 Thermal Treatment

Hybrid thin films synthesized in **A.3.2** were thermally treated under dry and humid conditions by placing the spin coated films in an oven at 45 °C and 105 °C. Humid conditions were prepared by placing the films in a jar with a vent containing a reservoir of 5 mL DI H_2O. Samples were monitored over several hours to find the optimized thermal treatment conditions.

A.3.4 Aged Thiol-Ene/TiO$_2$ Thin Film Synthesis

To generate thicker films, an ageing process was applied to the sol-gel synthesis. Samples were prepared similar to **A.3.2**, however, 10 mL isobutyl alcohol was used as solvent, and the H_2O:TIP, and HCl:TIP mol ratios were changed to 3:1 and 1:10, respectively. Samples were then stirred at room temperature for 0 to 72 hours and films were prepared as previously described.

A.3.5 Characterization

Refractive index measurements were calculated on Gaertner Scientific Corporation LSE ellipsometer with a 632.8 nm laser at 70° from the normal. Transmittance spectra were collected using a Lambda 35 UV-Vis Spectrometer where the thin films, spin coated onto glass, were placed directly in the light pathway. Transmittance values were measured at a wavelength range of 350 -700 nm. Thin film morphology was determined via atomic force microscopy using a Bruker Icon in tapping mode. Samples were scanned with a T300R-25 probe with a spring constant of 40 Nm^{-1}.….

A.4 Results and Discussion

A.4.1 Hybrid Thin Film Formation
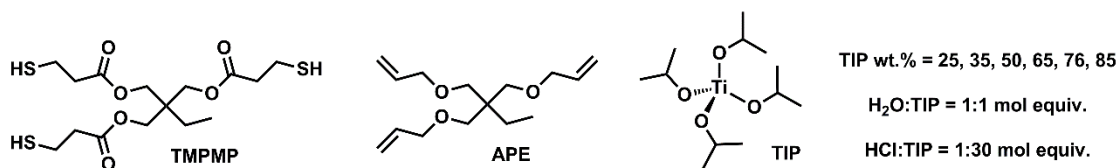
Figure A.1 Thiol-ene monomers, TiO$_2$ precursor, and formulation conditions used to synthesize high refractive index hybrid thin films.

The sol-gel synthesis of thiol-ene/TiO$_2$ hybrid thin films required considerable amounts of optimization. Solvent choice and the appropriate ratios of water and HCl, are crucial parameters dictating the rate of the TiO$_2$ condensation reaction and the quality of the resulting thin films. After considerable experimentation, the desired ratios (provided in section **A.3.2**) were found and thin films were synthesized using the network materials shown in Figure A.1, by spin coating the thiol-ene/TiO$_2$ sol-gel solutions at 5,000 rpm, followed by a 5 minute UV photopolymerization of the thiol-ene monomers. The resulting films were approximately 20 nm thick and showed an increase in refractive index with increasing TIP loading (Table A.1). From the results presented in Table A.1, it is clear that by varying the amount of TIP in the system, the refractive index of the film can be systematically controlled and high refractive index values are achievable (i.e. 85 wt.% TIP, $n = 1.79$). Further, the hybrid high refractive index thin films were synthesized via a one pot method, using mild processing conditions. These results

Table A.1

Refractive Index of Thiol-ene/TiO$_2$ Thin Films Without Thermal Treatment

TIP wt.%	25	35	50	65	75	85
n	1.65	1.66	1.69	1.70	1.75	1.79
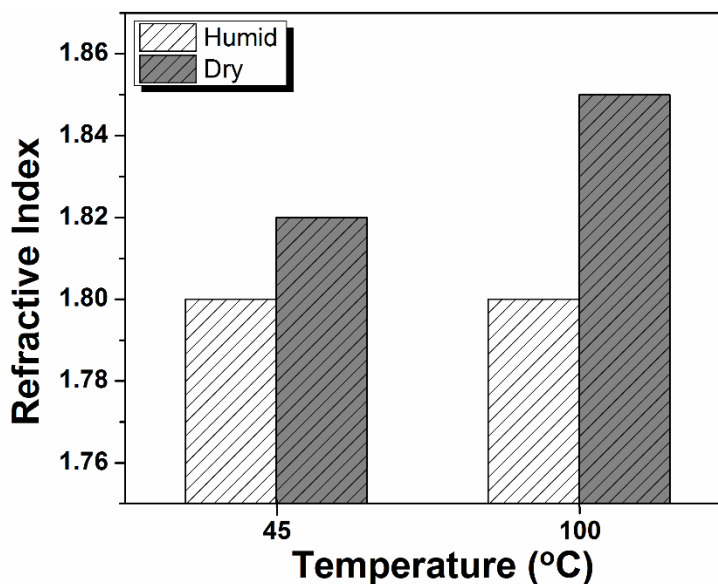
Figure A.2 Refractive index of 85 wt.% TiO_2/thiol-ene hybrid thin film under varying thermal treatment conditions.

indicate that this methodology allows the facile and rapid synthesis of high refractive index coatings, and may be useful in a variety of industrial settings

To drive the TiO_2 condensation reaction to higher conversions, thus increasing the thin film refractive index, thermal treatment was applied to the organic/inorganic hybrid films; a common methodology in sol-gel film preparation.[16] Thermal treatment was conducted at 45 °C and 105 °C under both dry and humid conditions for an 85 wt.% TiO_2 hybrid thin film. Humid conditions were tested as inorganic sol-gel films are brittle and have been demonstrated to crack at high network conversions.[17] As shown in Figure A.2, the refractive index is increased from 1.79 to 1.82 and 1.85 under dry conditions at 45 °C and 105 °C, respectively. Under humid conditions, an increase in refractive index is observed, but temperature displayed no measureable effect (1.81 and 1.81 for 45 °C and 105 °C, respectively). The increased refractive index under dry conditions, and more significantly, under high temperature conditions, is rationalized by the successful

116
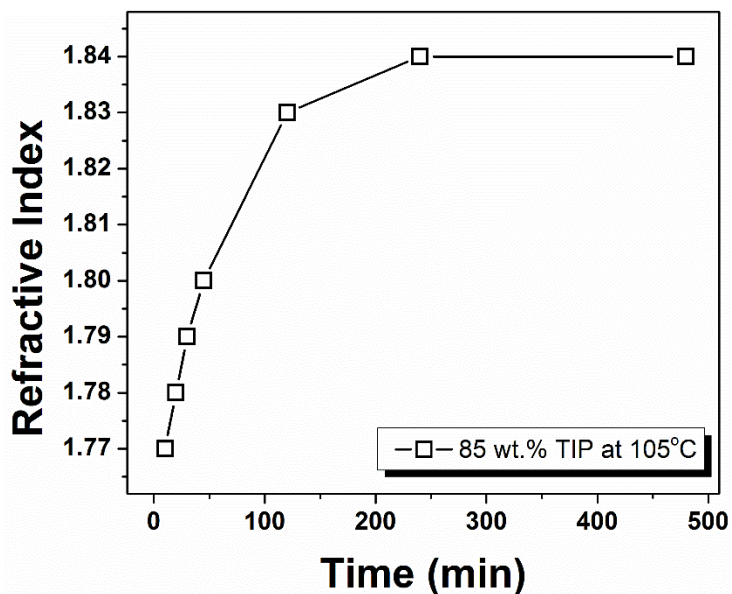
Figure A.3 Refractive index vs time for an 85 wt.% TiO_2 hybrid film thermally treated at 105 °C in a dry atmosphere. Results indicate that an optimal refractive index is achieved after 4 hours.

evaporation of water from the thin film. As TiO_2 network formation is a condensation reaction, the byproduct (water) must be driven off to achieve high conversion. Under humid conditions, it is probable that the film environment becomes saturated with water, preventing high network conversion and therefore high refractive index films.

Thermal treatment was subsequently investigated as a function of time in order to determine the conditions required to achieve the highest refractive index film. As the 105 °C dry thermal condition showed the most promise for achieving a high refractive index, all subsequent experimentation was conducted at this thermal treatment condition. Figure A.3 shows the change in refractive index of an 85 wt.% TiO_2 hybrid film over 500 minutes. During the initial thermal treatment time, a linear rise in refractive index is observed (from 1.77 to 1.80 after 45 minutes). At extended times, a plateau begins to appear (120 minutes, $n = 1.83$) until the film reaches its final refractive index value at 240

117
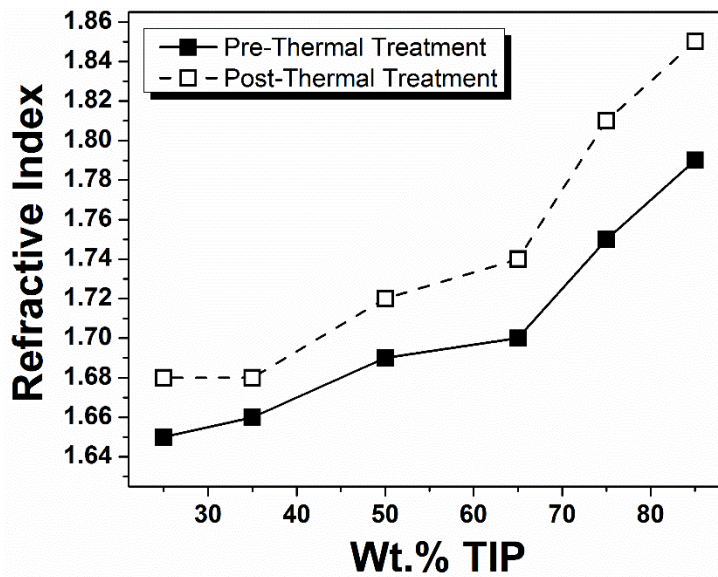
Figure A.4 Refractive index of 25 – 85wt.% TiO₂ hybrid films before thermal treatment (closed symbols) and after 4 hours of a 105 °C dry thermal treatment (open symbols).

Table A.2

Refractive Index of Thiol-ene/TiO₂ Thin Films With 105 °C DryThermal Treatment

TIP wt.%	25	35	50	65	75	85
n	1.68	1.68	1.72	1.74	1.81	1.85

minutes ($n = 1.85$). Additional thermal treatment resulted in no further increases in refractive index. From these results, it is concluded that for the thiol-ene/TiO₂ hybrid films, an optimal refractive index can be achieved after 4 hours of thermal treatment at 105 °C in a dry atmosphere. As such, all films (25 – 85 wt.% TiO₂) were subjected to the previously described thermal treatment and the resulting refractive indices are shown in Figure A.4 and summarized in Table A.2. As expected, thermal treatment increased the refractive index for all films, with the largest increase occurring in films containing the highest wt.% TiO₂ (65 -85 %).
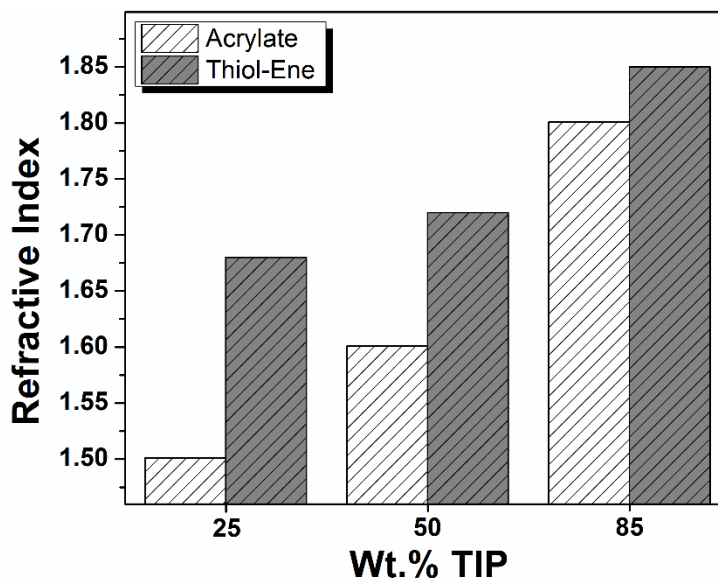
Figure A.5 Refractive index comparison of the TiO$_2$ hybrid films containing an acrylate or thiol-ene based organic phase. Films prepared at optimized thermal treatment conditions.

In order to elucidate the influence of the thiol-ene polymer network on refractive index, a series of thin-films were prepared as previously described at 25, 50, and 85 wt.% inorganic material, using a trifunctional acrylate (SR-444, pentaerythritol triacrylate) in place of the thiol-ene monomers. A comparison of the refractive index of the acrylate and thiol-ene containing films is shown in Figure A.5. As observed, the refractive index of the thiol-ene films is greater than that of the acrylate films at all wt.% TIP loading (1.50 vs 1.68 for 25 wt.%, 1.60 vs 1.72 for 50 wt.%, and 1.80 vs 1.85 for 85 wt.%). The increased refractive index of the thiol-ene films is rationalized by the high sulfur content inherent in the thiol-ene polymer network, and demonstrates the synergy between the organic and inorganic material at increasing the refractive index of the hybrid thin films.

With the ability to prepare high refractive index films, we sought to investigate their utility in optical applications. Ideally, the hybrid films would have a high
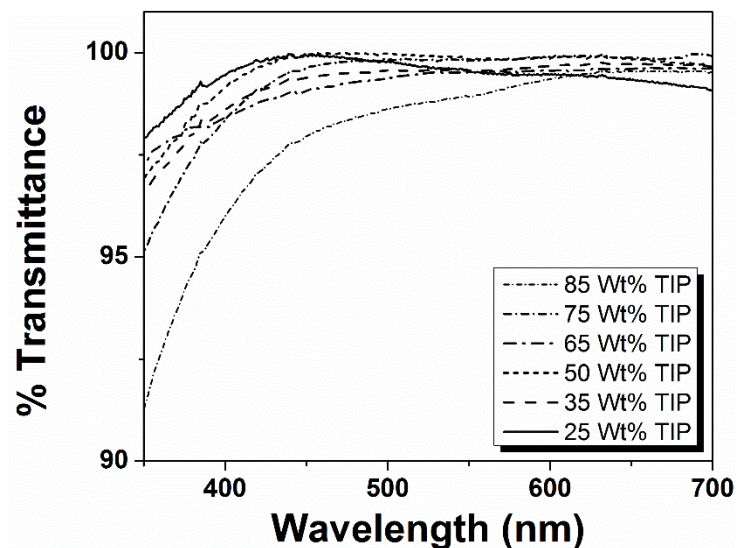
Figure A.6 UV-Vis transmittance spectra of 25 – 85 wt.% TIP/thiol-ene films. Films show high optical transparency over most of the visible light region.

transparency for visible light – a desired property in displays and lenses. To investigate, thiol-ene/TiO_2 hybrid films (25 – 85 wt.%) were spun onto glass substrates and transmittance spectra were recorded over the visible light range. The results are shown in Figure A.6. The 25 to 75 wt.% films all show similar trends, with transmittance values of ~ 98 - 99% from 700 to 400 nm, though small decreases in transmittance are observed with increasing TiO_2 content. The 85 wt.% film shows a more pronounced decrease in transmittance across the same wavelength range, but still maintains a transmittance of ≥ 95% until 400 nm. At 400 nm, a pronounced downward turn in transmittance is observed for all samples as glass begins to absorb light in this wavelength region.

Finally, the morphology of the hybrid thin films was obtained through AFM in tapping mode in order to ensure a homogenous surface structure was realized, avoiding any defects that may be detrimental to the thin film's optical properties. The morphology of an 85 wt.% TiO_2 thin film is shown in Figure A7. At larger length scales (Figure A7a, 20 μm x 20 μm) a smooth morphology is observed, with a root mean squared (rms)
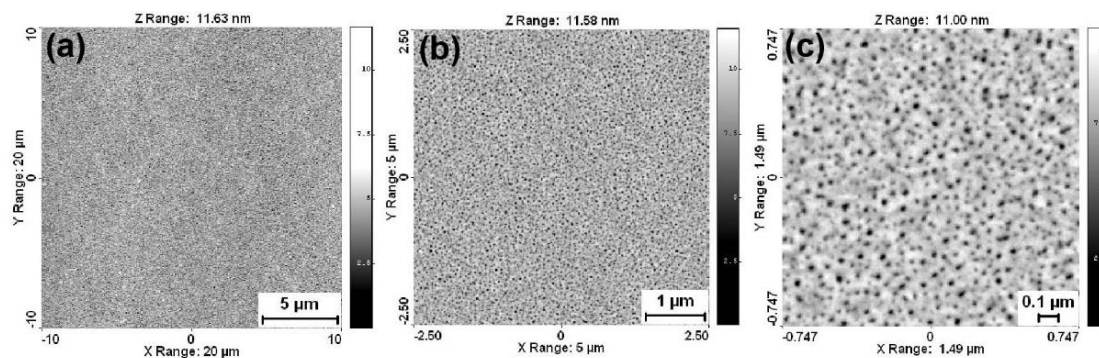
Figure A.7 AFM images of an 85 wt.% TiO$_2$/thiol-ene hybrid thin film at various length scales collected in tapping mode (a) 20 x 20 μm (b) 5 x 5 μm (c) 1.50 x 1.50 μm.

roughness of 0.710 nm. However, observing the film surface at smaller length scales (Figure A7, (a) and (b)) revealed the presence of ~5-25 nm sized "pinhole" defects (the calculated roughness remained same). Pinholes are a common defect observed in spin coating and have been demonstrated to be sensitive to the presence of very fine substrate contaminants.[18] Although the substrates were plasma treated to avoid defect surfaces, it is possible that prior to use additional contaminants (i.e. dust) landed on the substrate surface. As the hybrid films are very thin (~20 nm), even light contamination of the substrate may cause observable defects in morphology.[18] Ultimately, the thin nature of the film is problematic due to both the heterogeneous morphology, and the fact that optical devices such as OLEDs often require layers of considerable thickness, far greater than the 20 nm reported for the films above. Under the current conditions for hybrid film preparation, thick and uniform films were difficult to synthesize. Therefore, sol-gel preparation conditions were adjusted to facilitate an increased ageing of the sol and the results are described below.

A.4.2 Aged Sol-Gel Films and Hybrid Film Morphology

In order to synthesize high refractive index films with increased thickness, the thiol-ene/TiO_2 solutions were subjected to an "aging" process. The aging process allows the TiO_2 condensation reaction to proceed to a conversion such that the viscosity, and therefore the spin coating behavior, facilitates the formation of thick, homogeneous films. Under the conditions reported in **A.3.2**, aging of the films led to uncontrolled generation of the sol-gel, resulting in particulate formation and/or gelation in short reaction times. To slow the reaction down and allow a more homogeneous sol-gel to form, the solvent was switched from isopropanol to isobutanol, and the solvent, water, and acid concentrations were adjusted. It is rationalized that the use of isobutanol retards sol-gel formation by replacing the more reactive isopropoxide groups of TIP with isobutoxide groups via an alcohol exchange reaction.[19] Following optimization of the synthetic conditions, an 85 wt.% TIP solution was prepared and aged for 0, 16, and 48 hours. The resulting films showed an increase in thickness compared to the IPA based films, with thickness increasing to 80 nm, 110 nm, and 180 nm for a 0 hour,16 hour, and 48 hour age time, respectively. While these results demonstrate that an increased thickness could be achieved utilizing an aged sol-gel, unfortunately, homogeneous films could not be prepared at a thickness greater than 200 nm.

Although large film thicknesses (hundreds of nanometers) could not be achieved under the described synthetic conditions, AFM revealed that increases in thickness to ~100 nm in the 85 wt.% TiO_2 film eliminates the pinhole defects observed in the IPA-based films. As shown in Figure A8a, at 0 hours of age time (80 nm thick film) the
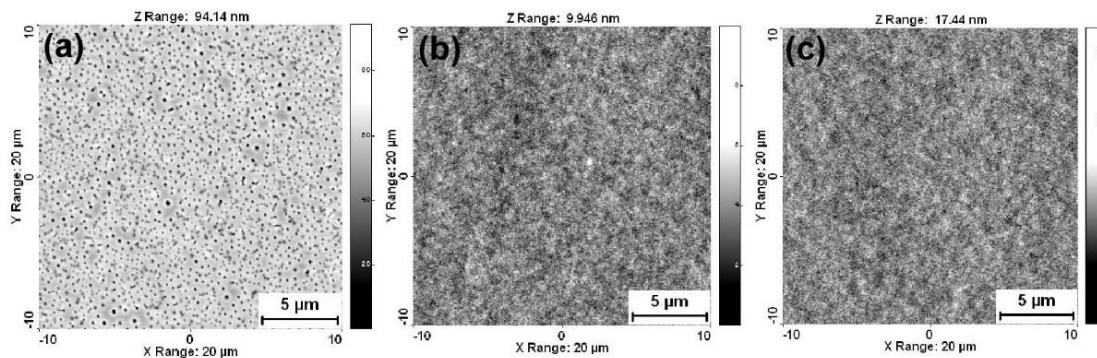
Figure A.8 AFM images of 85 wt.% thiol-ene/TiO$_2$ hybrid thin films aged (a) 0 hours (b) 16 hours (c) 48 hours.

pinhole morphology is still observed and occurs at a larger length scale (hole size ~ 20 nm – 500 nm), resulting in an increased rms roughness (8.00 nm). However, aging of the films increased film thickness and a smooth morphology is observed for both the 16 hour aged filmed (Figure A8b, rms roughness = 0.76 nm) and the 48 hour aged film (Figure A8c, rms roughness = 0.91 nm).

Following the success of developing a smooth morphology in the 85 wt.% TiO$_2$ hybrid film, 50, 65, and 75 wt.% films were synthesized and aged from 0-72 hours (aging of the 25 wt.% and 35 wt.% TIP solutions did not result in the necessary increases in viscosity required to form a thicker film). Surprisingly, the morphology observed in the 50-75 wt.% films was considerably heterogeneous. As shown in Figure A9, the 50 wt.% film revealed the formation of a particle-like morphology, where the 65 wt.% and 75 wt.% films showed significant hole formation. The images shown in Figure A9 are representative of the 50-75 wt.% films at all aging times. As the films show similar thickness to that observed for the 85 wt.% film aged at 16 hr and 48 hr, the resulting morphology is likely not the result of contamination alone. While the morphological
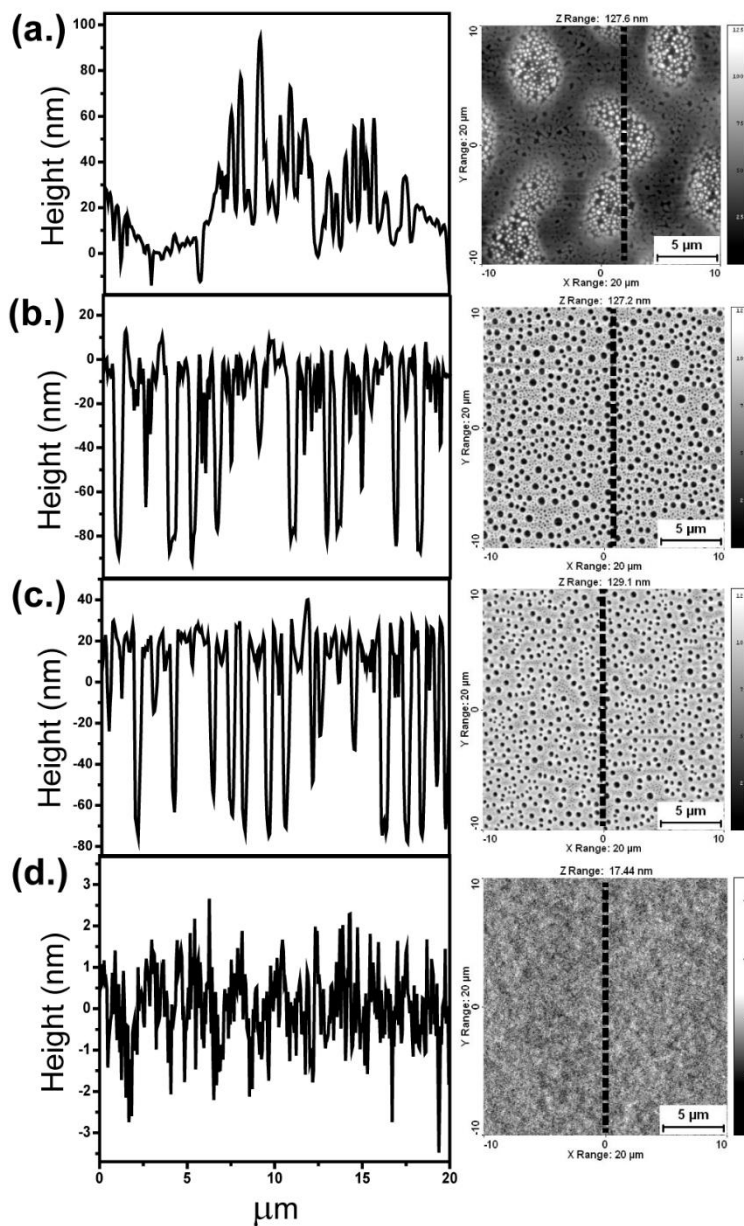
Figure A.9 Normalized cross section profiles and representative morphology images of aged hybrid films (a) 50 wt.% TiO_2 (b) 65 wt.% TiO_2 (c) 75 wt.% TiO_2 (d) 85 wt.% TiO_2. Dotted line represents the measured cross sections.

results presented in Figure A9 are not fully understood, it is suspected that the decreased

solubility of water in the isobutanol solutions may result in phase separation behavior

during spin coating and film formation. Water, while miscible in isobutanol (IBA),

showed marked decreases in solubility in IBA compared to IPA (IBA solutions took

124

several minutes to homogenize compared to the immediate homogenization of the IPA solutions). Therefore, it is hypothesized that during spin coating, as isobutanol evaporates, the concentration of residual water suddenly and sharply increases and phase separates into nanoscale droplets. As neither the inorganic TiO_2 phase nor the organic thiol-ene monomers are soluble in water, the droplet creates a hole on the surface of the film, showing depths of approximately 80 nm (Figure A9 (b) and (c)). From Figure A8 and A9d, it is demonstrated that at appreciable age times the 85 wt.% hybrid films do not display the hypothesized phase separation behavior. It is rationalized that due to higher concentrations of TIP in the 85 wt.% solution, at a given age time, the inorganic condensation reaction in the 85 wt.% solution has reached a more complete network structure when compared to the lower weight percentage solutions. Subsequently, during spin coating, the inorganic network has converted to such an extent that any phase separation behavior is resisted. Currently, the most convincing piece of evidence for this conclusion is based on Figure A8, where it was demonstrated that for an 85 wt.% hybrid film spun without aging, a hole morphology was observed. For the same wt.% solution, when subjected to either a 16 hour or 48 hour age, the TiO_2 network has reached higher conversions (increased viscosity) and a smooth film morphology is realized. The morphology of the 50 wt.% film is more convoluted as both hole and particle formation is observed. This result is a likely combination of miscibility, reaction conversion, and concentration, and as such, requires additional investigation to be fully understood.

Though the morphology results for the aged hybrid films are not ideal for optical applications (with the exception of the 85 wt.% films), the potential ability to dictate
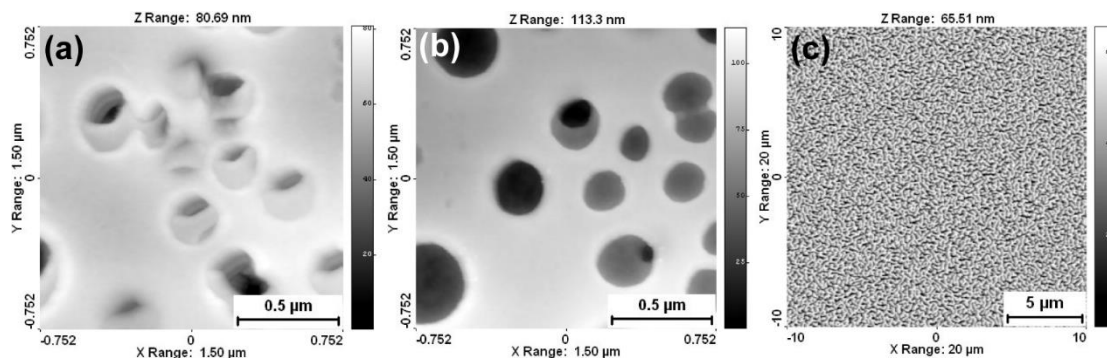
Figure A.10 (a) and (b) Porous morphology of an unaged 85 wt.% TiO$_2$ hybrid film prepared from an IBA solution showing depth and layering in porous structure (c) Phase separate structure of a 65 wt.% TiO$_2$ hybrid film aged for 24 hours – holes have become interconnected. .

surface morphology simply from processing conditions may have promise in other a

applications. Specifically, TiO$_2$ networks are known to display photocatalytic activity

and photoresponsive switching in wettability when exposed to UV and visible light.[20-23]

As these concepts are beyond the scope of this Appendix, they will not be discussed in

depth, however it is worth noting that the magnitude of catalytic activity and

switchability are related to the surface area of the film. Within this context, Figure A10

shows some of the interesting morphology patterns that may be achieved through simple

alteration of the formulation and spin-coating conditions for the thiol-ene/TiO$_2$ hybrid

films. As stated previously, the ability to truly control these morphologies under the

described processing conditions has yet to be fully understood, however, the unique

patterns and structures formed may one day be applicable for responsive surfaces (i.e.

self-cleaning).

A.5 Conclusions

In summary, we have demonstrated the facile synthesis of hybrid thiol-ene/TiO$_2$

thin films that demonstrate tunable and high refractive indices. Under a high

temperature, dry thermal treatment condition, refractive index values of up 1.85 were

achieved – values necessary for use in certain optical and display applications. The use

of thiol-ene chemistry, intended to stabilize the formation of thick hybrid films, showed a

synergistic increase in refractive index owing to the high sulfur content when compared

to acrylate-base films, though did not facilitate the formation of thick films. By

subjecting the films to an aging process, increases in film thickness could be achieved,

though the resulting film morphologies resulted in heterogeneities that would limit their

use in optical applications. Interestingly, the processing conditions presented suggest that

there may be a route to controlling or influencing film morphology by a fine tuning of the

formulation and spin coating conditions. The results presented in this Appendix lay the

ground work for the development of high refractive index thin films for optical

applications and, additionally, suggest that the hybrid films may show utility in

applications were a controlled topography is necessary.

A.6 References

(1). Aizenberg, J.; Hendler, G. Designing Efficient Microlens Arrays: Lessons from Nature *J. Mater. Chem.* **2004,** *14*, 2066-2072.

(2). Kang, D. J.; Bae, B.-S. Photo-Imageable Sol–Gel Hybrid Materials for Simple Fabrication of Micro-Optical Elements *Acc. Chem. Res.* **2007,** *40*, 903-912.

(3). Ma, H.; Jen, A. K. Y.; Dalton, L. R. Polymer-Based Optical Waveguides: Materials, Processing, and Devices *Adv. Mater.* **2002,** *14*, 1339-1365.

(4). Junji, K. Organic Displays *Phys. World* **1999,** *12*, 27.

(5). Mortimer, R. J.; Dyer, A. L.; Reynolds, J. R. Electrochromic Organic and Polymeric Materials for Display Applications *Displays* **2006,** *27*, 2-18.

(6). Gather, M. C.; Köhnen, A.; Meerholz, K. White Organic Light-Emitting Diodes *Adv. Mater.* **2011,** *23*, 233-248.

(7). Chen, S.; Deng, L.; Xie, J.; Peng, L.; Xie, L.; Fan, Q.; Huang, W. Recent Developments in Top-Emitting Organic Light-Emitting Diodes *Adv. Mater.* **2010,** *22*, 5227-5239.

(8). Matterson, B. J.; Lupton, J. M.; Safonov, A. F.; Salt, M. G.; Barnes, W. L.; Samuel, I. D. W. Increased Efficiency and Controlled Light Output from a Microstructured Light-Emitting Diode *Adv. Mater.* **2001,** *13*, 123-127.

(9). Liu, J.-g.; Ueda, M. High Refractive Index Polymers: Fundamental Research and Practical Applications *J. Mater. Chem.* **2009,** *19*, 8907-8919.

(10). Higashihara, T.; Ueda, M. Recent Progress in High Refractive Index Polymers *Macromolecules* **2015,** *48*, 1915-1929.

(11). Bhagat, S. D.; Chatterjee, J.; Chen, B.; Stiegman, A. E. High Refractive Index Polymers Based on Thiol–Ene Cross-Linking Using Polarizable Inorganic/Organic Monomers *Macromolecules* **2012,** *45*, 1174-1181.

(12). Meng, Y.; Tsai, M.; Schmidt, G. R.; Anthamatten, M. Gradient-Index Materials Based on Thiol–Ene Networks *ACS Appl. Mater. Interfaces* **2015,** *7*, 8601-8605.

(13). Su, H.-W.; Chen, W.-C. High Refractive Index Polyimide-Nanocrystalline-Titania Hybrid Optical Materials *J. Mater. Chem.* **2008,** *18*, 1139-1145.

(14). Kim, J.-S.; Yang, S.; Bae, B.-S. Thermally Stable Transparent Sol−Gel Based Siloxane Hybrid Material with High Refractive Index for Light Emitting Diode (Led) Encapsulation *Chem. Mater.* **2010,** *22*, 3549-3555.

(15). Wang, B.; Wilkes, G. L.; Hedrick, J. C.; Liptak, S. C.; McGrath, J. E. New High-Refractive-Index Organic/Inorganic Hybrid Materials from Sol-Gel Processing *Macromolecules* **1991,** *24*, 3449-3450.

(16). Zhang, X.; Lu, H.; Soutar, A. M.; Zeng, X. Thick Uv-Patternable Hybrid Sol-Gel Films Prepared by Spin Coating *J. Mater. Chem.* **2004,** *14*, 357-361.

(17). Brinker, C. J.; Scherer, G. W., *Sol-Gel Science: The Physics and Chemistry of Sol-Gel Processing*. Academic Press Limited: San Diego, CA, 1990.

(18). Chen, X.; Robinson, A. P. G.; Manickam, M.; Preece, J. A. Suppression of Pinhole Defects in Fullerene Molecular Electron Beam Resists *Microelectron. Eng.* **2007,** *84*, 1066-1070.

(19). Schubert, U. Chemistry and Fundamentals of the Sol–Gel Process. In *The Sol-Gel Handbook*, Wiley-VCH Verlag GmbH & Co. KGaA: 2015, 1-28.

(20). Asahi, R.; Morikawa, T.; Irie, H.; Ohwaki, T. Nitrogen-Doped Titanium Dioxide as Visible-Light-Sensitive Photocatalyst: Designs, Developments, and Prospects *Chem. Rev.* **2014,** *114*, 9824-9852.

(21). Bourikas, K.; Kordulis, C.; Lycourghiotis, A. Titanium Dioxide (Anatase and Rutile): Surface Chemistry, Liquid–Solid Interface Chemistry, and Scientific Synthesis of Supported Catalysts *Chem. Rev.* **2014,** *114*, 9754-9823.

(22). Nishimoto, S.; Becchaku, M.; Kameshima, Y.; Shirosaki, Y.; Hayakawa, S.; Osaka, A.; Miyake, M. Tio2-Based Superhydrophobic–Superhydrophilic Pattern with an Extremely High Wettability Contrast *Thin Solid Films* **2014,** *558*, 221-226.

(23). Gao, Y.; Masuda, Y.; Koumoto, K. Light-Excited Superhydrophilicity of Amorphous Tio2 Thin Films Deposited in an Aqueous Peroxotitanate Solution *Langmuir* **2004,** *20*, 3188-3194.
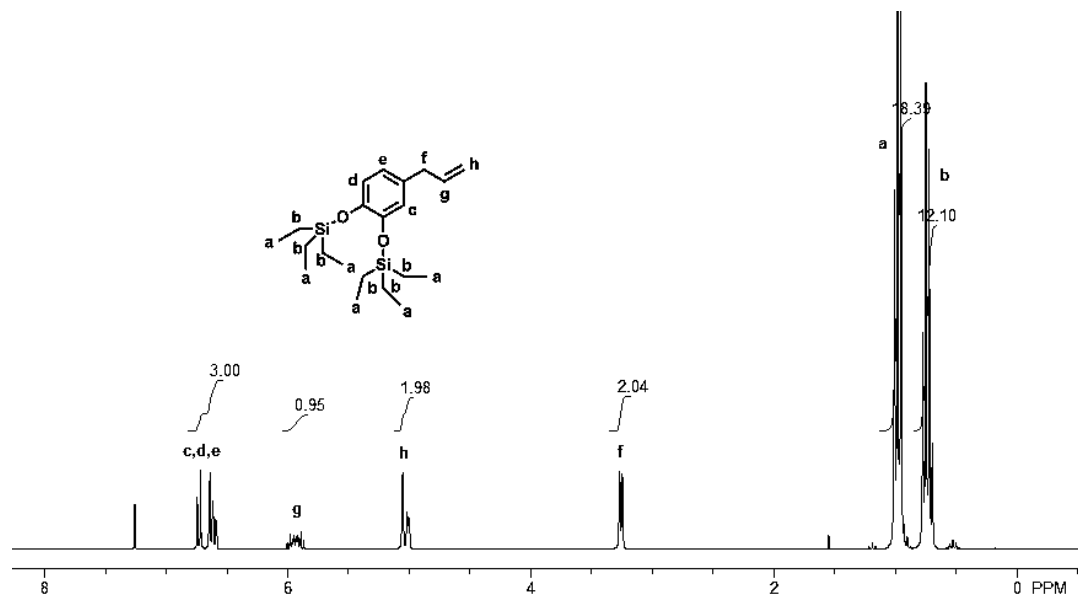
Figure B.1 ^{1}H NMR spectrum of EugTES.

Molecule hydrogens and corresponding chemical shifts denoted by letters **a-h**.
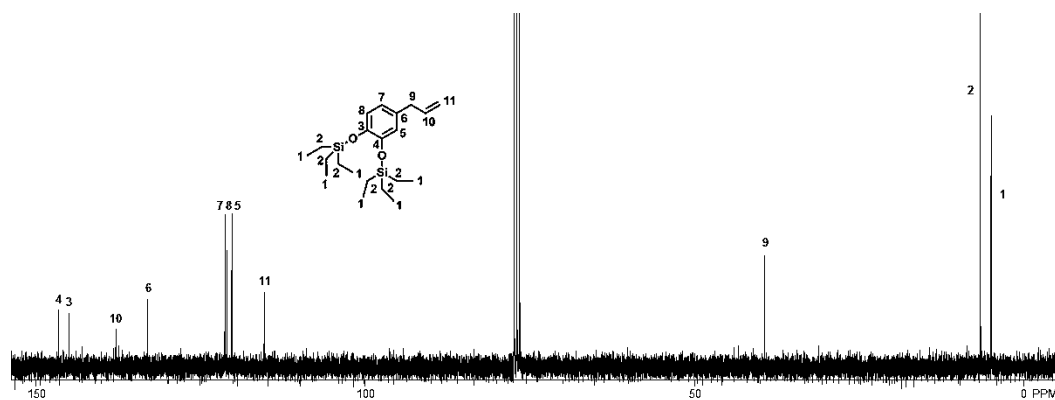
Figure B.2 ^{13}C NMR spectrum of EugTES.

Molecule carbons and corresponding chemical shifts denoted by numbers **1-11**.
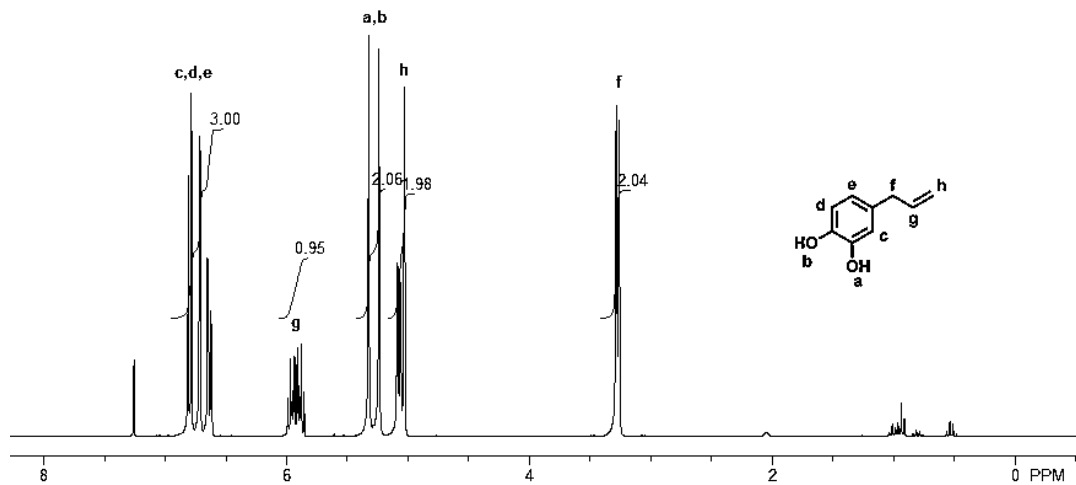
Figure B.3 ¹H NMR spectrum of EugOH.

Molecule hydrogens and corresponding chemical shifts denoted by letters **a-h**.
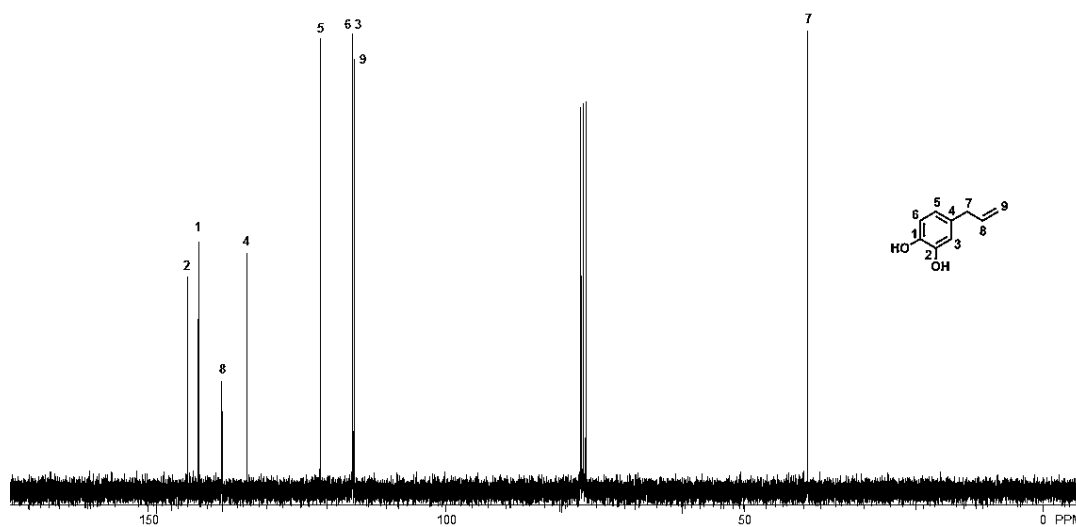
Figure B.4 ¹³C NMR spectrum of EugOH.

Molecule carbons and corresponding chemical shifts denoted by numbers **1-9**.

132
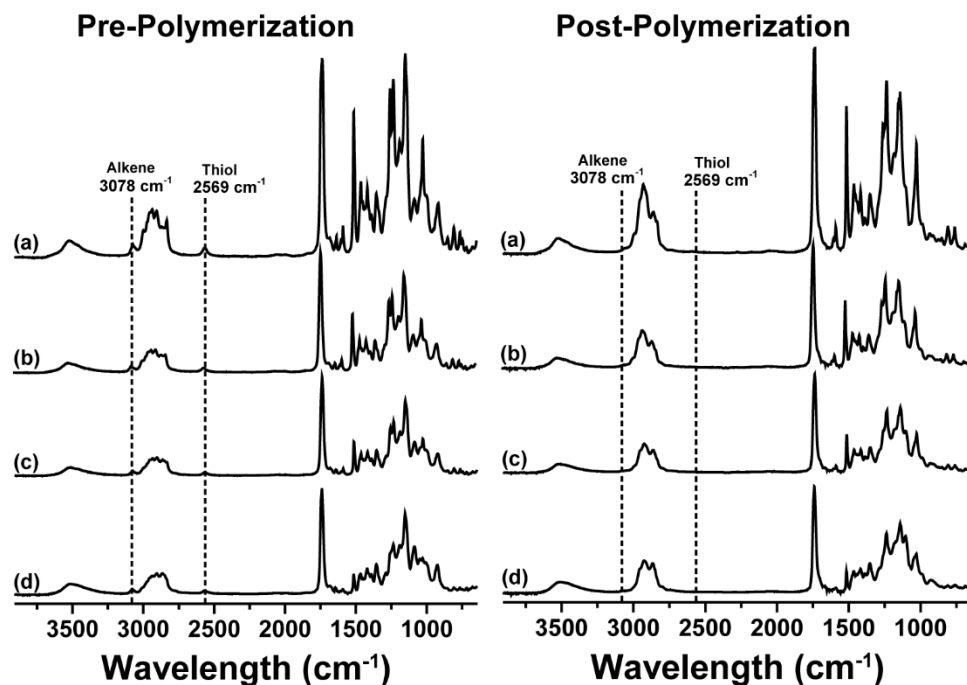
Figure B.5 FTIR of unpolymerized MeEug-APE-PETMP monomer resins (left) and FTIR of polymerized EugOH-APE-PETMP ternary polymer networks (right). (a) 50% MeEug (b) 35% MeEug (c) 25% MeEug (d) 10% MeEug.
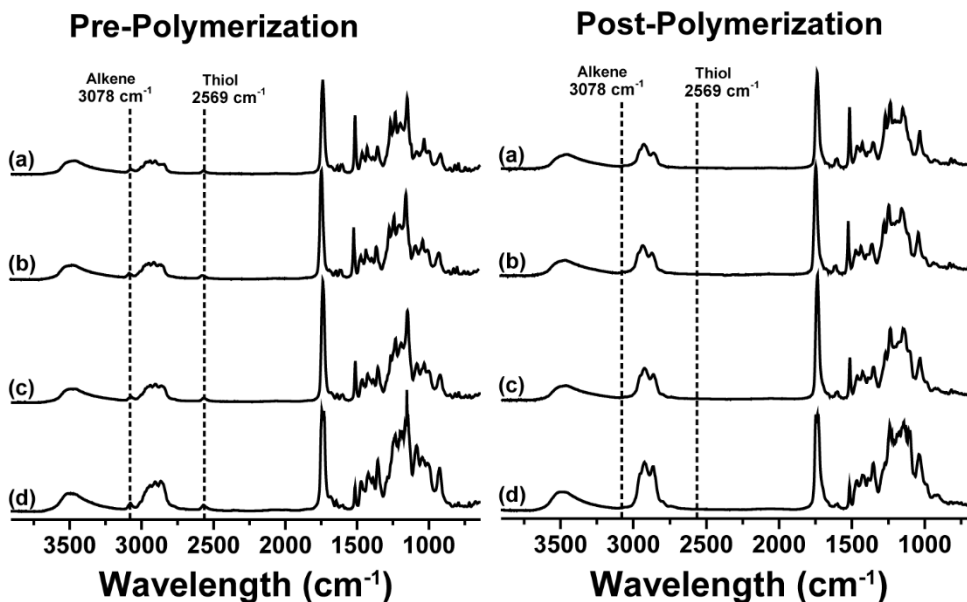
Figure B.6 FTIR of unpolymerized Eug-APE-PETMP monomer resins (left) and FTIR of polymerized Eug-APE-PETMP ternary polymer networks (right). (a) 50% Eug (b) 35% Eug (c) 25% Eug (d) 10% Eug.
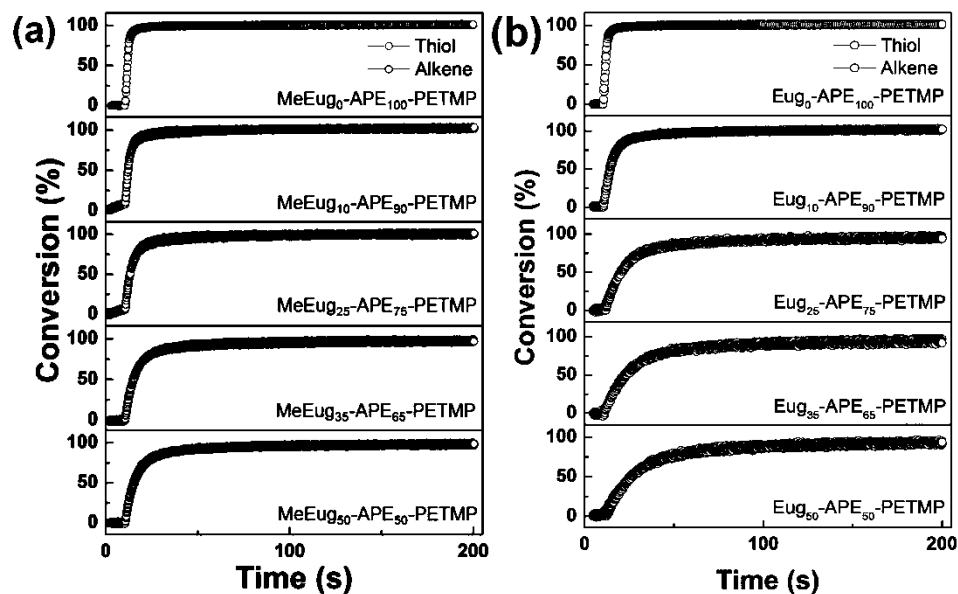
Figure B.7 (a) Kinetic plots of conversion vs time for MeEug-APE-PETMP thiol-ene networks. (b) Kinetic plots of conversion vs time for Eug-APE-PETMP thiol-ene networks.
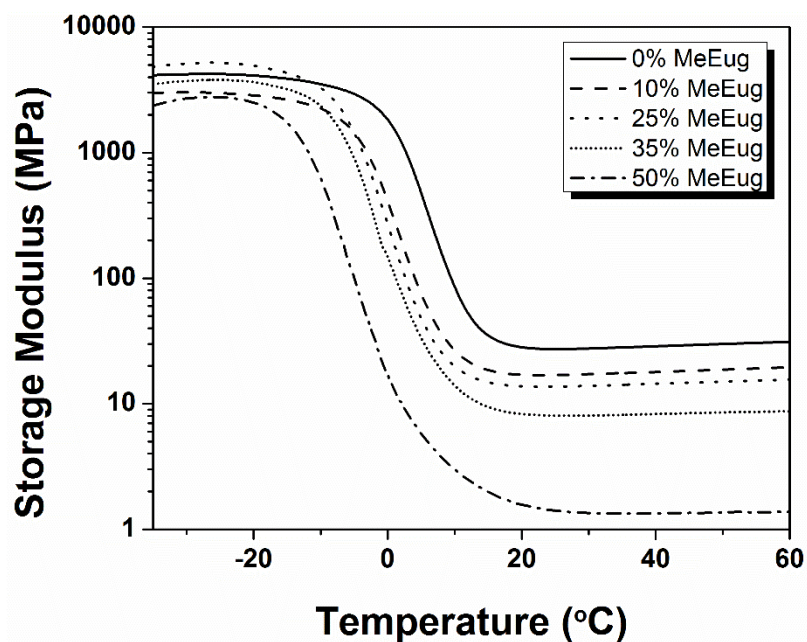
Figure B.8 Storage modulus vs temperature for the MeEug-APE-PETMP polymer networks with varying concentrations of MeEug (0-50 mol %).

134
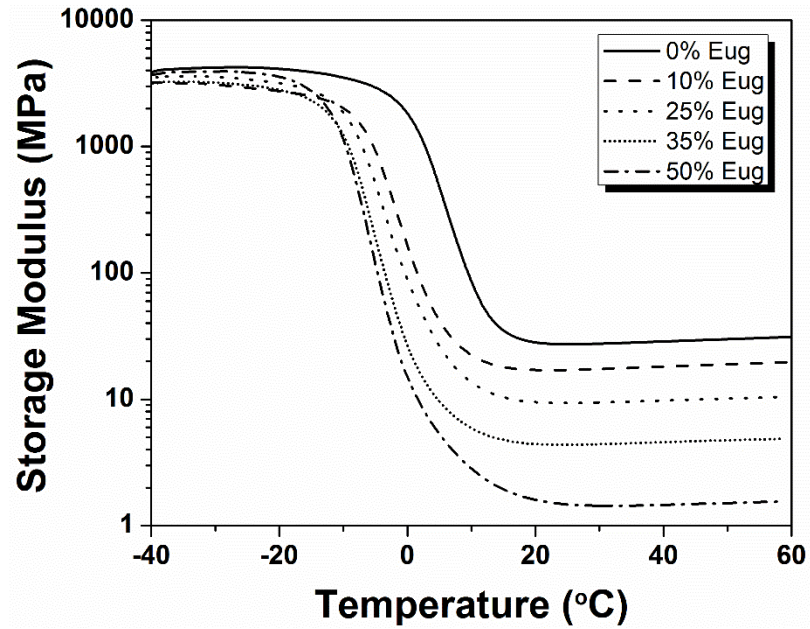
Figure B.9 Storage modulus vs temperature for the Eug-APE-PETMP polymer networks with varying concentrations of Eug (0-50 mol %).
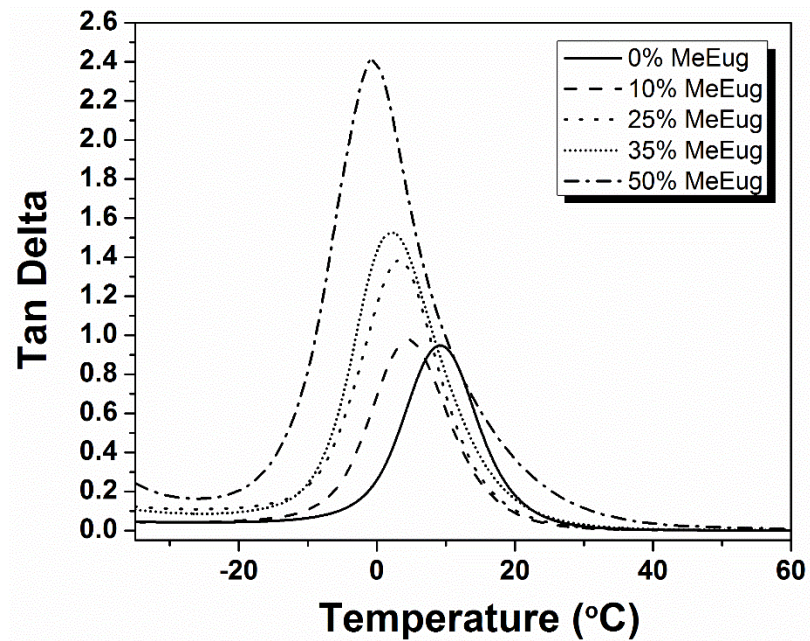
Figure B.10 Tan δ vs temperature for the MeEug-APE-PETMP polymer networks with varying concentrations of MeEug (0-50 mol %).
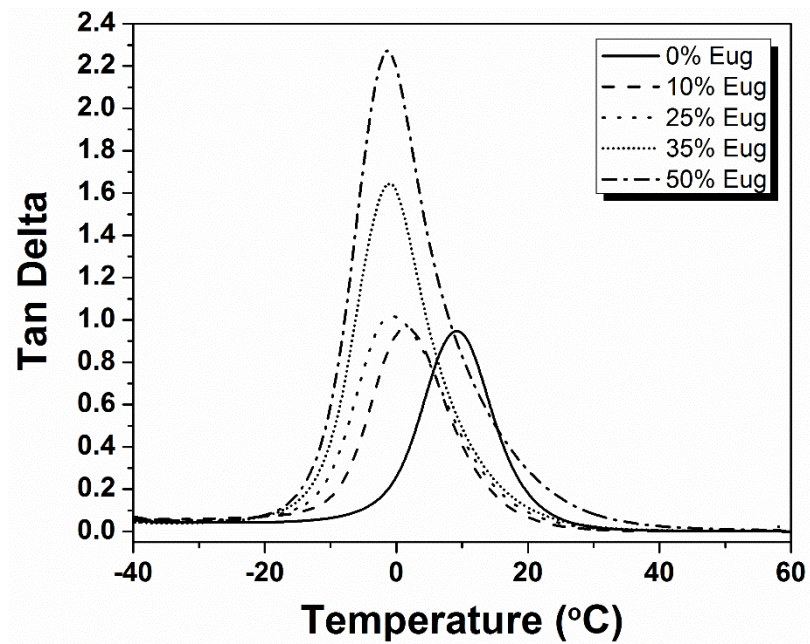
Figure B.11 Tan δ vs temperature for the Eug-APE-PETMP polymer networks with varying concentrations of Eug (0-50 mol %)
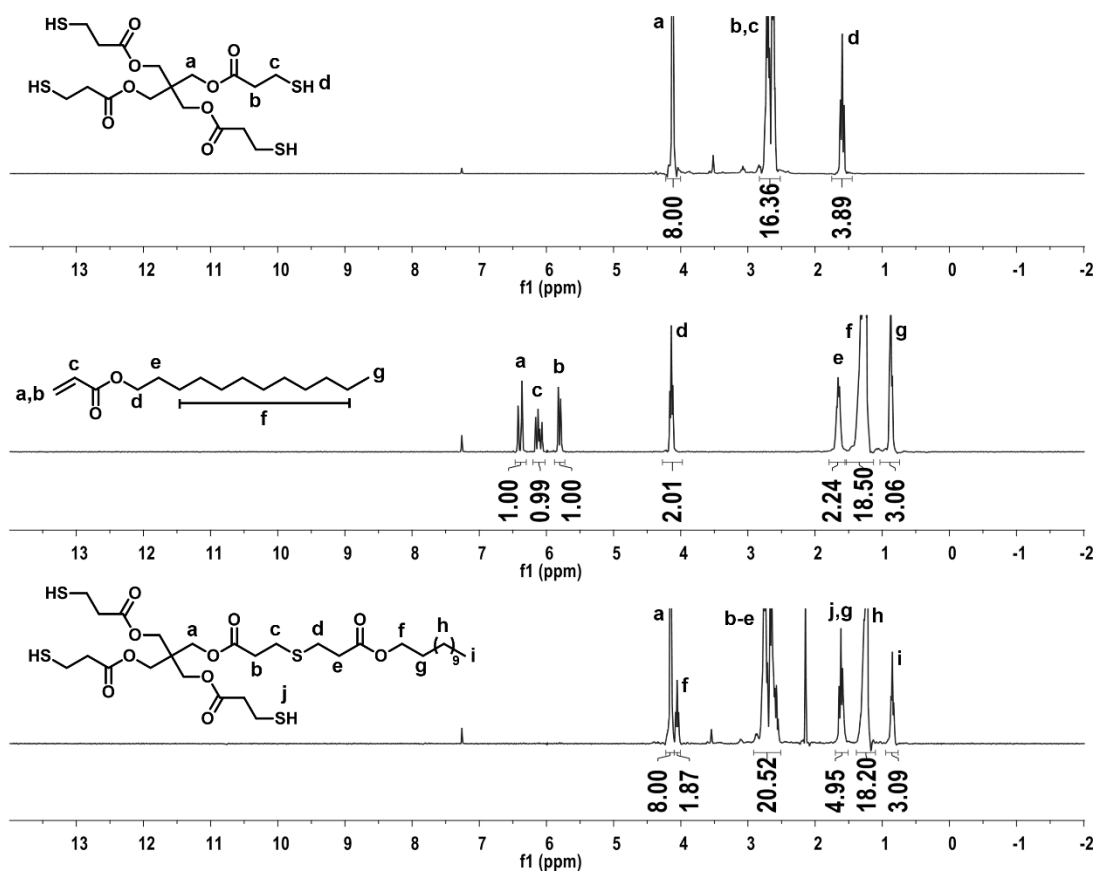
Figure C.1 ^{1}H NMR spectra of precursors and product for lauryl-PETMP synthesis.
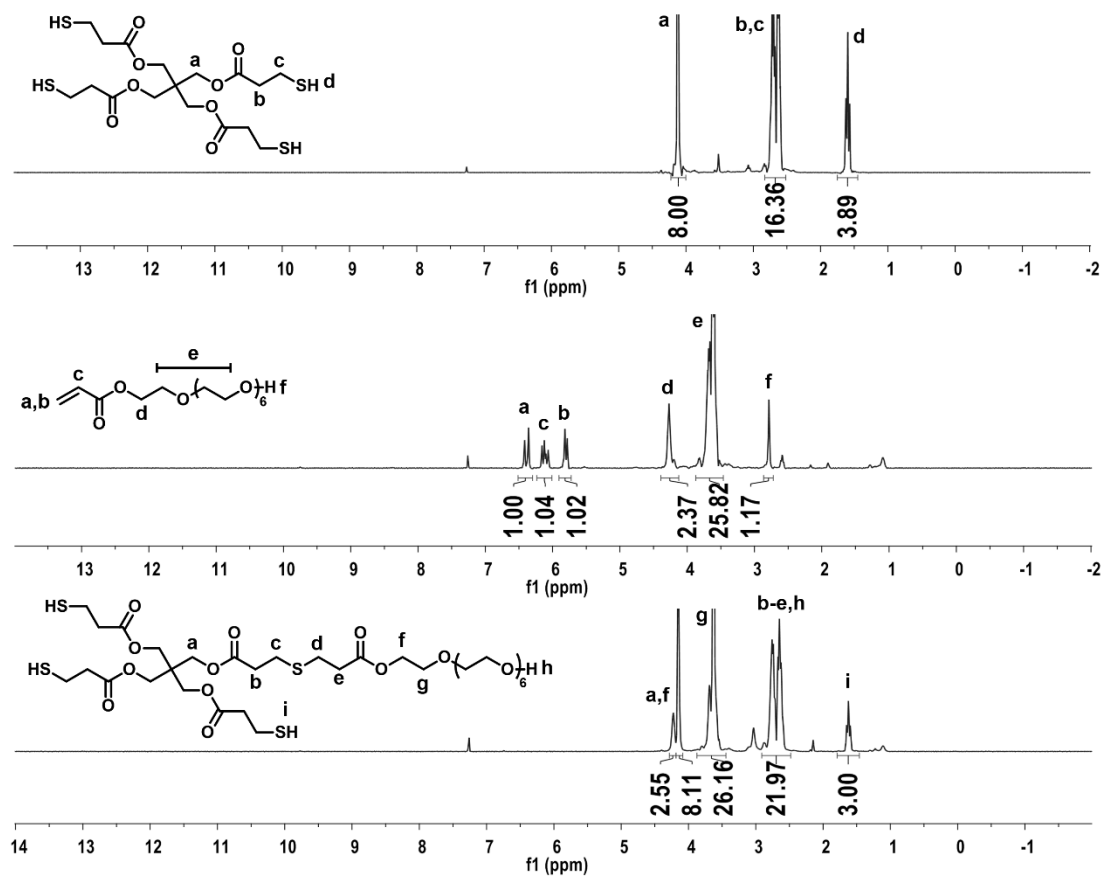
Figure C.2 ^{1}H NMR spectra of precursors and product for PEG-PETMP synthesis.

138
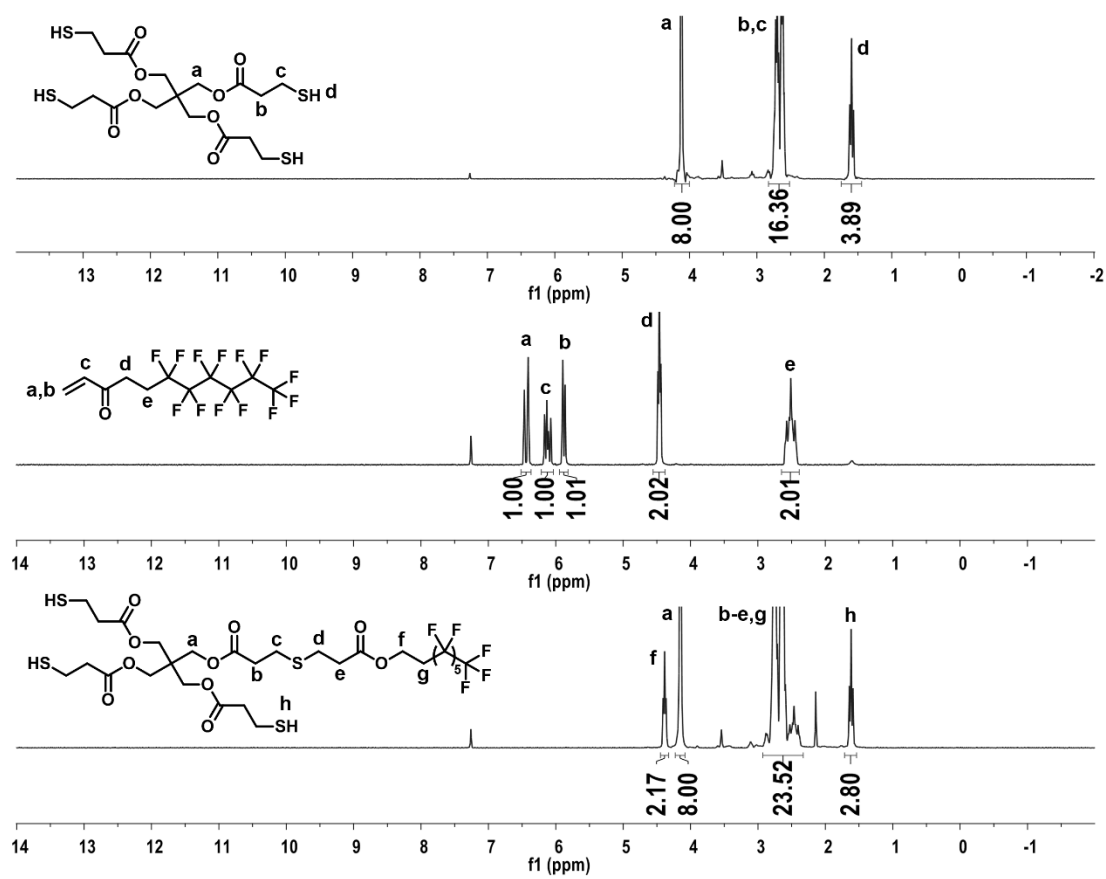
Figure C.3 ¹H NMR spectra of precursors and product for F6-PETMP synthesis
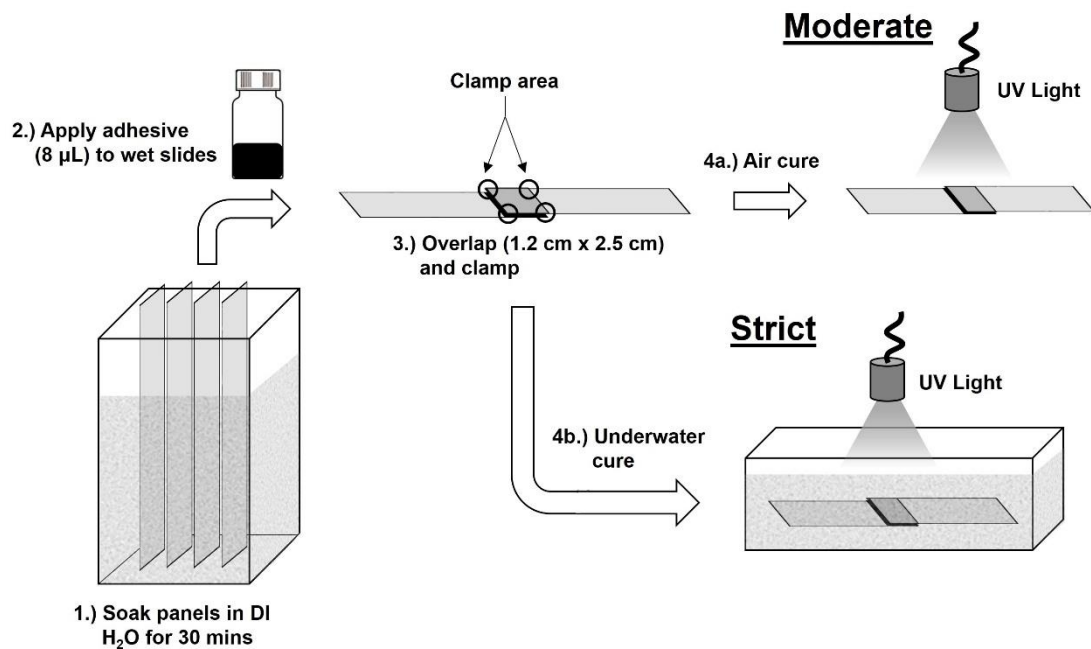
Figure C.4 Lap shear sample preparation for strict and moderate aqueous conditions. Strict conditions utilize plasma cleaned glass slides that are superhydrophilic, moderate conditions utilize glass slides with no pre-treatment.
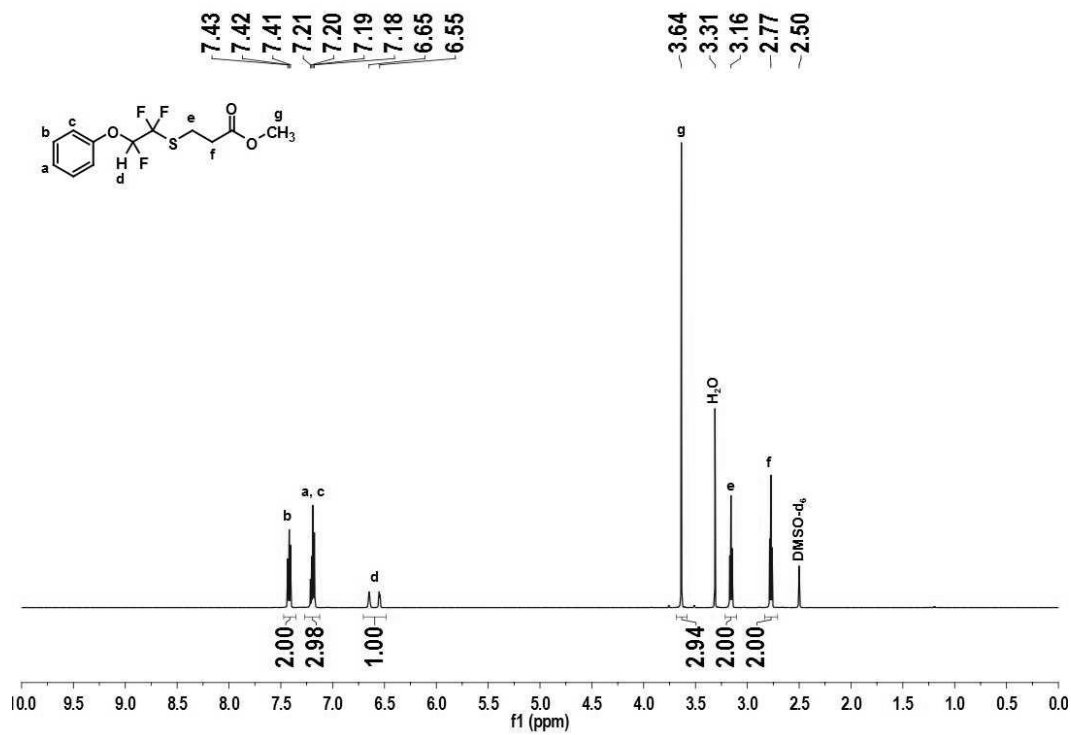
Figure D.1 ^{1}H NMR of M3MP semi-fluorinated addition product.
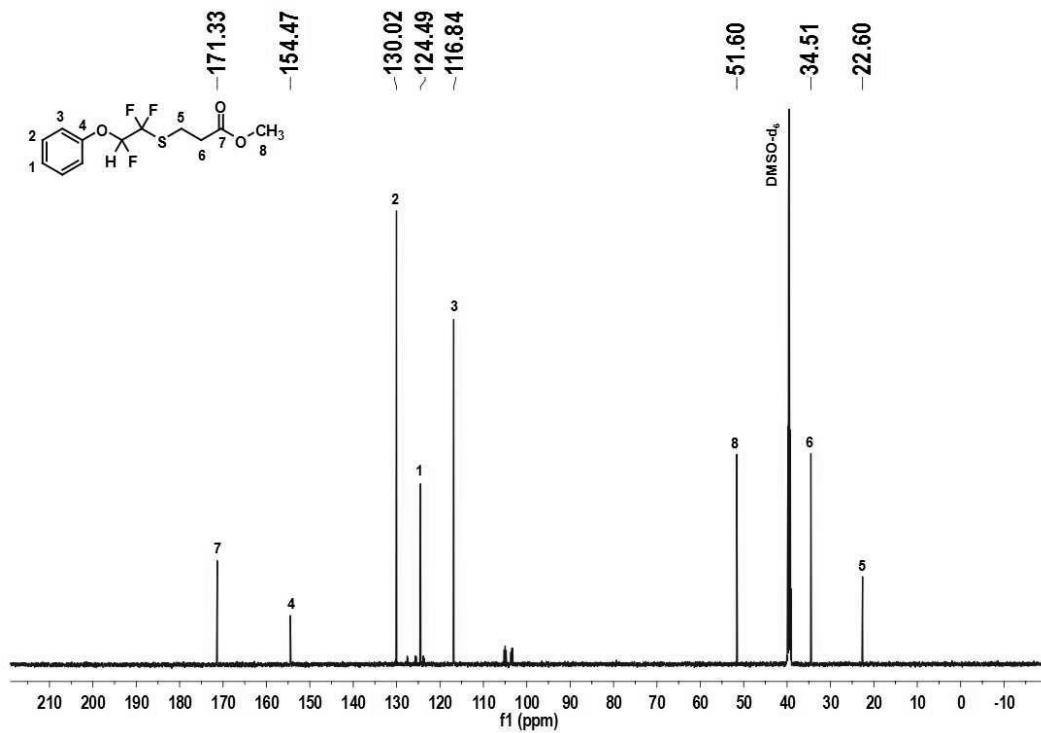
Figure D.2 ^{13}C NMR of M3MP semi-fluorinated addition product.
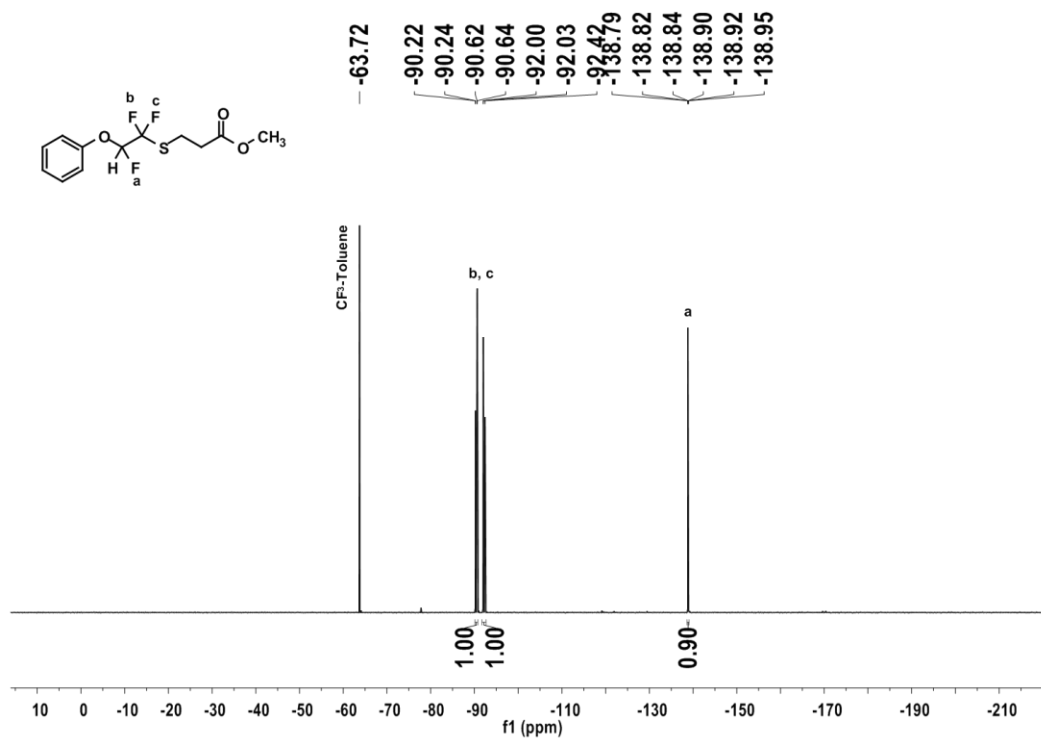
Figure D.3 ^{19}F NMR of M3MP semi-fluorinated addition product.
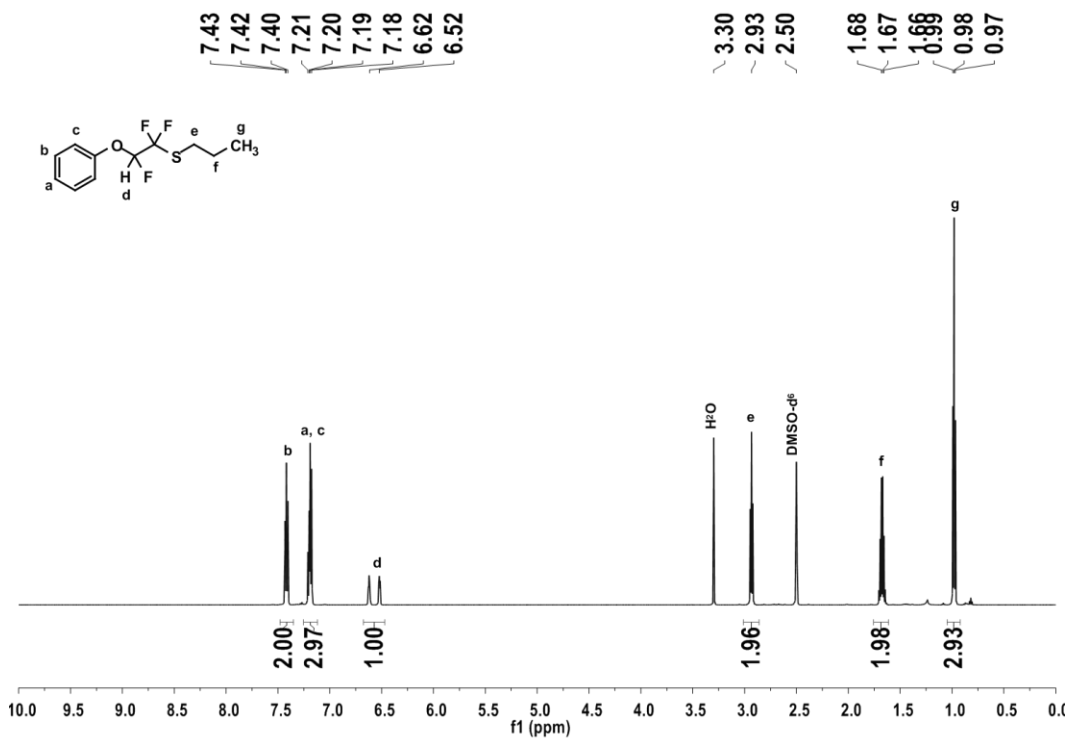
Figure D.4 ^{1}H NMR of PrSH semi-fluorinated addition product.
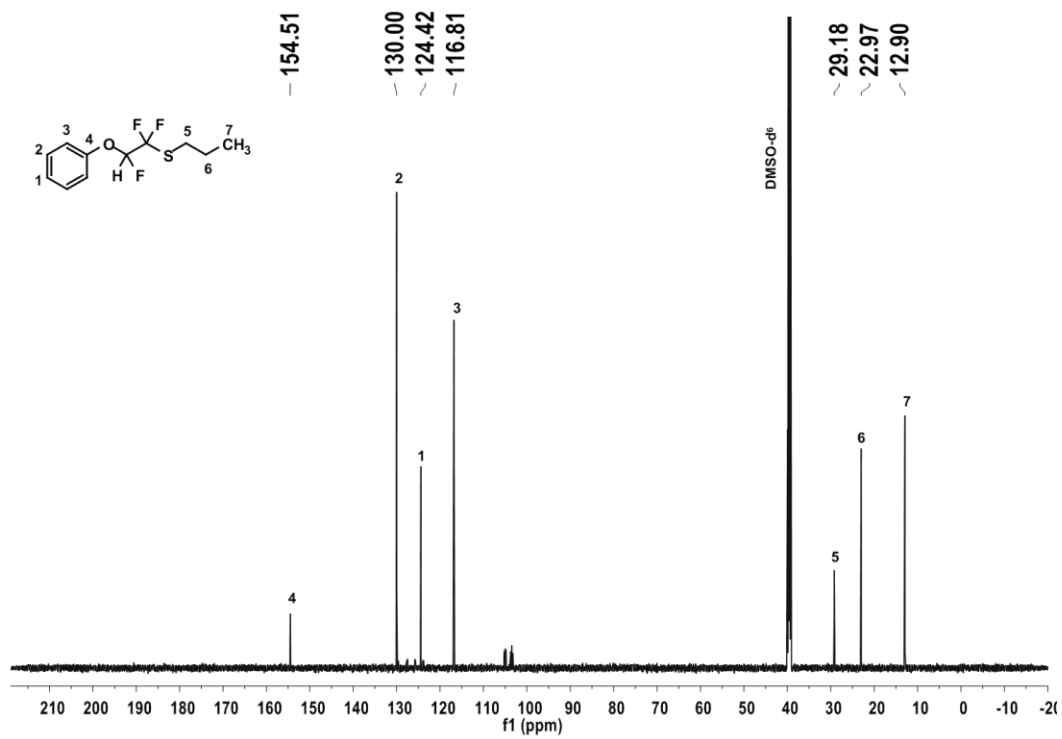
Figure D.5 ^{13}C NMR of PrSH semi-fluorinated addition product.

143
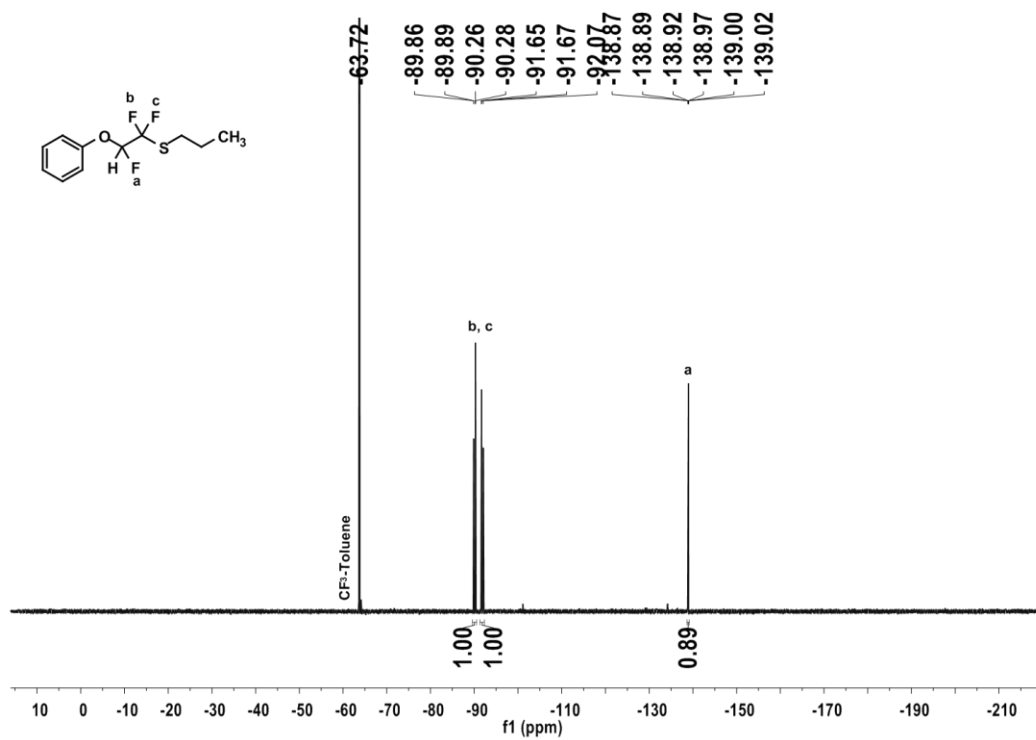
Figure D.6 ^{19}F NMR of PrSH semi-fluorinated addition product.
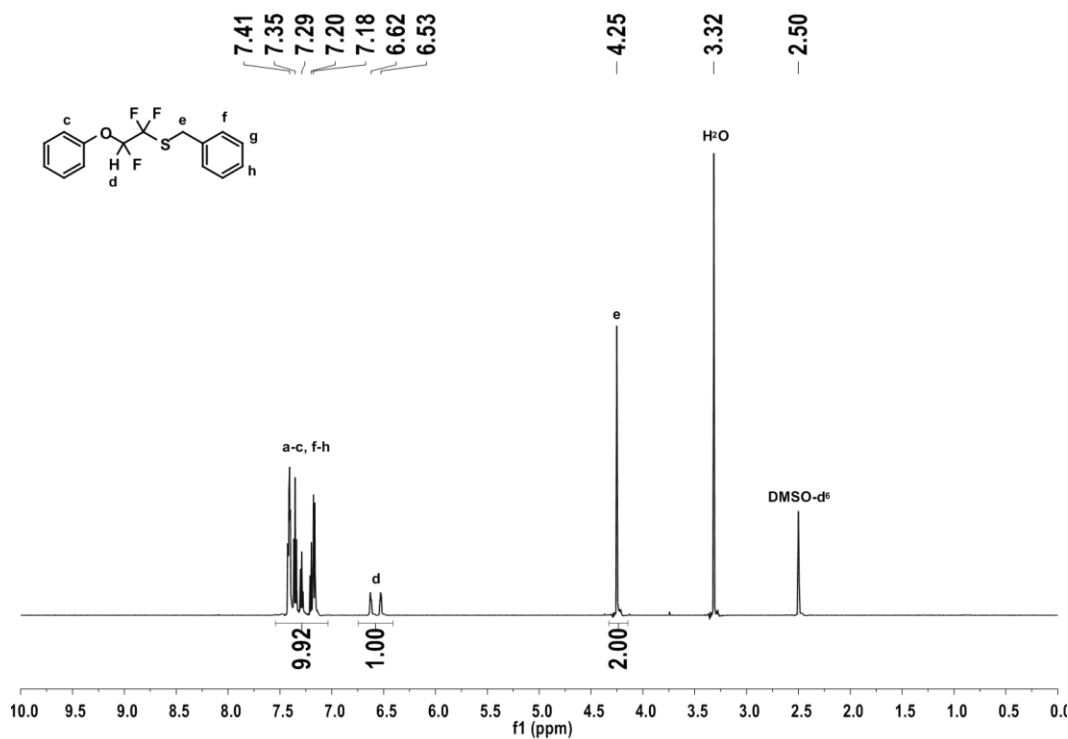
Figure D.7 ^{1}H NMR of BnSH semi-fluorinated addition product.
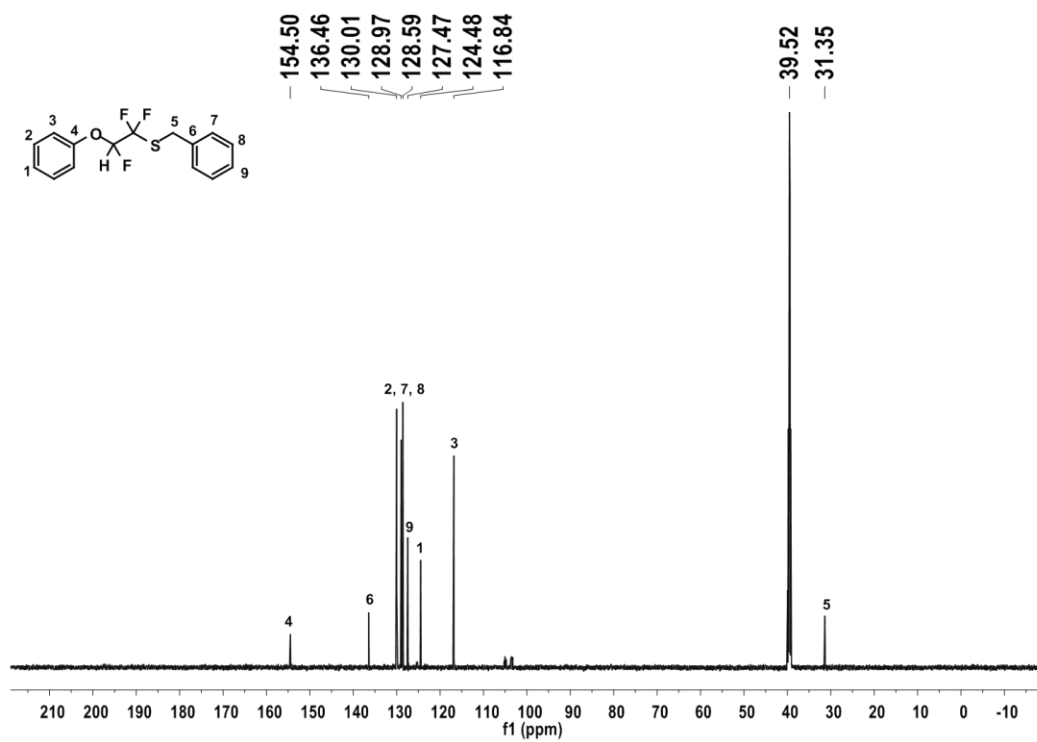
Figure D.8 ^{13}C NMR of BnSH semi-fluorinated addition product.
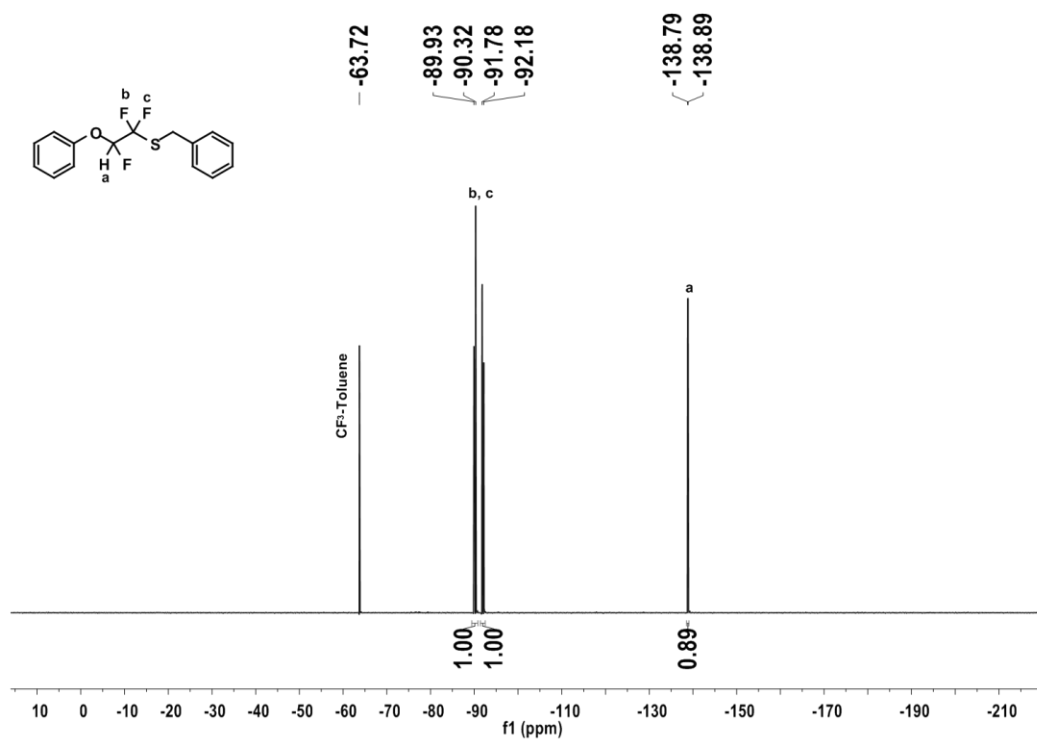
Figure D.9 ^{19}F NMR of BnSH semi-fluorinated addition product.
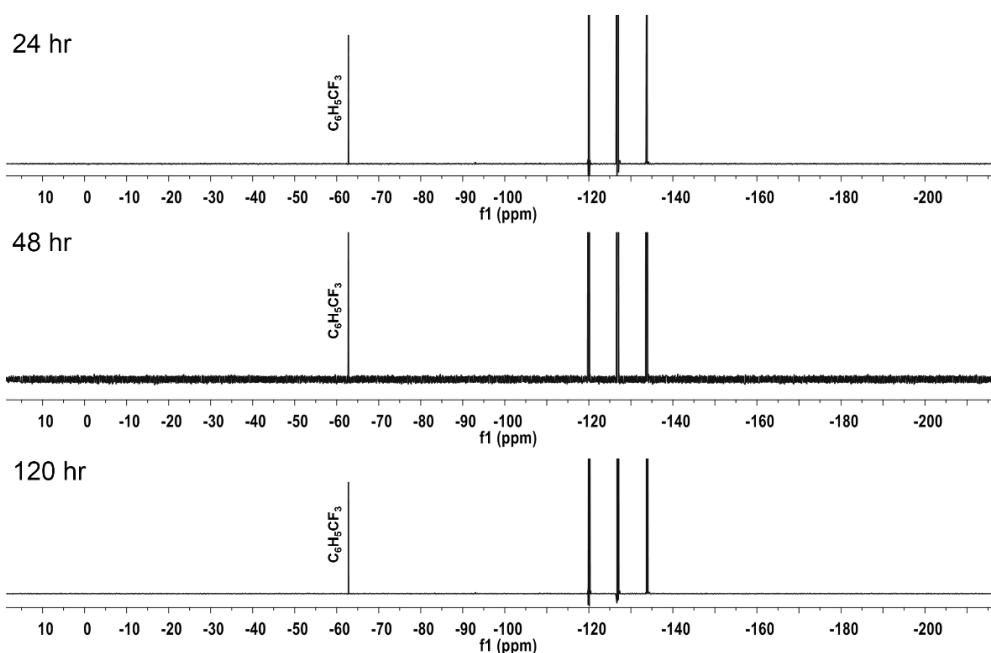
Figure D.10 Chemical structures of monofunctional alkene monomers used in alkene kinetic comparison study
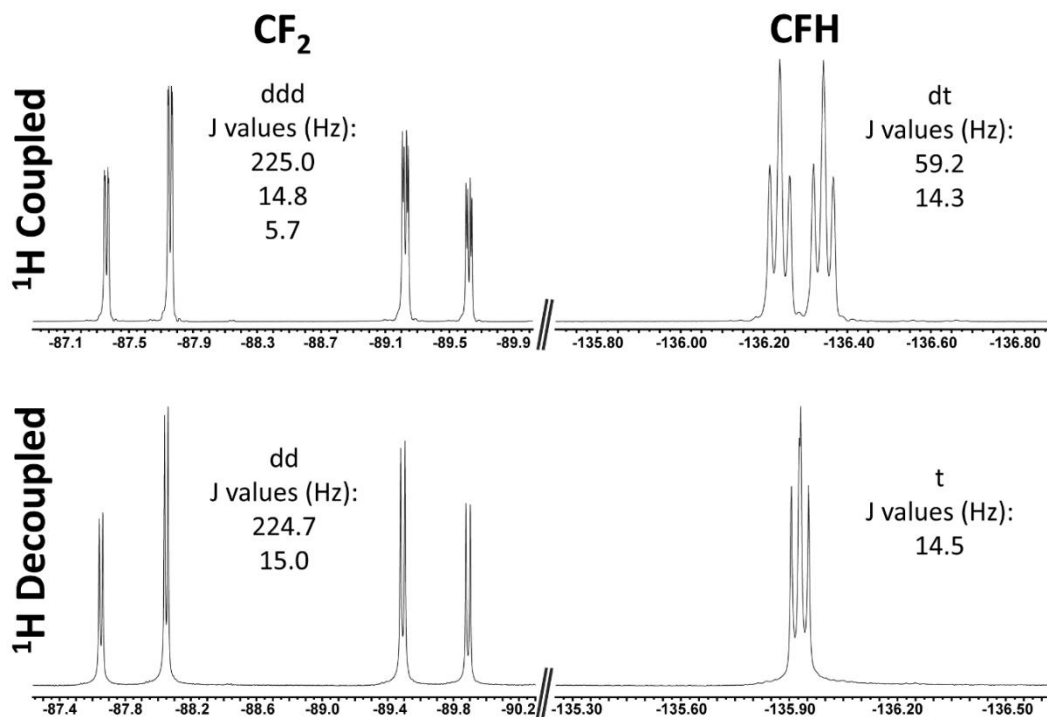
Figure D.11 ^{19}F splitting patterns of TFVE-SH addition products with ^{1}H signal coupled and decoupled.

146
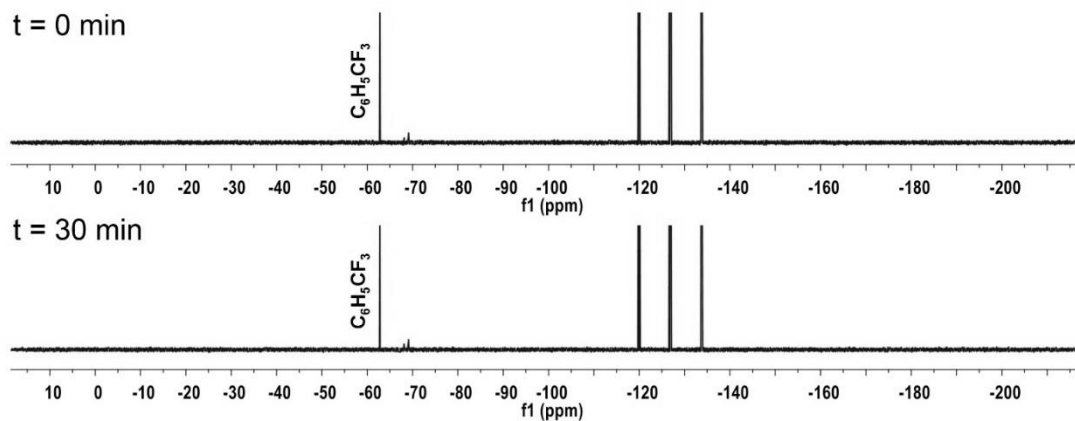
Figure D.12 ^{19}F NMR of Ph-TFVE and 1 wt % photoinitiator before and after 30 minutes of exposure to 100 mW/cm^2 intensity UV light. Absence of new fluorine peaks confirms that Ph-TFVE does not homopolymerize under the model reaction conditions used in this study (small peaks around -70 ppm are residual impurities in monomer).
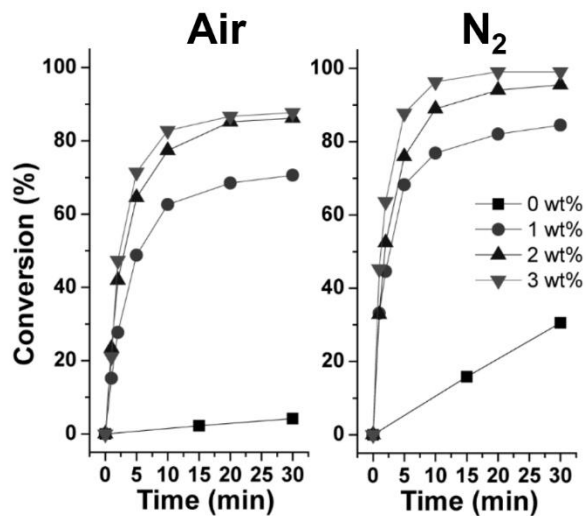
Figure D.13 BnSH/Ph-TFVE reactions conducted under varying wt % photoinitiator at 100 mW/cm^2 UV light in air (left) and N$_2$ (right).
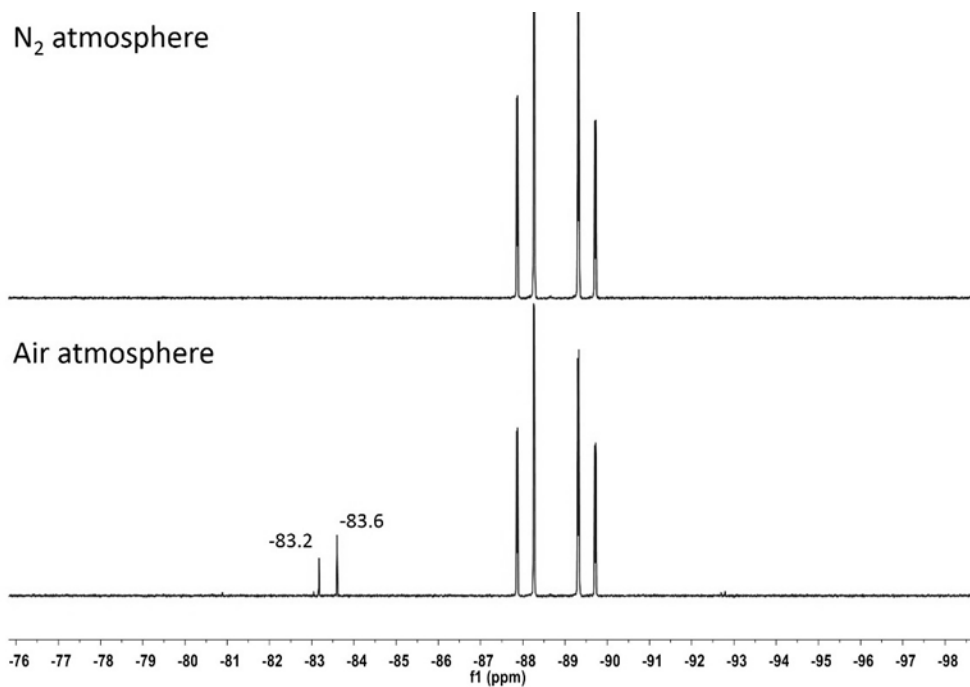
Figure D.14 Condensed ^{19}F NMR spectrum of reaction products of 1-dodecanethiol and Ph-TFVE conducted in nitrogen (top) and air (bottom). Air spectrum contains peaks associated with CF$_2$ of degradation products **I** and **II**.
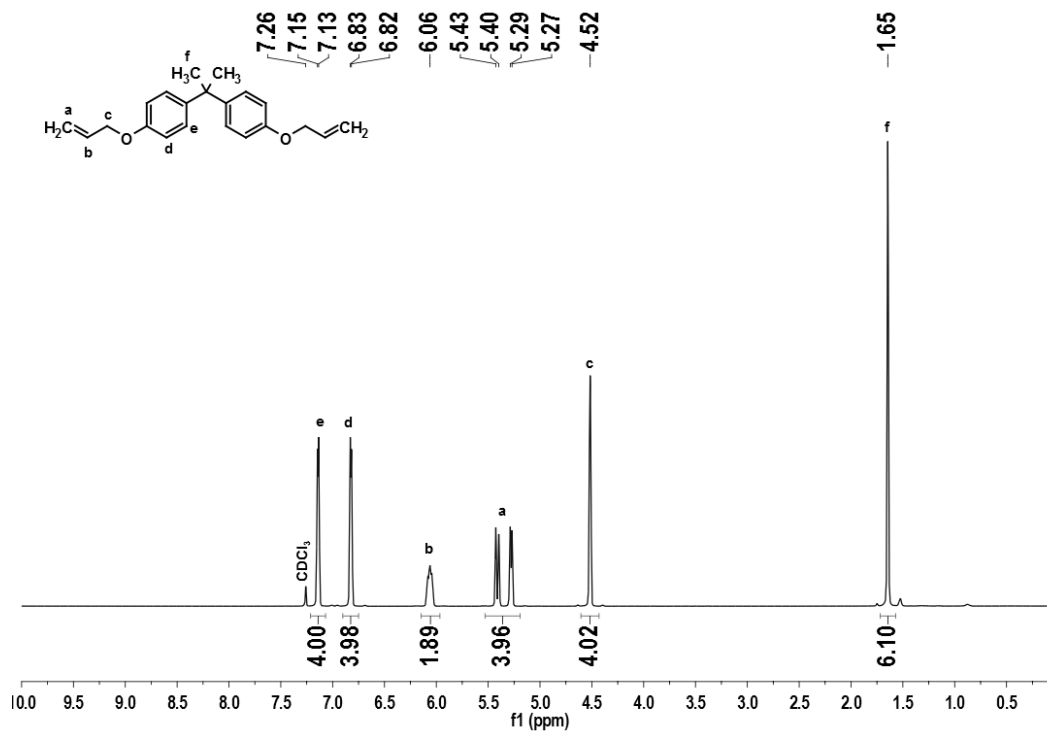
Figure D.15 ^{1}H NMR of Allyl-BPA.
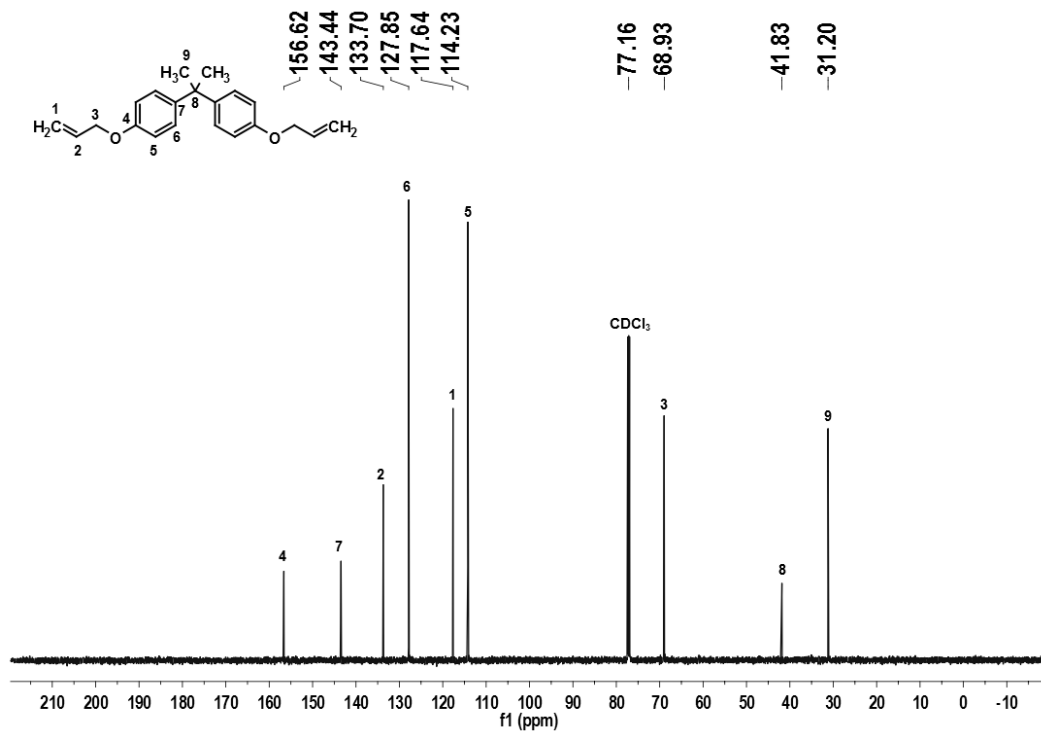
Figure D.16 ¹³C NMR of Allyl-BPA.
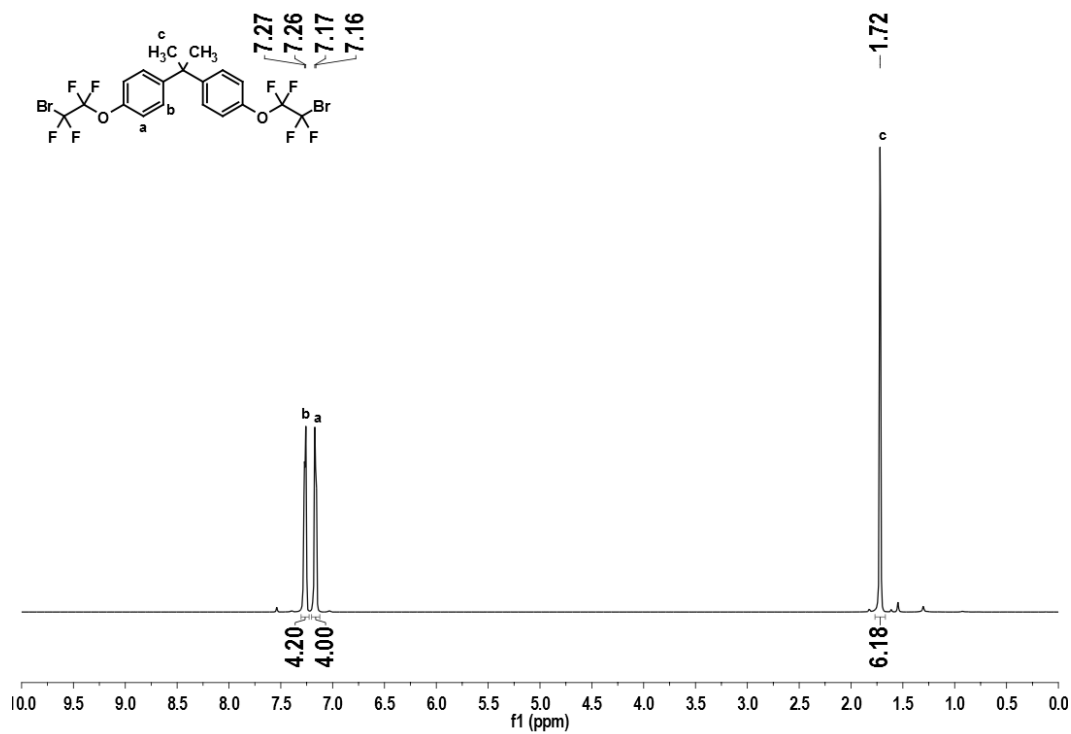
Figure D.17 ¹H NMR of BrE-BPA.
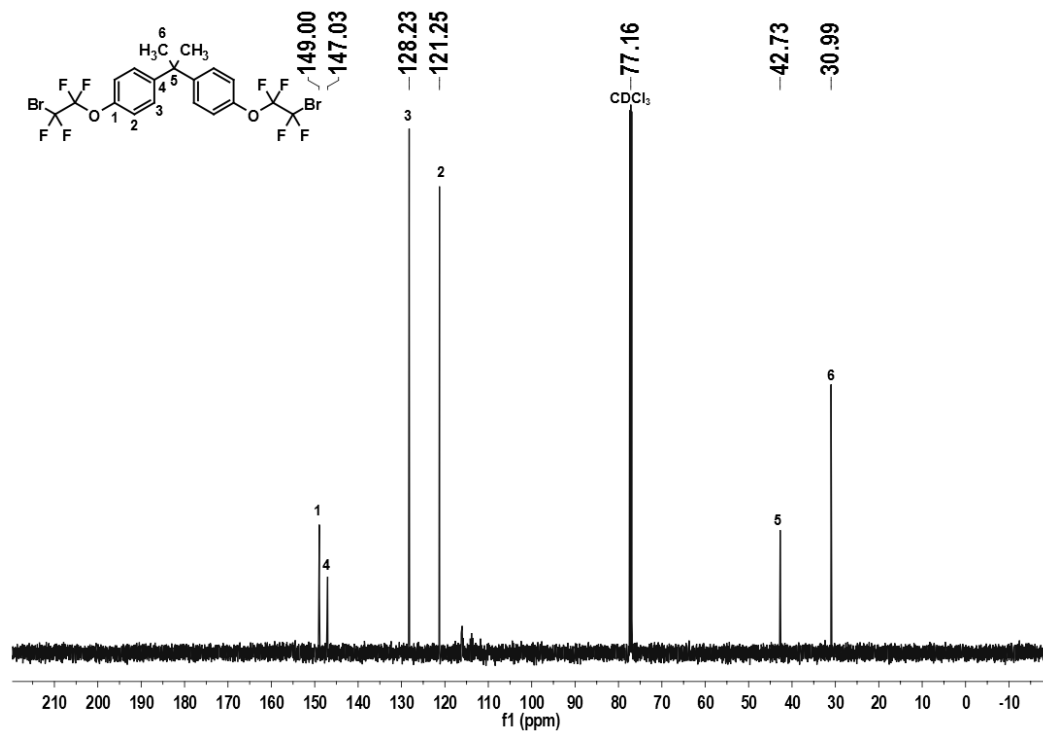
Figure D.18 ^13^C NMR of BrE-BPA.
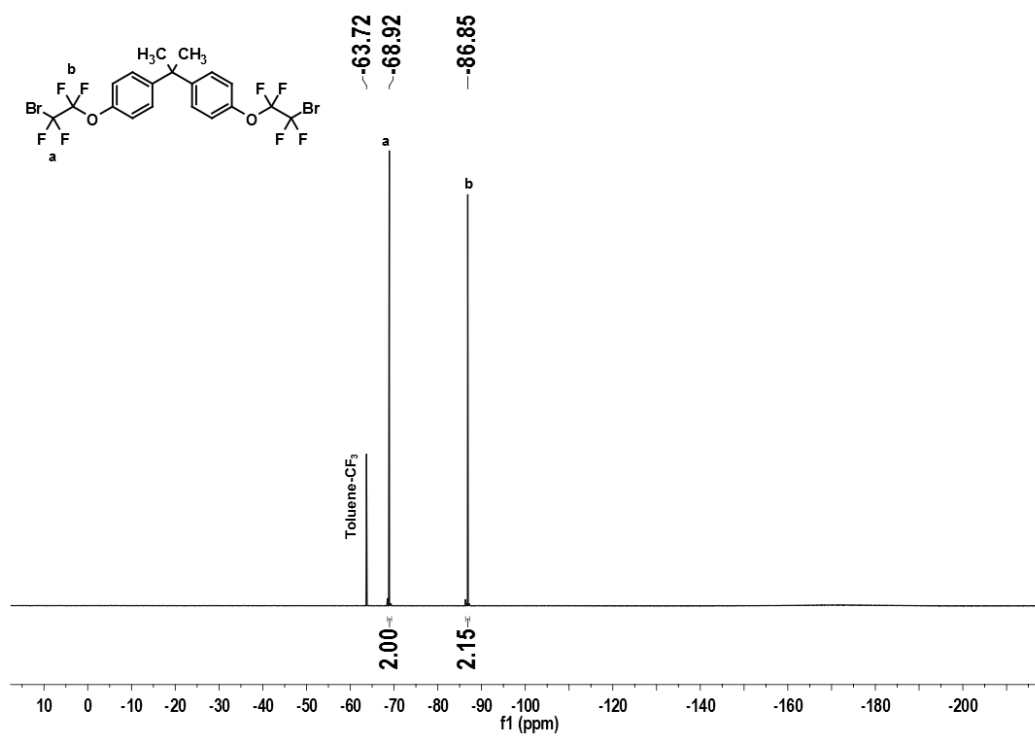
Figure D.19 ^19^F NMR of BrE-BPA.
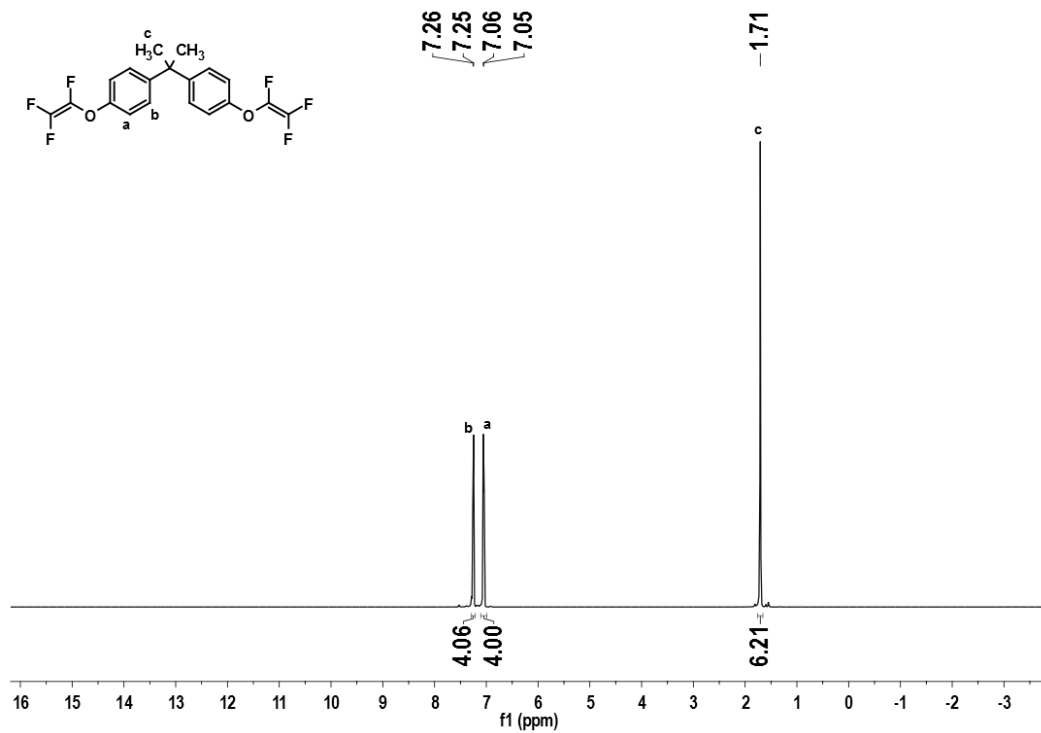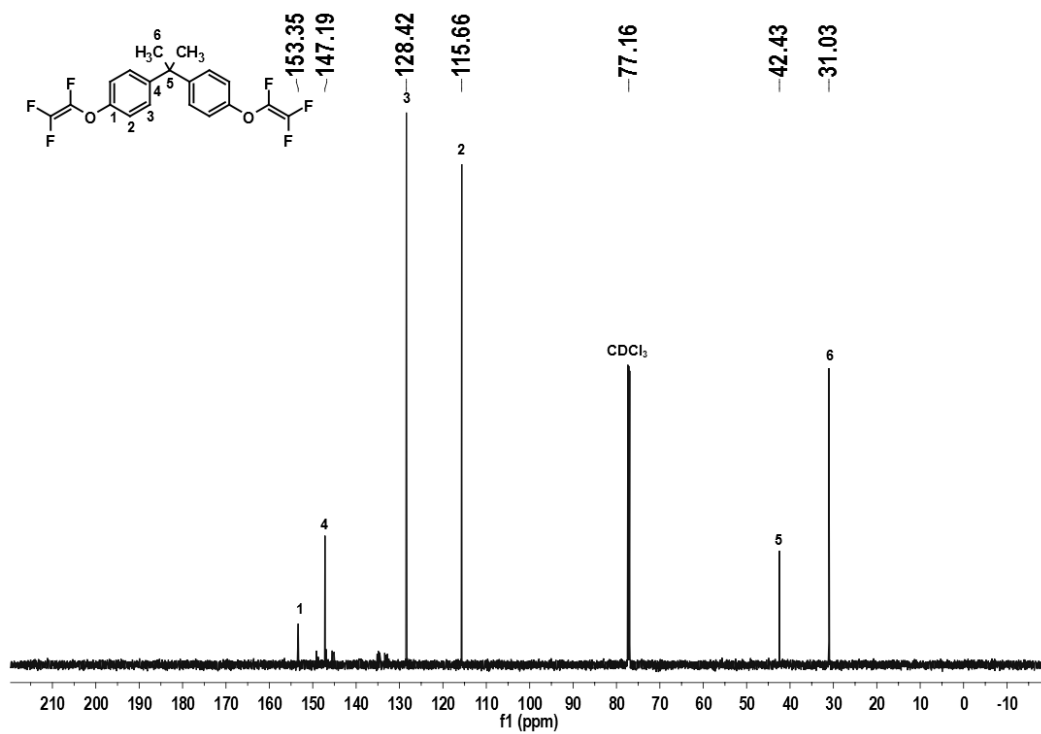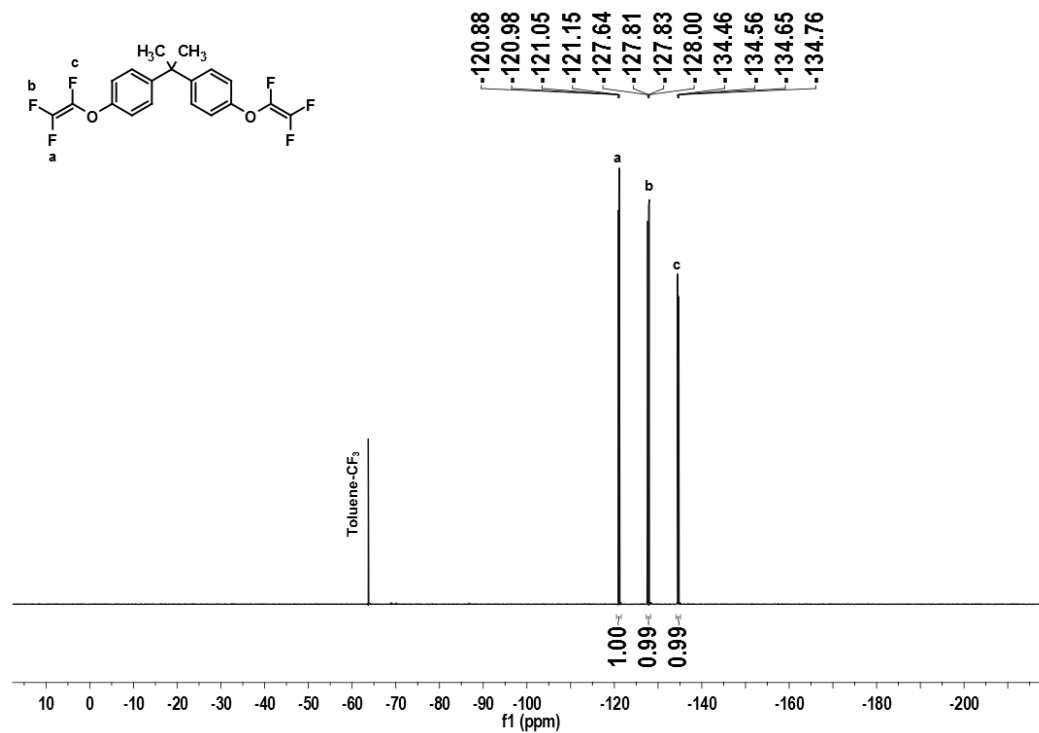
Figure D.20 ^{1}H NMR of TFVE-BPA.

Figure D.21 ^{13}C of TFVE-BPA.

Figure D.22 ^{19}F NMR of TFVE-BPA.